

Limitations to High-speed Crystal Growth Based on Conservation Laws

A DISSERTATION

SUBMITTED IN PARTIAL FULFILLMENT OF THE REQUIREMENTS

for the degree of

DOCTOR OF PHILOSOPHY

in

CHEMICAL ENGINEERING

by

EYAN PETER NORONHA

B.TECH. AND M.TECH, CHEMICAL ENGINEERING, INDIAN INSTITUTE OF TECHNOLOGY BOMBAY

CARNEGIE MELLON UNIVERSITY

Pittsburgh, Pennsylvania

May, 2022

*Dedicated to my loving parents,
Enas and Veera Noronha*

Copyright © 2022, Eyan P. Noronha
All rights reserved

Acknowledgments

First and foremost, I would like to thank my advisor, Erik Ydstie, for having me as his student and introducing me to the problem of silicon wafer production which served as the starting point for this thesis. Erik always made time to meet me and provided me with support in any way possible. In addition to research, I gained invaluable experience in working on the startup Industrial Silicon Technologies LLC with Erik, Reed McManigle, Michael Helman, Matt Cline, and Kristina Nikiforova. The combination of research and startup experience has provided me with a wider perspective on the commercialization of new technology.

My committee members—Larry Biegler, Andy Gellman, and Franziska Weber—have played a great role in this thesis with their inputs and suggestions. Larry is like a role model to me and has always been supportive throughout my Ph.D. I am also grateful for Prof. Bob Pego from the mathematics department at CMU. Our conversations have inspired some of the methodologies in this thesis.

The Process Systems Engineering (PSE) group at CMU is a collection of the finest minds and the warmest hearts. Our chats during happy hours are memories that I will carry forever. In particular, I want to thank Aliakbar Izadkhah, Xiangyu Yin, Saif Kazi, Akang Wang, David Thierry, and Carlos Nohra for always keeping their enthusiasm and lifting my spirits during the pandemic; and my research group—German Oliveros, Jiaying Ke, Zixi Zhao, Dana McGuffin, and Zicheng Cai for their camaraderie and support. Zicheng has been an awesome labmate and a friend who has always stood by me. I also owe special thanks to other members of the PSE group—David Bernal, Can Li, Sitoshna Jatty, Seolhee Cho, Kaiwen Ma, Owais Sarwar, Brad Johnson, Yijia Sun, Can Ekici, Noriyuki Yoshio, Kuan-Han Lin, Vibhav Dabadghao, Thomas Krumpolc, Hua Wang, and Chris Hanselman—for being a source of joy and inspiration during my Ph.D.

There are many friends outside the PSE group that have given me a tremendous amount of encouragement: Namit Chaudhary and Sai Sandeep for being the most amazing roommates who helped me during my surgery; Biswajit Paria, Kartik Gupta, Kin Gutierrez, Stefania Vattiata and Giulio Zhou for the supportive, fun conversations and dinners; Shamin-dra Shrotriya and Shoham Sen for many interesting math study sessions that we had together; the ChIGSA 2 group—Bhagyashree Lele, Bhavya Balu, Rajashri Sengupta, Anirudh Subramanyam, Yash Puranik, and Shivam Sahu—for making me less homesick; my friends

back in India—Maitri Vora, Shradha Kanojia, Krunal Mazumdar, Reinees Maknojjia, Shashank Parikh, Darshil Rambhia, Pranjal Chokhani, Anuj Shah, Coral Chatterjee, and Yash Mehta—for regularly checking up on me and always keeping me in their thoughts; and Abhijeet Alshi, Nitish Kaushik, Kedar Gupta, Shail Godiwala, Aman Wagadre, Chinmay Aras for helping me getting used to graduate school.

Throughout my life, my parents—Enas Noronha and Veera Noronha—have passed me their wisdom and principles of living a simple and honest life. Their love and prayers have given me the strength to get through difficult times. My brother, Valen Noronha, has always offered a shoulder for me to rely on.

My partner Leqi Liu has supported me with her constant love, companionship, encouragement, and wisdom. She is the best thing that happened to me during my Ph.D. This thesis would not be possible without her. I thank her for the incredible amount of support and guidance that she has given to me.

This research is made possible by the funding provided by the US DOE American Made Solar Prize competition, National Science Foundation (No. CBET 093 2556), GAP funding from the CMU tech transfer office, Chevron fellowship, and the CMU Presidential fellowship.

Eyan P. Noronha
Pittsburgh, PA
April 2022

Abstract

The main application motivating this thesis is the design of a high-speed crystal growth process, called the Horizontal Ribbon Growth (HRG), that can reduce the costs of manufacturing silicon wafers by 50%. Silicon wafers serve as the primary photovoltaic material for solar cells, therefore, innovations in HRG can make solar energy more affordable for everybody.

The main challenge with HRG is that stable operating conditions for the process are not very well known. In addition, the process is not economically viable due to low production speeds. To add to this, current models of crystal growth cannot predict the limitations in production speed. Without a predictive model, it is not possible to diagnose the limitations of the HRG process.

The main goal of this thesis is to develop models that can predict limitations to the HRG process. As we do so, we build on a wider set of mathematical tools, which can be used to model other kinds of solidification processes, like crystal growth and droplet freezing, as well.

To find the stable operating conditions, we develop a parametric free energy formulation and use Weierstrass' variational theory to analyze stable ribbon growth configurations under static conditions. The parametric formulation allows us to find multivalued meniscus shapes which are currently not known in the crystal growth field. The stability of the meniscus shapes is analyzed using second order variation to the free energy. The systems exhibits saddle node bifurcations and shows no solution for the meniscus in the horizontal ribbon configuration. The range of stable operating conditions is plotted as a function of pull angle and melt height. We also perform a simple proof of concept "kitchen" experiment to illustrate the instability of the HRG configuration.

A novel numerical algorithm based on energy conservation is developed to model the

heat transfer and phase transition near non-smooth interfaces. The algorithm uses a conservative discretization scheme to simulate non-smooth interface motion, for e.g., in the case of crystal growth. Simulation of the HRG process demonstrates the phenomena of pull speed limitation observed in experiments. A series of simulation studies are performed to quantify the effects of active cooling on the ribbons' growth rate and thickness. A linear scaling relationship between the limiting pull speed and the total heat removed is derived empirically for a family of Gaussian cooling profiles. These scaling relationships show that the intensity and spread of a cooling profile are directly tied to the growth rate limit and the ribbon's thickness, respectively.

Conservation laws are used to find constraints on the angles at the solid-liquid-gas triple junction. Energy and mass conservation imply a 90° angle for the solid and liquid phase. The problem of pull speed limitation is directly attributed to the perpendicular shape of the solid-liquid interface. The perceived advantage of the HRG process with vertical heat transfer is found not true. The experimental observations of a 55° facet angle are reconciled with the theoretical 90° angle using a multiple-scale theory. A cellular automata simulation algorithm is outlined to explain this point of view. Results from the simulations exhibit a 55° solid angle at the triple junction, in line with the multiple-scale theory. The formation of a facet angle at the triple junction is shown to have a negative effect on the pull speed limitation. Results also include the first simulation evidence for the formation of a dual facet at the triple junction.

Contents

Acknowledgments	i
Abstract	iii
List of Tables	
List of Figures	
1 Why improve silicon wafer production?	1
1.1 Introduction	1
1.2 Dirt is not dirt cheap	2
2 Overview of the Ribbon Growth Process	4
2.1 Introduction	4
2.2 History of the Horizontal Ribbon Growth (HRG) Process	5
2.3 Challenges and thesis overview	10
3 Weierstrass' variational theory for analyzing meniscus shape and stability	12
3.1 Introduction	12
3.2 Problem Statement	17
3.3 Free energy reformulation in parametric form	18
3.4 Stationary curves via the first variation	20
3.4.1 Analytic form and family of solutions	22
3.5 Stability analysis via the second variation	24
3.6 Results	27
3.6.1 Effect of pull angle	29
3.6.2 Effect of melt height	32
3.7 Practical considerations on meniscus shape	34
3.7.1 Theory	36
3.7.2 Applications	37
3.8 Experimental Design	40

3.9	Conclusions	41
4	Weak Stefan Formulation for Bulk Crystal Growth with Non-smooth Interfaces	42
4.1	Introduction	42
4.2	Mathematical Formulation	46
4.2.1	The Energy-Phase Rule	47
4.3	Numerical Simulation Model	49
4.3.1	Interface Propagation	50
4.3.2	Numerical Method	52
4.4	Application: Horizontal Ribbon Growth	53
4.4.1	Results	56
4.4.2	Discussion	59
4.4.3	Comparison Between Radiation and Gas Cooling	61
4.5	Active Cooling Design for Horizontal Ribbon Growth	63
4.6	Conclusions	67
5	A theory on interface propagation at the solidification triple junction	70
5.1	Introduction	71
5.2	Constraints due to Mass and Energy Conservation	74
5.3	Heat Transfer and Fluid Flow near a Triple Junction	78
5.4	Interpretation: Multiple Length Scales Point of View	83
5.5	Cellular Automata Simulations for Facet Growth	86
5.5.1	Simulation results	90
5.6	Conclusions	93
6	Conclusions and Future Work	95
6.1	Summary and Contributions	95
6.2	Future Work	97
	Bibliography	98
A	Young's contact angle and Gibbs pinning condition	113

List of Tables

3.1	Material properties and parameters used in the illustrative example.	28
4.1	Material properties of silicon used for simulation	56
4.2	Numerical values for simulation instances	65
4.3	Best fit parameters	66

List of Figures

1.1	Left: Increase in solar capacity in the US. Right: Decrease in the cost of electricity generated by solar. Source: Michael O’Sullivan, Senior VP, NextEra Energy Resources	2
1.2	Breakdown of the solar panel supply chain.	3
2.1	The contrast in the heat transfer mechanism between vertical and horizontal ribbon growth techniques as is currently known.	5
2.2	The heat transfer model proposed by Zoutendyk. Zoutendyk arrives at the given shape by equating the rate of ribbon growth with the heat flux in the vertical direction.	7
2.3	(left) The pull speed v.s. thickness data for the LASS process. We see that the thickness of the sheet from the LASS process is comparable to the ones produced by Kudo. However, the cooling provided in the LASS process was much more focused which allowed for better results. (right) Two experimental samples from the LASS process with aligned dendrites (top right) and random dendrites (bottom right).	9
2.4	Side view of sheet pulled slowly from the furnace. Growth direction is to the left. {111} facet is observed at the leading edge.	10
3.1	Schematic for a horizontal crystal ribbon growth process. The formation of a meniscus at the end of the crucible is essential for steady state operation	14
3.2	Characterization of the ribbon growth family based on pull angle (β)	15
3.3	(left) Stationary curves arising from the solution of the classical Euler-Lagrange equation yield single valued functions of the type $x(y)$. (right) Weierstrass’ variational approach expand the solution space to account for multi-valued stationary curves, described by curves of the type $x(s)$ and $y(s)$	19
3.4	Family of solutions for the parametric Young-Laplace equation	24
3.5	(left) Stationary meniscus shapes obtained using the analytical solution in parametric form. Curves correspond to a value of $\beta = 10^\circ$ and $h = 5.35\text{ mm}$. (right) The sine of the tangent angle $\Omega(s)$ for different pinning angles. The curves crossing zero correspond to the unstable modes.	28

3.6	Hydro-statically stationary configuration for a melt level of 5.35 mm and a pulling angle of 5° . The solid curve corresponds to a statically stable configuration and the dashed curve corresponds to an unstable configuration. . .	30
3.7	Saddle node bifurcations in the meniscus length S_t and pull angle β solution space. Inset: A zoomed up diagram of the solution space for negative pull angles. Solid lines represent stable solutions for which the Jacobi test is satisfied.	31
3.8	Stable meniscus region (shaded) over the parameter space of melt height and pull angle. Representative meniscus shapes have been drawn for melt height and pull angles.	33
3.9	A schematic highlighting the quantities of interest to evaluate the distance between the contact points (L)	35
3.10	The graph of a syntactrix curve with $h = 0$. The axes are in units of capillary length	36
3.11	Reference schematic for calculating distance between contact points (L) . .	37
3.12	Length of the ribbon exposed to the melt as a function of pull angle	38
3.13	Representative diagrams for meniscus shapes in crystal ribbon growth . . .	39
3.14	A sequence of photographs showing the meniscus spilling over from the corner of the plastic bath. Spill-over is induced by decreasing the angle of the sheet with the bath.	40
4.1	Examples of ill-defined interface velocity at non-smooth corners in bulk crystal growth	44
4.2	Schematic of the horizontal ribbon growth process around the growth zone	46
4.3	Energy-Phase rule	48
4.4	Simulation domain and initial seed configuration of the HRG process	49
4.5	Interface propagation rule for solidification.	51
4.6	Temperature maps for radiation cooling at ribbon pull speeds of 0.3, 0.5, 0.7, 0.9 mm/sec from top to bottom, respectively. The solid black line describes the position of the solid-liquid interface.	55
4.7	Comparison of top surface heat flux for radiation ($v = 0.5\text{mm/sec}$) and Gaussian cooling	57
4.8	Temperature maps for gas cooling at ribbon pull speeds of 0.2, 0.4, 0.8, 1.6 mm/sec from top to bottom, respectively.	58
4.9	Thickness vs pull speed plot for radiation and Gaussian cooling. The dashed lines signify the pull speed limitation observed in simulations.	59

4.10	A close up of the temperature field around the ribbon tip for radiation (left) and Gaussian cooling at limiting pull speeds of 0.9 and 2 mm/sec respectively. The thick black line denotes the interface at $T_m = 1685\text{K}$. Thin black lines denote isotherms at 0.2K intervals.	60
4.11	Top surface temperature profile for radiation (left) and Gaussian (right) cooling.	62
4.12	A graph highlighting the variability in total heat removed using radiation as a function of pull speed. In contrast, the heat removed using cooling jet is almost constant.	63
4.13	A graph of maximum pull speed as a function of heat removed. The dashed lines denotes the best fit lines.	64
4.14	Scaling relationship between maximum pull speed limit and total heat removed for different Gaussian cooling profiles.	66
4.15	Minimum thickness as a function of total heat removed for different Gaussian cooling profiles	67
5.1	A photograph of dual facet formation using antimony demarcation.	73
5.2	A schematic showing the energy flux across the solidification interface at the growth tip.	74
5.3	A schematic showing the mass flux at the interface from liquid to solid phase. The solid angle θ_s is considered to be 90°	77
5.4	A schematic of the three inter-phase boundaries between solid, liquid and gas phases intersecting at the triple point O	79
5.5	Typical polar gamma plot of surface energy of a crystal and the corresponding Wulff shape.	84
5.6	A multiple scales point of view of the angles at the triple point.	85
5.7	An atomic scale interpretation of the 90° solid angle.	85
5.8	Mushy zone ($0 < \chi < 1$) representing the interface.	87
5.9	Three main mechanisms of crystal growth at the interface	87
5.10	Procedure to calculate the facet angle θ along the interface.	89
5.11	Steady state phase field at $v = 4$ mm/sec. The figure on the left includes crystal growth dynamics and the figure on the right does not.	90
5.12	A close-up of the solid angle at $v = 4$ mm/sec. The figure on the left shows different stages of crystal growth dynamics at the interface. The figure on the right shows the triangular wedge shape predicted by Zoutendyk's theory.	90

5.13	Simulation results for the temperature field with crystal growth dynamics (left) and isotropic growth dynamics (right).	91
5.14	Thickness vs. pull speed charts for simulations carried out with (left) and without (right) crystal growth dynamics. The pull speed limitation is more severe when crystal growth is included.	91
5.15	Formation of dual facets near the triple point in presence of impurities. A close-up of the simulation result.	92
A.1	For the case of variable endpoints, the perturbation at the origin is considered to be $\vec{\delta r}$. The aim is to find conditions on the meniscus shape such that $\vec{\delta r} = 0$ is a minimum.	114
A.2	The shaded region displays the range of pinning angles for the inner and the outer edges. The figure shows how the starting position of the meniscus would change as the pinning angle is varied.	114

Chapter 1

Why improve silicon wafer production?

1.1 Introduction

According to the Renewables 2021 Global Status Report [1], fossil fuels represent 80% of the total energy consumption worldwide. Fossil fuels are limited in supply and unequally distributed across the globe, which require complex supply chain networks to meet global demand [2]. When these networks are disrupted, like during COVID-19 and the Russian Ukrainian conflict of 2022, they can lead to concerns of energy security around the globe [3, 4]. Moreover, burning fossil fuels releases carbon and greenhouse gases into the atmosphere. The buildup of greenhouse gases in the atmosphere has caused climate change, a trend that will worsen with more fossil fuel consumption [5].

Solving problems of energy security and climate change is a complex task. One approach taken by countries like United States, China, India, Japan, Germany and many others is to encourage the development of electricity generation using renewable energy. Renewable energy sources like wind, solar, geothermal, etc. are abundant and can be found in some capacity almost everywhere. They are also naturally replenishing and cause less environmental damage. In the coming decades, renewable energy will play a key role in providing security along with decarbonization of our energy systems [6].

Solar energy is the fastest growing renewable energy source—accounting for nearly half of the new U.S. electric generating capacity in 2022 [7]. Figure 1.1 illustrates the growth of solar capacity in U.S and the decrease in the cost of electricity generation due to innovations in photovoltaics. The National Renewable Technology Laboratory (NREL) estimates a 450 GW increase in U.S solar capacity by 2050 in the absence of any government lead

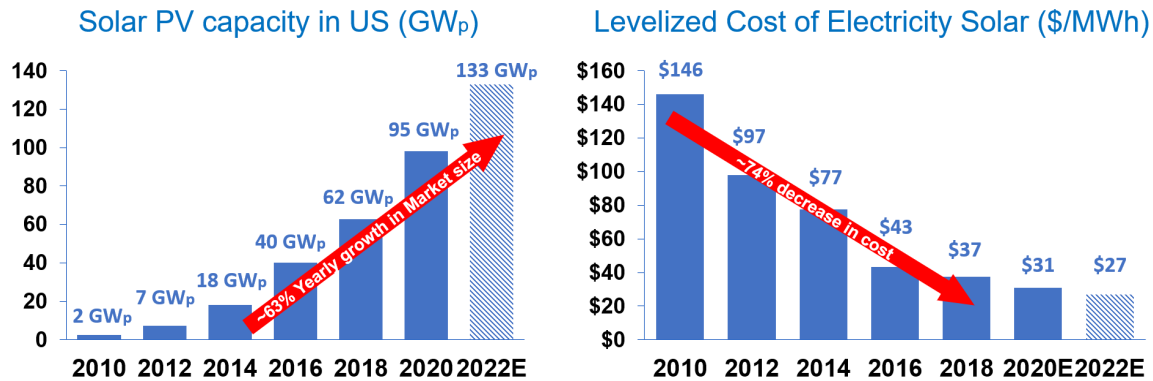


Figure 1.1: Left: Increase in solar capacity in the US. Right: Decrease in the cost of electricity generated by solar. Source: Michael O’Sullivan, Senior VP, NextEra Energy Resources

climate initiative [8]. The estimates are double in the presence of government support. As a point of comparison we note that a large coal plant provides about 1 GW per turbine-generator pair. 90% of this demand is expected to come from silicon based photovoltaics. To meet this demand, existing silicon wafer technology are not enough [9]. Faster and more efficient processes are needed to ramp silicon wafer production to reach multi-gigawatt scale.

1.2 Dirt is not dirt cheap

Silicon is the most abundant element on the Earth’s crust and can be found naturally as oxidized sand (SiO_2). The silicon-oxygen bond in SiO_2 is broken using carbothermic reduction to obtain metallurgical grade silicon (MG-Si). MG-Si is further purified using chemical methods to make it suitable for photovoltaic applications. The resulting product is polycrystalline silicon (poly-Si) and costs $\sim \$10/\text{kg}$, which is 2 orders of magnitude higher than the cost of sand $\sim \$0.05/\text{kg}$. The process of converting sand to poly-Si is highly optimized and provides little opportunity for innovations in cost reduction [10].

The next most significant cost in manufacturing solar panels comes from producing sili-

con wafers from poly-Si. Figure 1.2 provides a breakdown of the solar panel supply chain. The poly-Si is melted in large furnaces and carefully solidified to produce mono-crystalline silicon (mono-Si). This process is energy and labor intensive increasing the price of silicon wafers to \sim \\$65/kg [11].

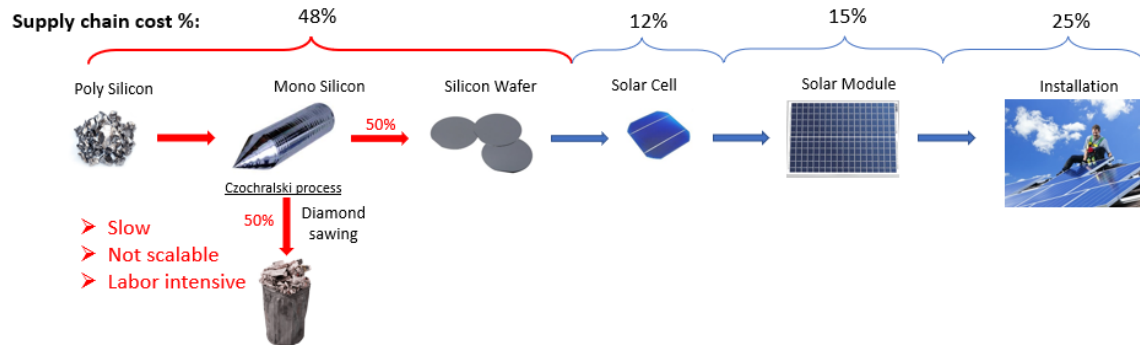


Figure 1.2: Breakdown of the solar panel supply chain.

Traditionally mono-Si is grown through the Czochralski process where silicon is solidified into large log-like ingots. The mono-Si ingots are then squared and cut along the length to make silicon wafers. The process of shaping and sawing produces significant amount of material loss (up to 55% [12]). The material losses alone present an opportunity to cut the cost of silicon wafers by half. In addition, the Czochralski is a batch process, which makes it slow and labor intensive. This makes the Czochralski process difficult to scale-up to meet the global renewable energy demands.

In the next chapter we look at some proposed high-speed wafer production processes that can avoid material losses due to sawing and also scale to meet the global demand for silicon wafers. These processes have the potential to reduce the cost of silicon wafer manufacturing, making solar energy more affordable for everyone.

Chapter 2

Overview of the Ribbon Growth Process

2.1 Introduction

Silicon ribbon growth technology was conceptualized in the 1960s as an alternative to ingot based crystal growth techniques such as the Czochralski or the Bridgman process [13, 14]. These ribbon growth processes were aimed at manufacturing thin single crystal silicon sheets for applications in solar and semiconductor industries. Since there was no squaring or wire sawing of ingots involved, these processes could reduce the cost of manufacturing silicon wafers by 30-50% in material savings alone. The most successful of them were the family of vertical ribbon growth (VRG) processes like the Edge-defined Film Growth (EFG), the Dendritic Web Growth (WEB) and the String Ribbon Growth (SRG) process [15].

In a vertical ribbon growth process, sheets of single crystal are pulled from the melt in the vertical direction with the aid of a shaper to maintain the meniscus shape and stability. The sheets produced in this manner could be extracted continuously. They were 100-200 μm in thickness, and flexible due to the absence of mechanical sawing [16, 17, 18].

Despite their notable advantages, the vertical ribbon growth processes could not commercially compete against the Czochralski process. This was partly due to their low production speeds and difficulty in scaling up the process [19, 20]. Around the same time, Horizontal Ribbon Growth (HRG) processes like the Ribbon Growth on Substrate (RGS), Low Angle Silicon Sheet (LASS), and Melt quenching were also being developed [21]. The belief was that a horizontal mode of withdrawing a sheet from the melt would allow for an increase in latent heat removal from the solidification interface. This was coupled with the notion that the longitudinal rate of crystal growth is faster than the rate of advance

of the interface by a factor of $\text{cosec}(\theta)$ [22]. Figure 2.1 provides a schematic of the ideas discussed. Theoretical estimates on the growth speeds of the horizontal ribbon growth process predicted its throughput (m^2/h) to be 40 times faster than the EFG process and 10 times faster than the Czochralski process for similar wafer dimensions [23, 24]. However, these estimates were later proved false in experiments [25]. The disparity between theoretical estimates and experimental results serves as the starting point for this research work. In the next section, we look into the history of the HRG process.

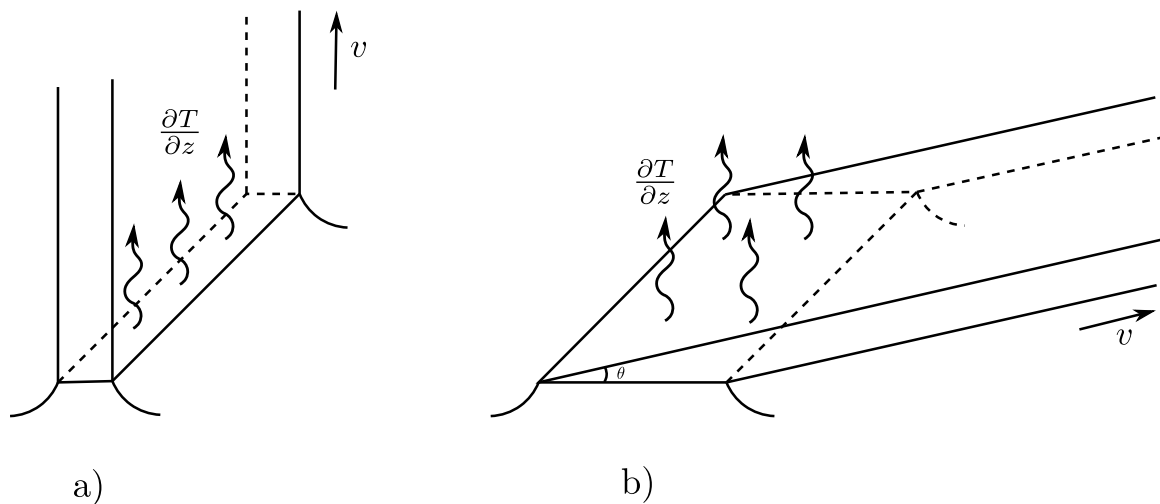


Figure 2.1: The contrast in the heat transfer mechanism between vertical and horizontal ribbon growth techniques as is currently known.

2.2 History of the Horizontal Ribbon Growth (HRG) Process

The HRG process was first invented by William Shockley [14] in 1962. The invention was intended for reliably growing thin sheets of single crystal silicon to replace the traditional batch process of slicing single crystal cylindrical ingots. The main idea of the process was to crystallize a thin film of crystal on top of the melt by careful surface cooling and seeding operation. The crystal would float on top of the melt due to buoyant forces and have

minimum mechanical stress on the ribbon leading to fewer defects.

In 1969, Carl Bleil was the first to utilize Shockley's idea to produce ice and germanium ribbons by placing the heat sink directly in contact with the surface of the wedge [26, 27]. Bleil provided three conditions for the process to be viable: "(1) the new growth does not adhere to the heat sink, (2) the seed does not melt away and (3) the new growth does not become so thick that the crystal cannot be extracted from the crucible." Despite his success, the crystals produced exhibited many visible structural irregularities. As Bleil suggested, these irregularities may be produced because of the difficulty in maintaining and controlling a constant thermal heat flux, which arises due to the improper solid-solid contact between the ribbon and the heat sink. To circumvent this, Bleil proposed to use a water cooled plate for radiative cooling or a gaseous/liquid conductive medium.

Following Bleil, Kudo [28] proposed a new design for the HRG process by replacing the heat sink with a gas cooling system above the melt. This enabled high speed growth of crystals. In his patent Kudo mentions, "Bleil also suggests in another paper 'soft' cooling through radiation only or by means of a gaseous medium or a liquid medium for the purpose of realizing uniform crystal growth, but says nothing about how to increase the rate of crystal growth. It is supposed that the crystal growth velocity of the Bleil patent is about 3mm/min at the most [29]." The gas cooling system designed by Kudo provided the necessary cooling required for latent heat extraction. Kudo claimed that this facilitated growth speeds of up to 7mm/sec for monocrystalline ribbon and 14mm/sec for polycrystalline ribbon. Kudo also mentioned that the ribbons obtained were of a maximum length of 2m, which suggests that the process was not being operated at steady state.

At the same time, John Zoutendyk at the Jet Propulsion Laboratory, provided theoretical analysis of the heat flow for HRG under simplifying assumptions [30]. His heat transfer model evaluated the geometries of the ribbon cross section for different cases of heat sinks. Zoutendyk [31] was the first to develop an expression correlating the ribbon thickness, pulling speed and the thermal gradients in the melt. A simplified interpretation of his

equation (17) in [31], which can also be seen in fig. 2.2, can be written as,

$$\rho L V_{pull} t = Q_{tot}, \tag{2.1}$$

where ρ is the density, L is the latent heat of fusion, v is the pulling speed of the ribbon from the furnace, and t is the thickness of the ribbon. Equation (2.1) equates the latent heat released on the left hand side to the total heat (Q_{tot}) removed from the system. It will be useful to keep this equation in mind since it has lead to significant misconception in the HRG literature [28, 27, 32, 33, 31, 34]. Based on equation (2.1), Zoutendyk recommends pull speeds of 1cm/sec to make ribbons of 100 μm thickness.

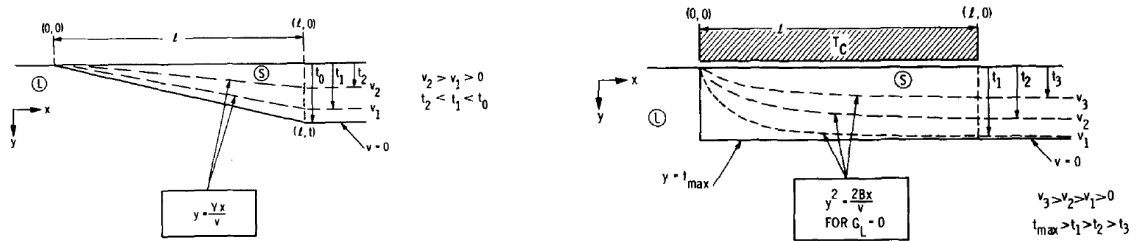


Figure 2.2: The heat transfer model proposed by Zoutendyk. Zoutendyk arrives at the given shape by equating the rate of ribbon growth with the heat flux in the vertical direction.

Glicksman and Voorhees [34] complemented Zoutendyk’s theoretical model by assuming a parabolic shape for the ribbon wedge. The models provided by Zoutendyk and Voorhes did not provide any pull speed limit for the ribbon. However, Voorhes pointed out a singularity problem at the tip of the ribbon due to conflicting boundary conditions. This singularity problem is also encountered by Helenbrook [35].

The issue of melt spill-over was first investigated by Rhodes et al. [36]. In particular, they proposed to model the shape of the meniscus formed between the ribbon and the crucible using the free energy of the system. This work would be later extended by Oliveros et al. [37] and Noronha et al. [38]. They analyze the stability of the meniscus using a variational formulation. Oliveros et al. [37] and Noronha et al. [38] discover what was observed by

Kudo in his experimental operation—“the hydro-statically feasible configurations require the meniscus to be ‘taller’ than the melt height, and that a ribbon be pulled at a slight angle to provide stability.”

The concept of pulling ribbons at a slight angle to the horizontal is the main motivation behind the Low Angle Silicon Sheet (LASS) process. The LASS process developed by Jewett et al. [32] around 1979 was a modification of the HRG process. Of all publicly available literature on HRG to date, LASS was the most successful in producing silicon ribbon with continuous growth rates of about 7.5mm/sec. A few samples of the ribbons produced are illustrated in fig. 2.3. The process operated at steady state and produced ribbons over 30m in length with a ribbon width of 6.7cm and 0.5mm thickness. Jewett attributes the success of his process to the design of the furnace and its operating procedure, both of which are mentioned [39]. Jewett [40] also designed a jet cooling system which is comparable to the design of Varian Semiconductors.

Daggolu et al. [41, 42, 43] established a multi-physics model on how fluid flow, heat transfer and solute segregation interact in the HRG system. The key finding is that the Marangoni convection influences the classical segregation profile, which concentrated underneath the solid-liquid interface.

With the aim of commercializing the HRG process, Peter Kellerman [25] spearheaded the Floating Silicon Method (FSM) at Varian Semiconductors. FSM was based on the theoretical models of Zoutendyk and Kudo which predicted the formation of a long triangular wedge over the length of the crucible. Latent heat dissipation was thought to happen along the entire length of the thin ribbon, which could lead to larger cooling area and thus high production rates. In fact, based on (2.1) it was thought to be possible to produce thinner ribbons with lower heat removal rates [44]. However, Kellerman’s experiments did not match the theory. An intense amount of heat removal was required to produce sheets at the low speed of 0.5 mm/sec. A pull speed limit was observed experimentally, beyond which the ribbon would be pulled out of the furnace and the process would halt. This up-

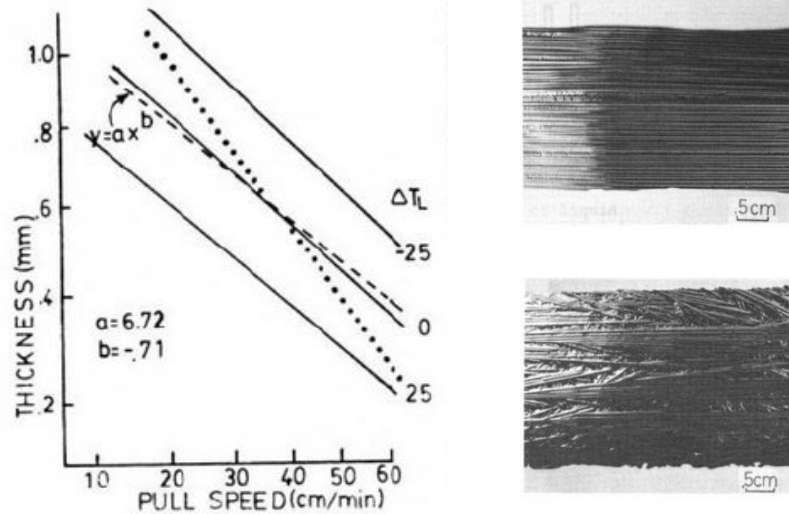


Figure 2.3: (left) The pull speed v.s. thickness data for the LASS process. We see that the thickness of the sheet from the LASS process is comparable to the ones produced by Kudo. However, the cooling provided in the LASS process was much more focused which allowed for better results. (right) Two experimental samples from the LASS process with aligned dendrites (top right) and random dendrites (bottom right).

per limit to the pull speed was documented for the first time in HRG literature and could not be explained by any of the traditional heat transfer models known at that time. An observation from experiments at Varian was the formation of a $\{111\}$ facet at the growth tip of the crystal as shown in 2.4. The limitation to pull speed was attributed to the existence of this facet since the triangular wedge model of Zoutendyk was no longer applicable. Interestingly, Ciszek [45] had already documented the effects of seed crystal orientation on the facet angle at the growth tip in 1984.

In consultation with Varian Semiconductors, Helenbrook [33] proposed to incorporate crystal growth dynamics in his model to simulate the flat facet at the solidification front. Using initial conditions close to the faceted solution, his models converged and he was

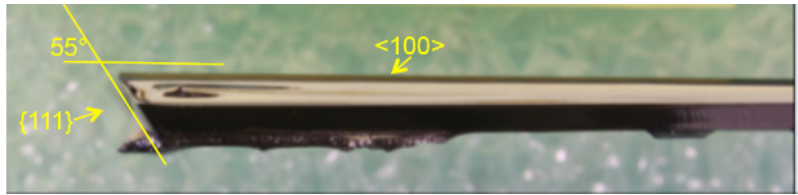


Figure 2.4: Side view of sheet pulled slowly from the furnace. Growth direction is to the left. {111} facet is observed at the leading edge.

able to demonstrate pull speed limit in his simulations. In addition, Helenbrook [35] uses his linear stability analysis to explain the formation of dendrites while operating HRG near the pull speed limit.

Alison Greenlee [46] at MIT developed a heuristic heat transfer model for the faceted edge consistent with Kellerman's experimental observations. Her calculations estimated that majority of the latent heat (70%) was dissipated to the liquid in front of the melt, which help support the high growth rate of the ribbon. Furthermore, her model revealed that it was not possible to make ribbons thinner than 200 microns to be used in solar applications. This instigated patents that involved remelting the solidifying ribbon in order to accomplish desired thickness control [47, 44]. Alison Greenlee would later launch a startup with Peter Kellerman, now called Leading Edge Equipment Technologies, and purchase the intellectual property rights for FSM from Varian.

2.3 Challenges and thesis overview

Despite the proposed advantages, the HRG process faces three major challenges towards successful commercialization. The first one is the problem of melt spilling over from crucible during ribbon extraction [25]. Melt spill over leads to material loss, which increases costs and disrupts the stable operation of the process. In addition, the full range of stable and unstable modes of the HRG process are not known. Chapter 3 uses Weierstrass' variational theory to calculate stable operating ranges for ribbon growth processes.

The second challenge is producing good quality silicon wafers at high production speed. Currently, wafers produced using the HRG process are thick and do not meet industry standards. On top of that, the economic viability of the process is highly dependant on increasing the production speed of the process beyond a certain threshold limit. Experiments show a strict limitation on the production speed, below the threshold limit. Current models of crystal growth cannot explain the observed limitations in pull speed and thickness. Chapter 4 develops a numerical model based on conservation laws to simulate the observed limitations. Results from the simulations are used to develop inverse models for scaling and control applications.

The third challenge is that the physics at the triple junction, which is also the first to solidify point, is not well understood. A guided physical understanding can help to explain the experimental limitations, providing a mechanism to improve high-speed crystal growth. In Chapter 5, we derive constraints imposed by conservation laws at the triple junction. A cellular automata model is proposed to simulate the single and dual facet shapes observed in experiments.

This thesis serves as a guidebook—with the history, current limitations, suggestions for improvement—for silicon wafer production using the Horizontal Ribbon Growth process. Moreover, the thesis builds on a wider set mathematical tools, which can be used to model other kinds of solidification processes as well. The following chapters look at the three major challenges and the proposed solutions in greater detail.

Chapter 3

Weierstrass' variational theory for analyzing meniscus shape and stability

We use the method of free energy minimization to analyze static meniscus shapes for crystal ribbon growth systems. To account for the possibility of multivalued curves as solutions to the minimization problem, we choose a parametric representation of the meniscus geometry. Using Weierstrass' form of the Euler-Lagrange equation we derive analytical solutions that provide explicit knowledge on the behavior of the meniscus shapes. Young's contact angle and Gibbs pinning conditions are analyzed and shown to be a consequence of the energy minimization problem with variable end-points. For a given ribbon growth configuration, we find that there exist multiple static menisci that satisfy the boundary conditions. The stability of these solutions is analyzed using second order variations and are found to exhibit saddle node bifurcations. We show that the arc length is a natural representation of a meniscus geometry and provides the complete solution space, not accessible through the classical variational formulation. We provide a range of operating conditions for hydro-statically feasible menisci and illustrate the transition from a stable to spill-over configuration using a simple proof of concept experiment.

3.1 Introduction

These investigations, which have found their confirmation in striking agreement with careful experiments, are among the most beautiful enrichments of natural science that we owe to the great mathematician.

— Carl Fredrich Gauss on Laplace’s theory of capillary action, which was later refined by him into its modern variational form.

The Young-Laplace equation was developed by Thomas Young [48], who provided a qualitative theory for surface tension, and Pierre-Simon Laplace [49], who mathematically formalized the relationship described by Young. This theory was later refined by Carl Fredrich Gauss [50] using Bernoulli’s principle of virtual work. Using the fundamental principles of dynamics, he derived the Young-Laplace equation and Young’s contact angle condition from a single variational framework. He argued that the energy of a mechanical system in equilibrium is unvaried under arbitrary virtual displacements consistent with the constraints. This spirit of variational analysis is still used in practice to describe the meniscus shape in interface problems.

The existence of a static meniscus plays a critical role in capillary-shaped ribbon growth systems such as the Dendritic web growth [51], Edge-defined Film Growth [52], Low Angle Silicon Sheet growth [53], and the Horizontal Ribbon Growth process [37]. In these processes, the ribbon shape is supported by the formation of a stable meniscus and grows without touching any external surface like the crucible wall. This prevents the formation of defects during solidification and allows for the formation of single crystal ribbons [20].

Figure 3.1 describes the schematic of a Horizontal Ribbon Growth (HRG) process which will serve as an example to illustrate the application of our theory. A bath of molten substrate is cooled from the top to form a thin ribbon of single crystal which is continuously extracted. A narrow helium cooling jet is used to provide intense cooling for solidification and keeps the starting point of the ribbon almost fixed for all feasible pull speeds [33]. A seeding process takes place at the outlet while the melt is being continuously replenished at the other end. Thin sheets of single crystal can be pulled at relatively high speeds due to enhanced heat transfer with the surroundings [54]. This provides an advantage over the present crystal growing methods, like the Czochralski process, where the sheets are prepared by slicing a single crystal boule followed by tedious, time consuming grinding

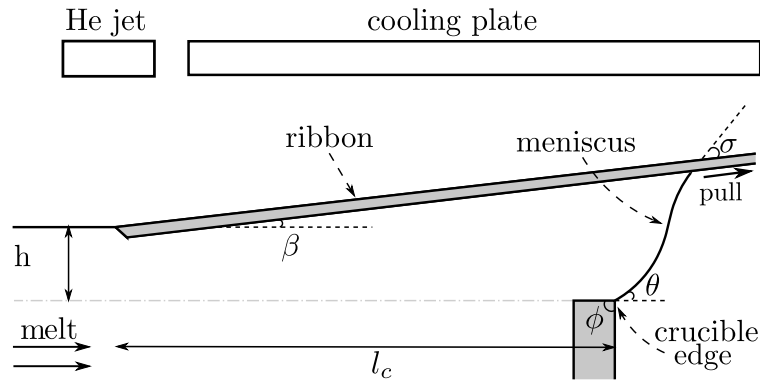


Figure 3.1: Schematic for a horizontal crystal ribbon growth process. The formation of a meniscus at the end of the crucible is essential for steady state operation

and lapping operations which result in a large percentage of the original crystal being wasted [14]. The weight of the ribbon is supported by the melt, which forms a meniscus between the ribbon and the edge of the crucible, thereby reducing the mechanical stresses on the crystal.

Several well known ribbon growth techniques can be characterized by the angle (β) at which the ribbon is pulled from the melt as illustrated in Figure 3.2. For the case when $\beta = 90^\circ$, the ribbon is pulled perpendicular to the surface of the melt and relates to the family of vertical ribbon growth techniques such as the Edge-defined Film Growth (EFG), and the Dendritic web (WEB) growth processes. In the EFG process, the role of the crucible in the previous example is substituted by a melt-wettable die which provides a pinning boundary for the meniscus. The die determines the shape of the meniscus and thus the cross section of the growing crystal ribbon [55]. This makes it important to understand the meniscus geometry in order to study its effect on crystal shape and quality.

Another family of ribbon growth methods, characterized by their low pull angles, are the Low Angle Silicon Sheet (LASS) process, and the Horizontal Ribbon Growth (HRG) process [56, 44]. These methods have the advantage of having a large solid-liquid interfacial area making it easier for the latent heat to dissipate and leading to higher produc-

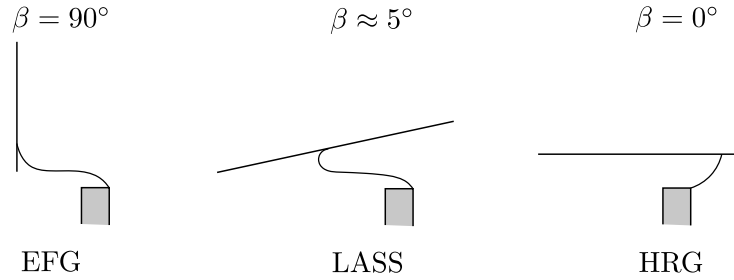


Figure 3.2: Characterization of the ribbon growth family based on pull angle (β)

tion speeds. However, two technical issues appear while operating these processes: the ribbon freezing onto the crucible (down-growth) and the melt spilling-over the crucible (spill-over) [28, 26, 25]. These two issues are directly related to the formation of a short or unstable meniscus between the ribbon and the crucible edge [43, 42, 37].

The main objective of this paper is to analyze these instabilities of the meniscus for the horizontal ribbon growth processes, while at the same time keeping the analysis general enough to be extended to other problems of physical or engineering importance.

The meniscus profiles for HRG were first investigated by Rhodes et al. [36] around the same time as Kudo [28] performed his first HRG experiments with silicon. They developed a mathematical model based on hydrostatics, to describe the shape of the meniscus that must be formed between the ribbon and the crucible edge. They found that the hydrostatically feasible configurations require the meniscus to be “taller” than the melt height, and that the ribbon be pulled at a slight angle, which coincided with Kudo’s experimental operation. In 2012, Daggolu et al. [43, 42, 41] constructed a thermal-capillary model describing the interaction between fluid flow and heat transfer in a HRG system. In their results they captured the critical nonlinearities in the system, such as the existence of multiple steady states for a given pulling speed. The problems of melt spilling over and freezing to the crucible were assessed by doing a sensitivity analysis on the length of the meniscus as a function of melt height and pull angle [42]. Multiplicity of steady states with respect to pull speeds have also been observed in the case of EFG process [57, 58]. This multiplicity is

manifested as two states of the ribbon thickness for the same pull speed but with different failure limits [59].

Classical variational analysis has proven useful in the study of meniscus stability for capillary based processes. For the Czochralski process, Mika and Uelhoff [60] used free energy minimization along with the concepts of variational calculus to numerically determine instability conditions for the meniscus. Mazuruk and Volz [61, 62] addressed the static stability problem for the Bridgman process using numerical simulations to calculate the sign of the second order variations for the governing free energy formulation. Using the observation that the angle between the crystal and the melt should converge towards a constant value, 11° for the case of silicon, Surek [63] developed a theory for shape stability in capillary shaped crystal growth systems based on deviations from this angle. Dynamic and static stability was numerically addressed by Tatartchenko [64] using Lyapunov based techniques and variational principles.

Outside the area of crystal growth, variational principles have been used to prove the existence and stability of menisci shapes for different capillary geometries [65]. A similar approach has been used by Pitts [66] and Vogel [67] to study the shape of liquid pendant drops and identify regions of stability before the drop breaks. Soligno et al. [68] implemented a numerical method to minimize thermodynamic potential function and calculate the interface shape of liquids for various wall geometries. Lawal and Brown [69, 70] used polar coordinates in their variational formulation to obtain multiple critical solutions for their drop geometries on an inclined surface. They observed that for a fixed Bond number, axisymmetric sessile shapes on horizontal surfaces lose stability at a drop volume that corresponds to a point of bifurcation into a family of asymmetric shapes. As we shall see in Section 3.6, the ribbon growth configuration also admits a point of bifurcation into stable and unstable families of menisci.

Very recently Oliveros et al. [37] used the classical variational approach to find existence and stability conditions for menisci in a HRG process. The analysis showed that stationary

menisci arising as solutions to the classical Euler-Lagrange equation were stable as long as the solution satisfied the existence conditions. Due to the well known complexity and non-linearity of the ribbon growth systems, we were left with the question of whether or not the system had any unstable configurations that can't be captured by the traditional variational tools. In Weierstrass' variational theory this limitation is overcome by formulating the geometry of the meniscus in parametric form [71]. This approach allows for the possibility to find stationary curves described by multi-valued functions (Figure 3.3), which help expand the solution space. We refer the readers to Oliveros [72] for further details on the development of the theory.

It is important to note that heat transfer and fluid flow also play a critical role in capillary shaped crystal growth processes [73, 74]. However here we decouple these phenomena and focus only on the static stability of the meniscus in absence of heat transfer. In doing so, we are able to provide explanations to phenomena like multiplicity of steady states as observed in the EFG and HRG processes [42, 57] and the existence of destabilizing multi-valued menisci in crystal growth systems [75, 76], among others, using a first principles approach.

3.2 Problem Statement

The free energy (ΔU) of the three phase system consisting of a rigid fixed ribbon, a gas and a liquid bounded by the interface $x = x(y)$, as seen in Figure 3.3, is given by the expression [37]:

$$\Delta U = \int_0^H -\Delta P x dy + \gamma \sqrt{1 + x'^2} dy = \int_0^H F(x, y, x') dy. \quad (3.1)$$

The right-hand side is divided into two terms. The first term represents the potential energy due to hydrostatic pressure (ΔP). The second term represents the free surface energy of the interface due to surface tension (γ). H is the maximum height of the meniscus and corresponds to the length of integration in the vertical direction in the Cartesian co-

ordinate system. The Euler-Lagrange equation for the variational problem that results from minimizing the free energy gives the Young-Laplace equation:

$$\Delta P + \gamma \frac{x''}{(1+x'^2)^{3/2}} = 0. \quad (3.2)$$

Analytic solutions have been developed for the Young-Laplace equation (3.2) in 2 and 3 dimensions using Legendre elliptic functions [37, 77]. However, in some cases the solution to geometric problems that use the classical variational formulation cannot be described by functions of the form $x = x(y)$ in a Cartesian coordinate system. For example, the multi-valued meniscus of a non-wetting sessile drop on an incline plane cannot be described using single-valued functions [78, 70]. A similar problem exists in describing the full spectrum of minimum energy curves for ribbon growth systems. The stationary curves arising from free energy minimization are often multi-valued and therefore require a less restricting and more “natural” representation. By choosing the arc length as a parametric variable, we see the emergence of a natural representation of the meniscus shape which allows us to find the complete solution space. These interface curves are also shown to share similarities with the family of Euler’s elastic curves.

3.3 Free energy reformulation in parametric form

Instead of denoting the interface in a Cartesian frame as $y = y(x)$ or $x = x(y)$, we represent them in parametric form $x(s), y(s)$. The parameter s is chosen such that $x(s)$ and $y(s)$ come out as single valued functions with respect to the parameter. The reformulated free energy expression with respect to the parameter s is

$$\Delta U = \int_0^{s_t} -\Delta P xy' ds + \gamma \int_0^{s_t} \sqrt{x'^2 + y'^2} ds = \int_0^{s_t} g(x, y, x', y') ds, \quad (3.3)$$

where s_t is the total length of integration. The first term accounts for the hydro-static energy of the system. Due to the presence of gravity, the pressure in the liquid is given as a function of height, $\Delta P = \rho g_r (h - y)$, where ρ is the density of the liquid and g_r is the

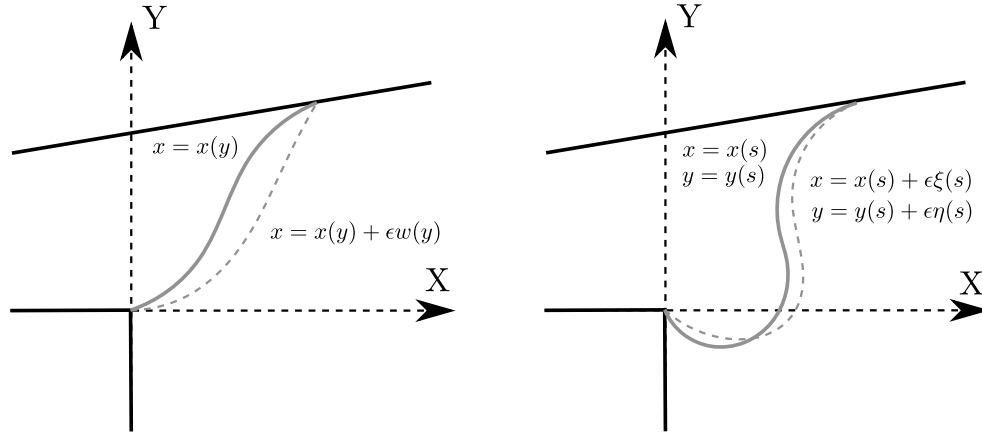


Figure 3.3: (left) Stationary curves arising from the solution of the classical Euler-Lagrange equation yield single valued functions of the type $x(y)$. (right) Weierstrass' variational approach expand the solution space to account for multi-valued stationary curves, described by curves of the type $x(s)$ and $y(s)$.

acceleration due to gravity. The second term represents the surface energy of the interface due to interfacial tension γ .

In performing this transformation, the value of ΔU must remain invariant for any type of parametric form chosen for x and y . Weierstrass showed that the necessary and sufficient condition for the invariance of ΔU is that the function g be homogeneous and of degree one in the variables x' and y' [71, p. 118], i.e.

$$g(x, y, kx', ky') = kg(x, y, x', y'), \quad (3.4)$$

where the prime represents differentiation with respect to s . From this homogeneity condition, there follow several relationships between the partial derivatives of G , which are useful in constructing the expressions for the first and second variation of ΔU .

Non-dimensionalizing length scales with respect to the capillary length, $\lambda_c = \sqrt{\gamma/(\rho g_r)}$ yields,

$$\begin{aligned}\mathcal{U}(X, Y) &= \int_0^{S_t} (Y - H)XY'dS + \sqrt{X' + Y'}dS \\ &= \int_0^{S_t} G(X, Y, X', Y')dS,\end{aligned}$$

where $\Delta U = \gamma \lambda_c \mathcal{U}$, $x = \lambda_c X$, $y = \lambda_c Y$, $s_t = \lambda_c S_t$ and $h = \lambda_c H$. The homogeneity condition is not affected by non-dimensionalization.

3.4 Stationary curves via the first variation

The objective is to find conditions on the stationary curves $X(S), Y(S)$ that set the first variation of \mathcal{U} to zero. This exercise leads to the well known Young-Laplace equation in parametric form. However, we briefly provide some important steps in the derivation as they will be useful in developing the forthcoming stability analysis.

Let $\epsilon \xi(S)$ and $\epsilon \eta(S)$ be small perturbations to the curves $X(S)$ and $Y(S)$, with ϵ as small as desired. The end points on the curve are kept fixed i.e. ξ and η are taken to be zero at the end points. The energy of this neighbouring curve is given by

$$\mathcal{U}(X + \epsilon \xi, Y + \epsilon \eta) = \int_0^{S_t} G(X + \epsilon \xi, Y + \epsilon \eta, X' + \epsilon \xi', Y' + \epsilon \eta')dS.$$

Applying Taylor's formula to the integrand, we obtain that

$$\begin{aligned}\mathcal{U}(X + \epsilon \xi, Y + \epsilon \eta) &= \mathcal{U}(X, Y) + \epsilon \delta \mathcal{U} + \frac{\epsilon^2}{2} \delta^2 \mathcal{U} + O(\epsilon^3) \\ \delta \mathcal{U} &= \int_0^{S_t} \left(\xi G_X + \xi' G_{X'} + \eta G_Y + \eta' G_{Y'} \right) dS.\end{aligned}$$

We call $\epsilon \delta \mathcal{U}$ the first variation of the energy functional \mathcal{U} . For $X(S), Y(S)$ to be a critical point of \mathcal{U} , we infer that $\delta \mathcal{U} = 0$, i.e.,

$$\int_0^{S_t} \left(\xi G_X + \xi' G_{X'} + \eta G_Y + \eta' G_{Y'} \right) dS = 0, \quad (3.5)$$

for otherwise, we could increase or decrease the value of \mathcal{U} by choosing ϵ to be of the same or a different sign of the integral in (3.5), respectively.

Using integration by parts and assuming continuous derivatives of the functions involved, we arrive at the Euler-Lagrange equations:

$$G_X + \frac{dG_{X'}}{dS} = 0, \quad G_Y + \frac{dG_{Y'}}{dS} = 0 \quad (3.6)$$

Due to the homogeneity condition (3.4), the two equations in (3.6) are not independent of each other, as we proceed to show. Differentiating (3.4) with respect to k , and substituting $k = 1$, yields

$$X'G_{X'} + Y'G_{Y'} = G. \quad (3.7)$$

Differentiating this expression with respect to X' or Y' , we obtain

$$\frac{1}{Y'^2}G_{X'X'} = -\frac{1}{X'Y'}G_{X'Y'} = \frac{1}{X'^2}G_{Y'Y'} = G_1, \quad (3.8)$$

where G_1 is the common value of these expressions. Differentiating (3.7) partially with respect to X and Y we get

$$G_X = X'G_{XX'} + Y'G_{XY'}, \quad G_Y = X'G_{X'Y} + Y'G_{Y'Y}. \quad (3.9)$$

Using (3.8),(3.9) in the Euler-Lagrange equation and assuming that X' and Y' don't vanish simultaneously in the interval $[0, S_t]$ we arrive at

$$G_{XY'} - G_{YX'} - G_1(Y'X'' - X'Y'') = 0. \quad (3.10)$$

This equation is the *Weierstrass' form of the Euler-Lagrange equation*. Evaluating the necessary terms we have that

$$G_1 = \frac{1}{(X'^2 + Y'^2)^{3/2}}, \quad (3.11)$$

$$G_{XY'} = Y - H, \quad G_{YX'} = 0. \quad (3.12)$$

So the Euler-Lagrange equation becomes:

$$H - Y = \frac{X'Y'' - X''Y'}{(X'^2 + Y'^2)^{3/2}}. \quad (3.13)$$

3.4.1 Analytic form and family of solutions

The differential equation (3.13) together with an initial condition determines the critical curve, but not the functions $X(S)$ and $Y(S)$. In order to find these functions we must add a second equation or differential relation between S, X, Y . This additional relation should be such that X and Y come out as single valued functions of S . In order to find analytic solutions to the parametric Young-Laplace equation, we make the transformation

$$X'(S) = \cos \Omega(S), \quad Y'(S) = \sin \Omega(S), \quad (3.14)$$

where Ω is the tangential angle to the meniscus. These substitutions define the independent variable S to be the arc length of the meniscus and turn the Young-Laplace equation into

$$\Omega'(S) = H - Y. \quad (3.15)$$

This transformation splits the Young-Laplace equation into a system of 3 ODEs. We set the initial conditions of the meniscus to have general pinning conditions

$$X(0) = 0, \quad Y(0) = 0, \quad \Omega(0) = \theta.$$

To find an analytic solution to the system of ODE's we differentiate (3.15) and substitute (3.14) to find

$$\Omega''(S) = -\sin(\Omega(S)). \quad (3.16)$$

We observe that the dynamics of the tangent angle (Ω) are similar to the dynamics of a pendulum or an elastic rod [79, p. 265]. Multiplying (3.16) with $\Omega'(S)$ and integrating, we get,

$$\frac{1}{2}\Omega'^2 - \cos \Omega = A, \quad (3.17)$$

where A is the constant of integration. For a simple pendulum, A defines the energy of the system. In our case, A represents the horizontal force balance of hydrostatic pressure, $\frac{1}{2}\rho g(h - y)^2$, and surface tension, $\sigma \cos \Omega$, along any longitudinal cross section of the

meniscus. Using the initial conditions $\Omega(0) = \theta$ and $\Omega'(0) = H$, we evaluate the integration constant as,

$$A = \frac{H^2}{2} - \cos \theta. \quad (3.18)$$

Using the trigonometric identity $\cos \Omega = 1 - 2 \sin^2 \Omega/2$, we arrive at

$$\Omega'(S) = 2\sqrt{\frac{A+1}{2} - \sin^2 \frac{\Omega}{2}}. \quad (3.19)$$

The solution to this differential equation can be explicitly written down in terms of Legendre elliptic and Jacobi amplitude functions,

$$\Omega(S) = 2 \operatorname{am}\left(\sqrt{\frac{1+A}{2}}S + F\left(\frac{\theta}{2}\middle|\frac{2}{1+A}\right)\middle|\frac{2}{1+A}\right), \quad (3.20)$$

where $F(u|m)$ is the incomplete elliptic integrals of the first kind and $\operatorname{am}(u|m)$ is the Jacobi amplitude function. $Y(S)$ can be calculated directly using (3.15) and the identity $\operatorname{am}(u, k) = \int_0^u \operatorname{dn}(u', k) du'$ to be

$$Y(S) = H - \sqrt{2(1+A)} \operatorname{dn}\left(\sqrt{\frac{1+A}{2}}S + F\left(\frac{\theta}{2}\middle|\frac{2}{1+A}\right)\middle|\frac{2}{1+A}\right), \quad (3.21)$$

where $\operatorname{dn}(u|m)$ is the Jacobi delta amplitude function. Using the result (3.15), (3.17) and (3.21) into the expression for $X'(S)$ in (3.14) we obtain

$$\begin{aligned} X(S) &= \sqrt{2(1+A)} E\left(\operatorname{am}\left(\sqrt{\frac{1+A}{2}}S + F\left(\frac{\theta}{2}\middle|\frac{2}{1+A}\right)\middle|\frac{2}{1+A}\right)\middle|\frac{2}{1+A}\right) \\ &\quad - \sqrt{2(1+A)} E\left(\frac{\theta}{2}\middle|\frac{2}{1+A}\right) - AS. \end{aligned} \quad (3.22)$$

$E(u|m)$ is the incomplete elliptic integral of the second kind.

Using these analytic expressions, we plot the interface for different values of pinning angle θ as shown in figure 3.4. For the purpose of this illustration, we consider the non-dimensional melt height H to be 1 as the pinning angle θ is varied. Figure 3.4 shows parametric plots of $X(S)$ and $Y(S)$ at $H = 1$ and for some chosen values of θ using (3.21) and (3.22). The curves are periodic and can extend in length from $(-\infty, \infty)$. The origin can therefore be taken to be any point where the curve makes an angle θ with the horizontal.

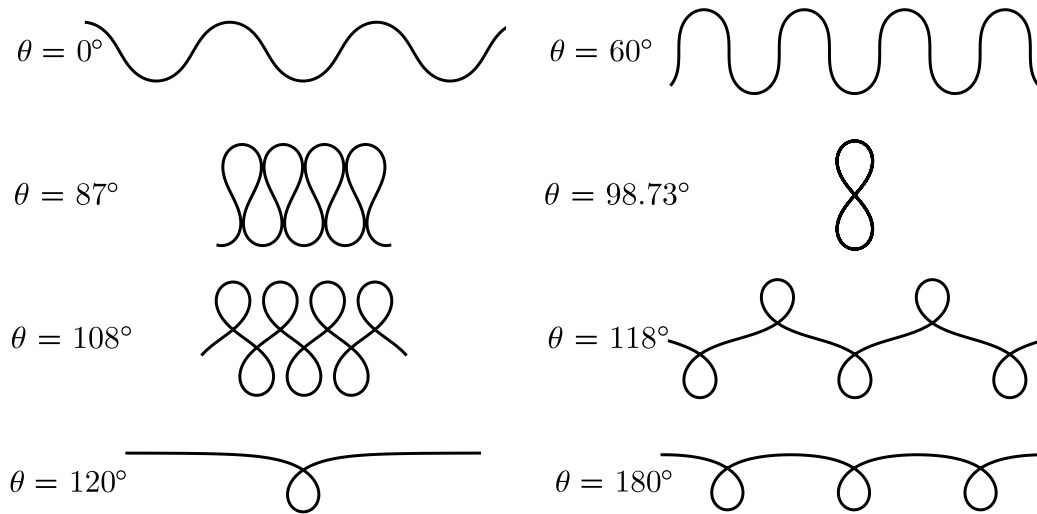


Figure 3.4: Family of solutions for the parametric Young-Laplace equation

Plotting for $A > 1$ might require certain inversion transformations. These along with other identities in this section can be found in Abramowitz and Stegun [80].

Certain sections of the curves in Figure 3.4 closely resemble pendant or droplet like shapes. The similarity of these solutions also extend to the family of elastic curves discovered by Euler as a part of his elastica problem [81]. Depending on the second order stability condition, a portion of these curves will form a stable meniscus to the ribbon growth process. This condition will be derived in the following section.

3.5 Stability analysis via the second variation

In this section we consider the stability of the critical curves when the end-points are considered fixed. Using Taylor series representation, the second variation in parametric form is expressed as:

$$\delta^2 U_0 = \int_0^{S_t} \delta^2 G dS, \tag{3.23}$$

where

$$\begin{aligned} \delta^2 G = & G_{XX}\xi^2 + 2G_{XY}\xi\eta + G_{YY}\eta^2 + 2G_{XX'}\xi\xi' + 2G_{YY'}\eta\eta' + \\ & 2G_{XY'}\xi\eta' + 2G_{YX'}\eta\xi' + G_{X'X'}\xi'^2 + 2G_{X'Y'}\xi'\eta' + G_{Y'Y'}\eta'^2. \end{aligned} \quad (3.24)$$

In order for the curve described by $Y(S)$ and $X(S)$ to be a minimum—and therefore stable—its second variation should be positive; so the value of the integral above must be always positive in the range of integration. Using a lengthy factorization, Weierstrass transformed the second variation into the classical quadratic functional

$$\delta^2 U_0 = \int_0^{S_t} \left[G_1 \left(\frac{d\omega}{dS} \right)^2 + G_2 \omega^2 \right] dS. \quad (3.25)$$

In our application we find from (3.24)

$$\omega = Y'\xi - X'\eta,$$

and G_2 satisfies the following relationships:

$$G_2 = \frac{L_2}{Y'^2} = \frac{M_1}{-X'Y'} = \frac{N_1}{X'^2},$$

with

$$\begin{aligned} L_2 &= G_{XX} - Y''G_1 - \frac{dL_1}{dS}, \\ M_2 &= G_{XY} + X''Y''G_1 - \frac{dM_1}{dS}, \\ N_2 &= G_{YY} - X''^2G_1 - \frac{dN_1}{dS}, \\ L_1 &= G_{XX'} - Y'Y''G_1, \\ M_1 &= G_{XY'} + X'Y''G_1 = G_{YX'} + Y'X''G_1, \\ N_1 &= G_{YY'} - X'X''G_1. \end{aligned}$$

The form of the integral (3.25) allowed Weierstrass to apply the classical results of the calculus of variations. Namely, Legendre's necessary condition and Jacobi's test. Legendre's necessary condition for a minimum requires that

$$G_1 \geq 0, \quad (3.26)$$

along the stationary curve described by $X(S)$ and $Y(S)$.

Jacobi's test requires that the solution to the differential equation,

$$G_2u - \frac{d}{dS} \left(G_1 \frac{du}{dS} \right) = 0, \quad (3.27)$$

must not have conjugate points in the integration interval, i.e:

$$u(S) \neq 0 \quad 0 < S < S_t.$$

For otherwise if $u(S) = 0$, it is possible to find a perturbation centered around S such that the second variation is negative.

The Legendre test is satisfied by virtue of (3.11). In order to have the Jacobi test satisfied we require that the solution to the differential equation

$$G_2u - (G_1u')' = \frac{Y'''}{Y'}u - u'' = 0, \quad (3.28)$$

must not have conjugate points in the interval of integration. Equation (3.28) is equivalent to:

$$(Y'u' - Y''u)' = 0.$$

Thus, we obtain that for some constant K_1 ,

$$Y'u' - Y''u = K_1.$$

Dividing the expression above by Y'^2 we get:

$$\frac{Y'u' - Y''u}{Y'^2} = \left(\frac{u}{Y'} \right)' = \frac{K_1}{Y'^2}.$$

So the condition for stability becomes

$$u(S) = K_1 Y'(S) \int_0^S \frac{dS}{Y'(S)^2} \neq 0 \text{ for } 0 < S < S_t. \quad (3.29)$$

The integral in (3.29) is always positive as long as $Y'(S) \neq 0$ in the interval $0 < S < S_t$ (given $S_t > 0$), otherwise the integral does not converge. The term $K_1 Y'(S)$ does not

change sign as long as $Y'(S)$ does not change sign in the $(0, S_t)$ interval. Therefore the issue of stability reduces to finding the range of values for which $Y'(S)$ crosses zero in the range $(0, S_t)$. This is easier to analyse recalling from (3.14) the fact that $Y'(S) = \sin \Omega(S)$, where $\Omega(S)$ is the tangential angle of the meniscus with respect to the horizontal axis. If $\sin \Omega(S)$ is always positive or always negative in the integration interval, the function $u(S)$ will have no conjugate points and the Jacobi test is satisfied. Thus we simplify our stability criterion (3.29) to the following expression:

$$\sin(\Omega(S)) \neq 0 \quad \forall S \in (0, S_t), \quad (3.30)$$

3.6 Results

We apply the theory developed in the previous sections to study the menisci of silicon ribbon growth while keeping in mind that they can be applied to a range of other problems of physical and engineering importance such as finding the size and stability properties of droplets. To characterize figure 3.1 in more detail, the edge of the crucible is considered to be rectangular ($\phi = 90^\circ$). One end of the meniscus is considered to remain pinned at the edge of the crucible and the other end to intersect the ribbon at a fixed angle (σ). The nature of the angle (σ) depends on whether solidification or melting takes place at the triple point, in which case σ is either the growth angle or the contact angle respectively. To maintain consistency in our analysis and for the sake of convenience, we assume σ to be a constant value of (11°) across all operating conditions. The pull angle (β) and the height of the melt (h) serve as degrees of freedom. It is of interest to find stable operating regimes for the meniscus over the parameter space of β and h . The required material properties are summarized in table 3.1 and are used to dimensionalize the equations and the results.

The plot on the left in Figure 3.5 describes the various stationary meniscus shapes for a representative pulling angle of $\beta = 5^\circ$ and melt height $h = 5.35$ mm ($H = 1$). We use the analytic expressions for $x(s)$ and $y(s)$, with different θ values to plot the interface curves

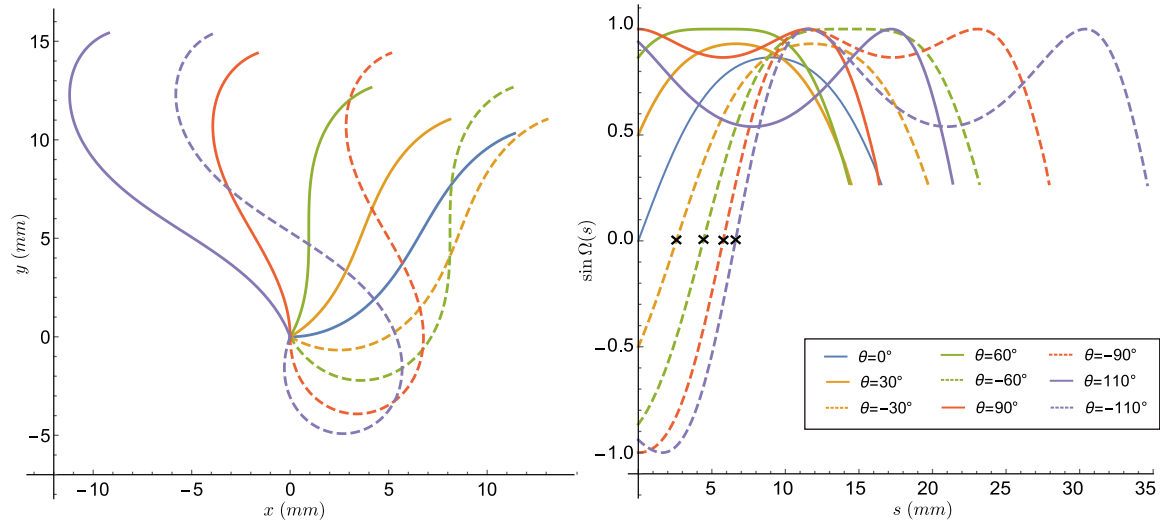


Figure 3.5: (left) Stationary meniscus shapes obtained using the analytical solution in parametric form. Curves correspond to a value of $\beta = 10^\circ$ and $h = 5.35 \text{ mm}$. (right) The sine of the tangent angle $\Omega(s)$ for different pinning angles. The curves crossing zero correspond to the unstable modes.

Parameter	Symbol	Value
Density of liquid silicon	ρ	2570 [kg m^{-3}]
Acceleration due to gravity	g_r	9.8 [m s^{-2}]
Surface tension of silicon	γ	0.72 [J m^{-2}]
Triple point angle	σ	11°
Melt-graphite wetting angle	θ_e	30°

Table 3.1: Material properties and parameters used in the illustrative example.

and stop when the interface reaches the angle of $\sigma + \beta$. In order to show the concept of static stability, we focus on the results obtained from Jacobi's test (Legendre's condition for a minimum is always satisfied for all meniscus shapes). The plot on the right in Figure 3.5 shows the sine of the tangential angle as a function of the arc length. As we mentioned before, the sine of the tangential angle must not vanish between 0 and s_t . From the figures we show that menisci in which the pinning angles are greater than zero are statically stable, whereas the curves for values of pinning angle lower than zero cross the horizontal axis. The family of stable and unstable curves converge in the limit $\theta \rightarrow 0$.

Let x^* and y^* be the parametric coordinates describing the equation for a ribbon. We assume the shape of the ribbon to be a straight line starting from $l_c = -5.35\text{cm}$ ($L_c = -10$) and represented by

$$L(x^*, y^*) = (y^* - h) - \tan \beta(x^* - l_c) = 0.$$

The desired solution is then given by any curve described in Figure 3.5, whose end point lies on this line. This can be formulated as a boundary value problem:

$$\begin{aligned} x(0) &= 0 & y(0) &= 0 \\ \Omega(s_t) &= \beta + \sigma & L(x(s_t), y(s_t)) &= 0 \end{aligned} \quad (3.31)$$

We use a Newton-Raphson solver to find curves that satisfy (3.31). Two curves, one stable and one unstable, are found and illustrated in Figure 3.6 along with a diagram of the system (to scale) to better visualize the concept of hydro-static stability.

3.6.1 Effect of pull angle

The shape of the meniscus is influenced by the pull angle (β) through the boundary conditions described in (3.31). To get a better description of the meniscus multiplicity observed above, we vary the pulling angle to evaluate the feasibility of stationary menisci. Figure 3.7 provides a description of the solution space for a melt height of $h = 5.35\text{mm}$ as a function of the pulling angle. The choice of meniscus length as the Y-axis was motivated from

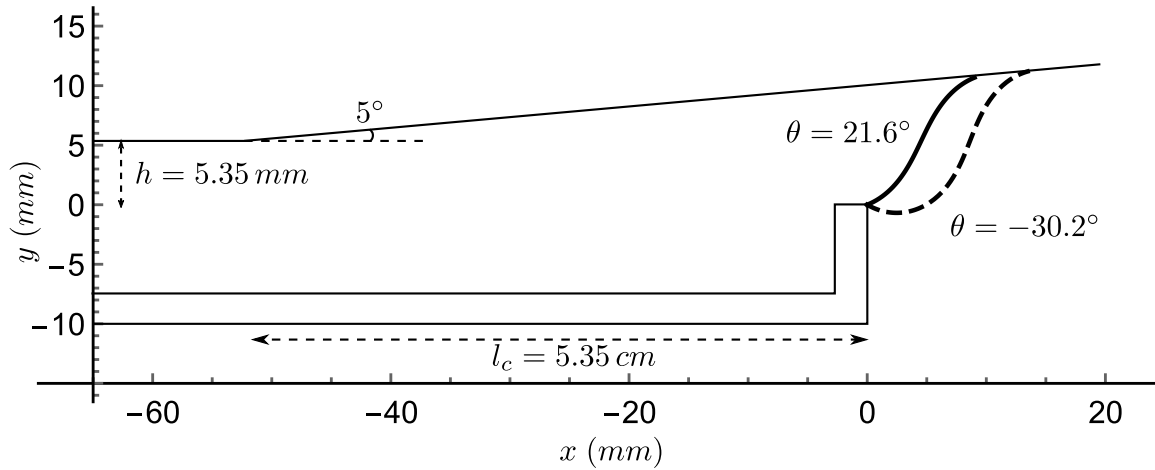


Figure 3.6: Hydro-statically stationary configuration for a melt level of 5.35 mm and a pulling angle of 5° . The solid curve corresponds to a statically stable configuration and the dashed curve corresponds to an unstable configuration.

literature on elasticity and bifurcation theory [82].

Representative meniscus shapes are drawn along the solution curves to describe their geometry for a few choice of pull angles. The dashed curves describe the family of unstable solutions, characterized by a point of zero slope where the Jacobi condition is not met. In the neighbourhood of this point, it is possible to perturb the curve such that the second order variation is negative and the solution is not a minimum. Vice versa, the solid curves describe the statically stable solutions which minimize the thermodynamic energy of the system. The pinning condition at the crucible edges due to Gibbs has not been considered here and is commented on separately in Appendix A.

We observe that it is not always possible to find a feasible solution for any given value of pull angle. Such an operational limit was also observed in the thermal-capillary simulations performed by Daggolu et al. [42], however their analysis was limited to the narrow stability region on the left. Two saddle node bifurcations are observed in our analysis that divide the feasible solution space into two disjoint regions. The feasible region on the left has a smaller range of pull angles available for stable operation. The crucible limit shown

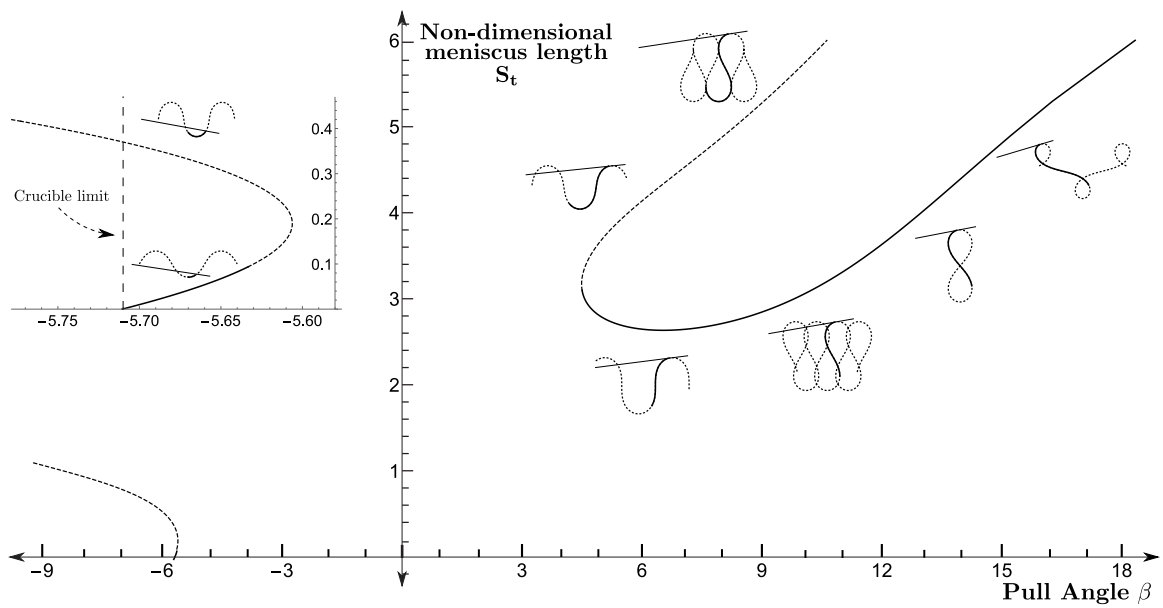


Figure 3.7: Saddle node bifurcations in the meniscus length S_t and pull angle β solution space. Inset: A zoomed up diagram of the solution space for negative pull angles. Solid lines represent stable solutions for which the Jacobi test is satisfied.

inset is the limit at which the meniscus length goes to zero. Decreasing the pulling angle to this limit causes the bottom part of the ribbon to get closer to the crucible edge and result in ribbon freezing onto the crucible. On the other hand, increasing the pull angle beyond the bifurcation point results in the meniscus becoming unstable and causing the melt to spill-over from the crucible.

Given the narrow range of operation for negative pull angles, it would be desirable to operate the ribbon growth process at positive pull angles, beyond 4.5° for the case of $H = 1$, as there is no upper limit to the height of the pulling angles. The feasible region on the right illustrates the variety of meniscus shapes that can be achieved for positive pull angles. The low-angle silicon sheet (LASS) growth process, where the ribbon is extracted from the melt at a slight positive angle with the horizontal takes advantage of this idea. [32].

3.6.2 Effect of melt height

A successful design for a ribbon growth process requires understanding the effect of the melt height (H) on the stability of the meniscus. It is therefore useful to study how the melt height influences the landscape of the solution space described in Section 3.6.1.

Figure 3.8 shows the range of feasible pull angles as the melt height is varied. For example, the portion of the shaded region at $H = 1$ can be thought of as a projection of the feasible pull angles (solid curves) in Figure 3.7 onto the X-axis. Therefore, the entire shaded region in Figure 3.8 describes the existence of a stable meniscus at every point over the parameter space of H and β .

Representative meniscus shapes have been drawn for some chosen values of H and β . At some places, a plus symbol has been used to denote the point where the menisci belong. For $H < 2$ ($h < 10.7\text{ mm}$) we see that it is possible to find a stable meniscus for pull angles as large as 90° . At this point the arrangement corresponds to vertical ribbon growth techniques like WEB, EFG. What is interesting to note is that as the pull angle increases, the meniscus becomes longer and the meniscus-ribbon triple point moves further away from

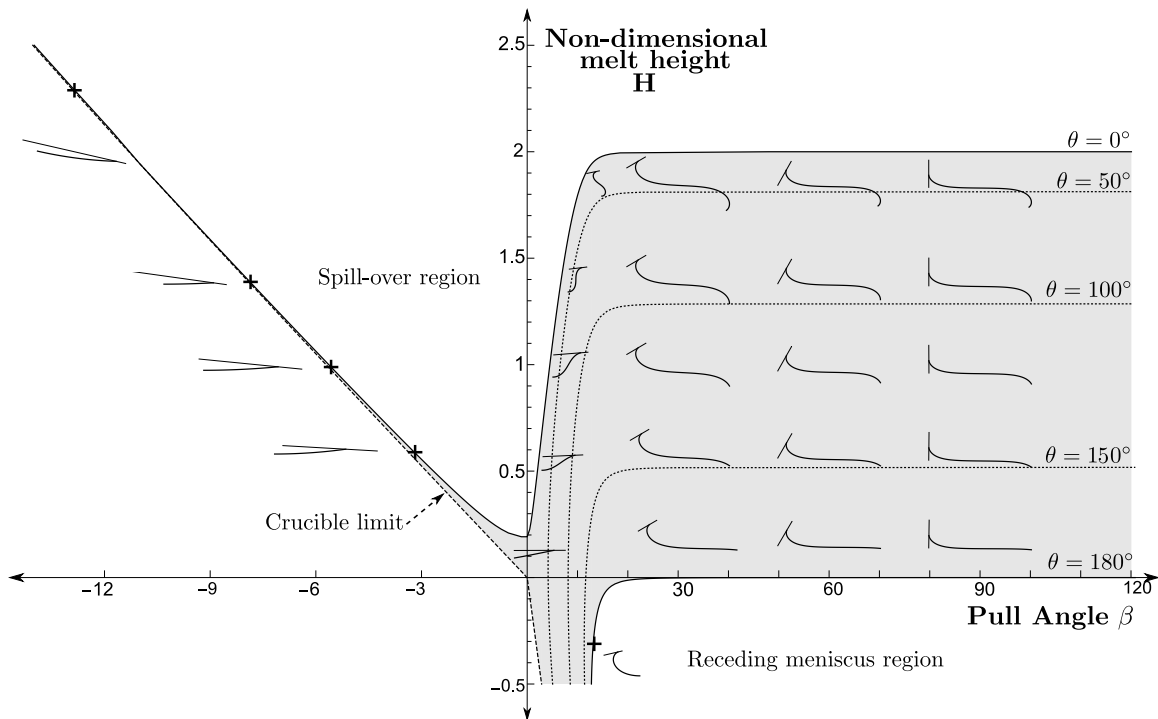


Figure 3.8: Stable meniscus region (shaded) over the parameter space of melt height and pull angle. Representative meniscus shapes have been drawn for melt height and pull angles.

the crucible edge. This observation is the guiding principle behind low-angle silicon sheet (LASS) growth process and circumvents the problem of ribbon freeze-over by moving the triple phase contact point on the ribbon away from the crucible edge.

As the melt height increases, we see that above $H = 0.2$, the feasible solution space splits. The portion in between the regions is the melt spill-over region. In this region it is not possible to form a stable meniscus to support the melt from spilling over the crucible. Since the solution space for positive pull angles is much larger than the negative pull angles, the scale for the negative pull angles has been increased to meaningfully show the feasible solution space. Notice also that there is an upper limit to the height of the melt that the meniscus can accommodate. Beyond this height, a meniscus can no longer exist and the melt spills over from the crucible edge.

The feasibility region shown in Figure 3.8 does not consider the Gibbs inequality condition that arises at the crucible edge. Gibbs' inequality provides a range of pinning angles (θ) at the crucible edge for which the meniscus remains stable. Since the Gibbs limit is a material property and also depends on the geometry of the crucible edge, we provide contours for some chosen pinning angles to find a subset of the feasible (shaded) region that satisfies Gibbs' inequality. The Gibbs pinning condition is derived in appendix A.

3.7 Practical considerations on meniscus shape

We develop a simplified model to determine the shape of upper and lower meniscus for an angled ribbon growth configuration. An explicit formula for approximating the shape of the free surfaces and the length of the solid-liquid interface is derived by using the geometric properties of the syntactrix curve. Results show that the length of the interface decreases with an increase in pull angle, which may provide an additional degree of freedom for controlling ribbon thickness.

Figure 3.9 illustrates a schematic of two free surfaces typically involved in direct growth of ribbon from melt. In this process the ribbon is being withdrawn continuously from a

pool of melt while it is simultaneously being cooled either through radiation or through the use of cooling jets. The ribbon is being pulled at a distance away from the lip of the crucible in order to prevent complications of ribbon freezing onto the crucible/dye lip or the melt spilling over. For this reason, we assume the size of the melt to be infinite. The description of the process has been kept general enough to consider the different ribbon growth processes based on their pull angle (β).

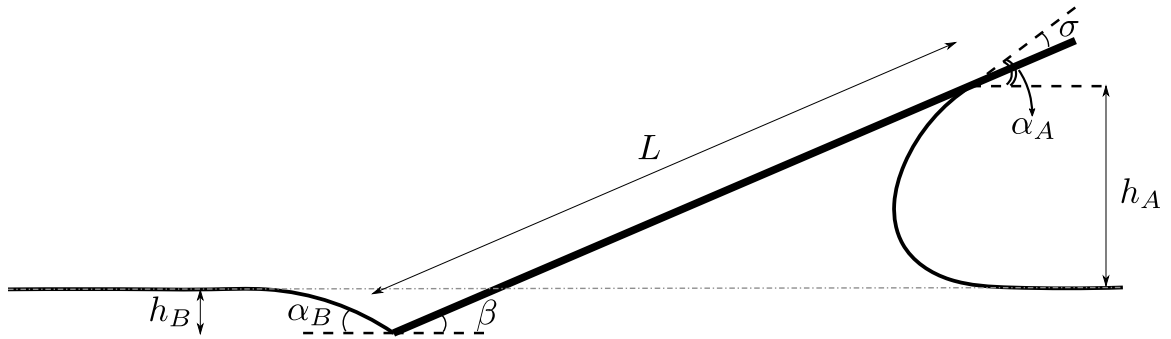


Figure 3.9: A schematic highlighting the quantities of interest to evaluate the distance between the contact points (L)

To reduce model complexity, we assume the ribbon to grow from a pool of melt that is large enough in the horizontal dimension such that the pool appears infinite to the growing ribbon. This assumption may also be practically advantageous, as it is found that growing ribbons close to the crucible walls may cause problems of ribbon freeze-over or meniscus asymmetry. Imagine an infinite pool of melt. A solid sheet of material is held in place on top of the melt such that the sheet induces capillary effect at the upper and lower surface of the sheet. Depending on the angle of inclination (β) chosen and the wettability of the sheet with respect to the melt, the upper and the lower menisci can be above or below the base height, as shown by the dotted gray line in fig. 3.9.

The boundaries of the free surface dictate the length of the ribbon in contact with the melt at equilibrium. We will thus aim to provide a mechanism to determine the process parameter (pull angle) based on the required operating conditions (Length of the ribbon,

shape of the free surfaces etc). Additionally, we assume that the thickness of the ribbon remains fixed for all configurations of ribbon growth considered. This assumption may not be true. However, the dimension of the ribbon thickness is too small to affect the length calculations in a significant way except when the length is of the same order as the thickness.

3.7.1 Theory

Given the condition, $y = h$, $\Omega = \pi$. We use (3.18) to get the value of the constant A as 1. We can therefore substitute this into (3.17) and arrive at

$$y = h \pm 2\lambda_c \cos\left(\frac{\Omega}{2}\right) \tag{3.32}$$

Substituting (3.14) into (3.17), we get,

$$\Omega'(s) = \pm 2 \cos\left(\frac{\Omega}{2}\right) \tag{3.33}$$

We integrate (3.33) to re-arrange to obtain,

$$\cos\left(\frac{\Omega}{2}\right) = \frac{1}{\cosh(s)}, \tag{3.34}$$

with $s = 0$ defined as the point when $\Omega = 0$. Since $\Omega \in [-\pi, \pi]$, only the positive solution to (3.33) is considered.

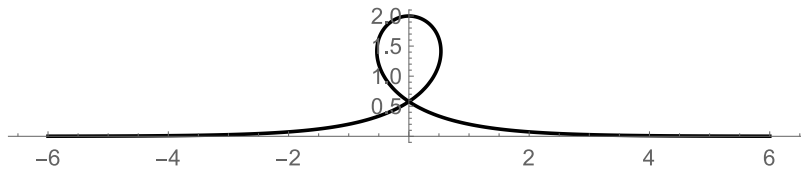


Figure 3.10: The graph of a syntroctrix curve with $h = 0$. The axes are in units of capillary length

Now that we have Ω as a function of s , we can substitute this into equation (3.32) and (3.14) to obtain

$$\begin{aligned} Y &= H \pm \frac{2}{\cosh(S)} \\ X &= S - 2 \tanh(S) \end{aligned} \tag{3.35}$$

The graph for (3.35) is shown in figure 3.10. The curve extends along the arms of the x-axis so it would seem like the ribbon is inside a pool of infinite melt. In practise, a distance of six capillary units from the crucible edge should be sufficient for a reasonable approximation.

3.7.2 Applications

An important equation of interest for the purpose of this paper is the energy equation (3.18) of the convex curve given by:

$$\frac{1}{2}h^2 - \cos \Omega = 1, \tag{3.36}$$

here h is the height of the curve and Ω is the tangent angle of the curve with the horizontal. Using this relation, we can find the meniscus height as a function of the contact angle.

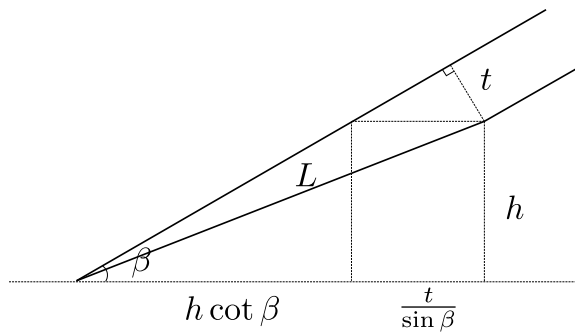


Figure 3.11: Reference schematic for calculating distance between contact points (L)

$$h_B(\alpha_B) = \begin{cases} \sqrt{2 + 2 \cos(\pi - \alpha_B)} & \alpha_B > 0 \\ -\sqrt{2 + 2 \cos(\pi - \alpha_B)} & \alpha_B < 0, \end{cases} \quad (3.37)$$

$$h_A(\alpha_A) = \sqrt{2 + \cos(\alpha_A)}, \quad (3.38)$$

here h_A and h_b are the height of the meniscus on the right (lower) and left (upper) side of the sheet respectively. α_A and α_B are the angles of the two menisci with the horizontal. These angles depend on the inclination angle of the sheet (β) and the growth angle (σ), as given by

$$\alpha_B = \sigma - \beta, \quad (3.39)$$

$$\alpha_A = \sigma + \beta. \quad (3.40)$$

We see that for $\beta < \sigma$, α_B is positive and the left meniscus dips below the zero level of the liquid. When $\beta > \sigma$, the left meniscus rises and behaves similar to the meniscus in the EFG process.

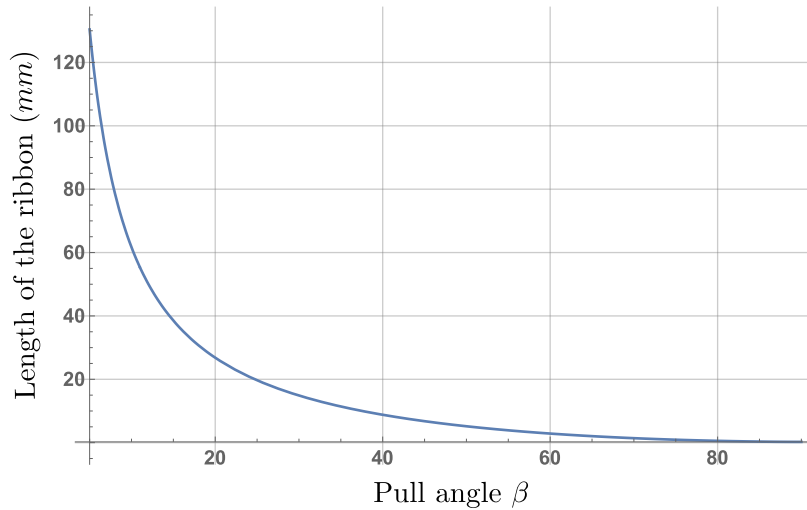


Figure 3.12: Length of the ribbon exposed to the melt as a function of pull angle

Explicit knowledge on the height of the menisci provides us with sufficient information to deduce the distance between the contact points of the two menisci (L). Figure 3.11

provides an illustrative guide to calculate L using the Pythagorean theorem.

$$L(\beta) = \sqrt{(h \cot \beta + t/\sin \beta)^2 + h^2}, \tag{3.41}$$

where $h = h_A + h_B$. t is the thickness of the ribbon, which is assumed to be constant. The thickness of the ribbon is predominantly a consequence of heat transfer. So in the presence of high convective cooling, the thickness of the ribbon can be justified to be fixed.

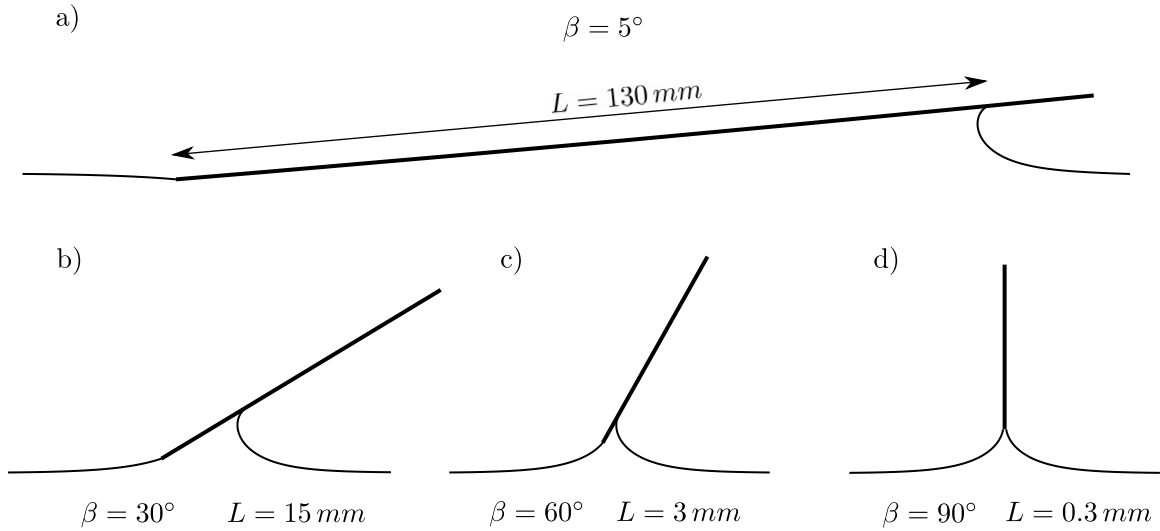


Figure 3.13: Representative diagrams for meniscus shapes in crystal ribbon growth

We use the values provided in table 3.1 to dimensionalize the length scales for a silicon system. Figure 3.12 provides a graph for the relationship between the length of the ribbon in contact with the melt (L) as a function of the pull angle (β).

The graph illustrates an inverse relationship between L and β . For vertical pull angles ($\beta = 90^\circ$), the distance between the contact points is the lowest and is equal to the thickness of the ribbon. As the pull angle is decreased the distance increases until a point where the assumption of an infinite melt is practically no longer valid. The graph is therefore not suitable to predict the interface length for very low pull angles. Figure 3.13 provides to-scale diagrams of the free surface shapes and the interface length for chosen values of pull angles.

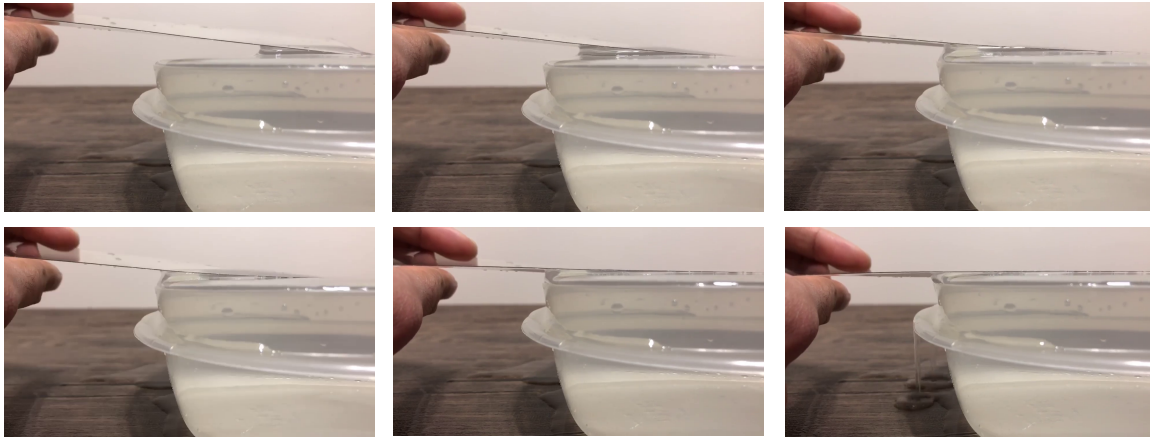


Figure 3.14: A sequence of photographs showing the meniscus spilling over from the corner of the plastic bath. Spill-over is induced by decreasing the angle of the sheet with the bath.

3.8 Experimental Design

A miniature proof-of-concept experiment is used to study and illustrate the mechanism of melt spill over in a HRG configuration when the pull angle is varied. A polyethylene ribbon ($\rho_{pe} = 0.93g/cm^3 < \rho_{water}$) rests completely on top of the water contained in a plastic bath such that the inclination with respect to the top surface of the water can be varied.

From Section 3.6.2, we observed a range of infeasible pull angles around the horizontal position ($\beta = 0$) when H was greater than 0.2. To test this hypothesis, we induce spill-over by slowly decreasing the angle of inclination with the water surface while photographing the changes in the shape of the water meniscus. Figure 3.14 displays a sequence of photographs showing the bulking of the meniscus as the pulling angle decreases. The top left-most photograph shows the shape of a meniscus in which the ribbon is inclined at a positive angle (a stable configuration). This configuration would make it least likely for the ribbon to freeze on top of the crucible edge. The right-most bottom photograph is the

shape of a meniscus prior to spilling over the crucible (an unstable configuration) as the ribbon becomes horizontal. Despite the difference in materials, we see that the stability analysis from our theory agree qualitatively with the experimental observations.

3.9 Conclusions

This chapter provides a parametric formulation and a solution to the generalized static stability problem for the meniscus in a ribbon growth process. Due to the geometric nature of the meniscus problem, we observe that the method of parametric representation is not only preferable but also one which furnishes a complete solution. Using Weierstrass' variational theory, we found analytic expressions describing the shape of the meniscus and compared it with the family of Euler's elastic curves. This similarity can be used to exchange concepts from elasticity theory in order to study stability and bifurcations of menisci shapes in liquids and vice versa.

The stability of the meniscus is evaluated using Legendre and Jacobi test conditions. A range of stable operating conditions are provided over the parameter space of melt height and pull angle. Two bifurcation points are observed which divide the solution space into two regions. The infeasibility zone between the two solution spaces, which include the horizontal position of the ribbon, didn't have a stable meniscus solution to support the ribbon. Growing a ribbon in this region leads to melt spilling over from the meniscus until the melt height decreases to the stable region. This argument is supported by doing a simple proof of concept experiment, in which the phenomena of spill-over is created using a polyethylene ribbon resting on a bath of water. Given the vast range of stable positive pull angles, we conclude that it is appropriate to incline the ribbon above a certain threshold angle to ensure stability of ribbon growth as the horizontal configuration was statically unstable.

Chapter 4

Weak Stefan Formulation for Bulk Crystal

Growth with Non-smooth Interfaces

Most heat transfer models for bulk crystal growth rely on the classical (strong) Stefan formulation to evaluate interface motion during phase change. However, when the interface is non-smooth the use of the classical Stefan formulation introduces singularities and ambiguity in direction and speed of crystallization. To address this problem, we propose to use a the weak formulation of the Stefan problem in problems with non-smooth interfaces. This approach, which has not been applied previously to this class of problems, provides an energy conserving discretization scheme that accurately evaluates heat transfer using a modified energy phase rule. We apply the weak Stefan formulation to numerically simulate the solidification of silicon in the horizontal ribbon growth process. Results using a finite volume approach show that the ribbon's pull speed is limited as observed in the experimental studies summarized Chapter 2. A comparison of heat transfer between radiation and gas cooling shows that gas cooling increases the pull speed limit for the same amount of heat removed.

4.1 Introduction

Heat transfer modeling and numerical simulation play important roles in the design and control of crystal growth processes [83]. At their core, crystal growth models describe phase transition taking place across a moving interface. The physics of phase transition are complex and depend on the scale of the process and the properties of the materials

involved. Still, a first order macroscopic model for phase transition can be developed, based on the basic principles of mass and energy conservation. Such models belong to a well known class of mathematical formulations known as Stefan problems [84].

Solving a Stefan problem in 2 or 3 dimensions is challenging since the shape of the interface is not known beforehand. Therefore, crystal growth models often rely on numerical techniques to obtain accurate solutions [85]. Methods based on Galerkin finite element combined with arbitrary Lagrangian-Eulerian (ALE) approaches have been used due to their high spatial accuracy [86, 87]. Helenbrook and Hrdina [88] developed an adaptive mesh algorithm to track the interface using a triangular, ALE moving mesh representation to tackle large, unsteady interfacial deformations. Finite volume methods using interface tracking algorithms are used in [89, 90] to build 3D models for the Czochralski process. Weinstein et al. [91] applied a Lattice Boltzmann model to track interface evolution while accounting for anisotropic interface attachment kinetics. Other approaches that track the interface evolution implicitly, such as the phase field models, are also used to model crystal growth [92]. However, they are best suited to model phase transition at the microscopic level based on thermodynamic considerations, such as dendrite growth and phase boundaries [93, 94].

Despite the ubiquity of Stefan problems in modeling crystal growth processes, certain problems exist. One major problem is the use of the strong formulation, also known as the classical formulation, of the Stefan problem to model non-smooth interfaces. An interface is termed non-smooth if the unit normal at any point on the interface is not uniquely defined. On a smooth interface the strong form of the Stefan condition based on energy conservation is given by

$$\left[k_l \nabla T_l - k_s \nabla T_s \right] \cdot \hat{n} = -\rho L \vec{v} \cdot \hat{n}, \quad (4.1)$$

where \hat{n} is a unit vector normal to the interface; k_s, k_l are the thermal conductivities and $\nabla T_s, \nabla T_l$ are the temperature gradients for the solid and liquid phase. ρ denotes the density of the solid phase, L is the latent heat of fusion and $\vec{v} \cdot \hat{n}$ denotes the velocity of the

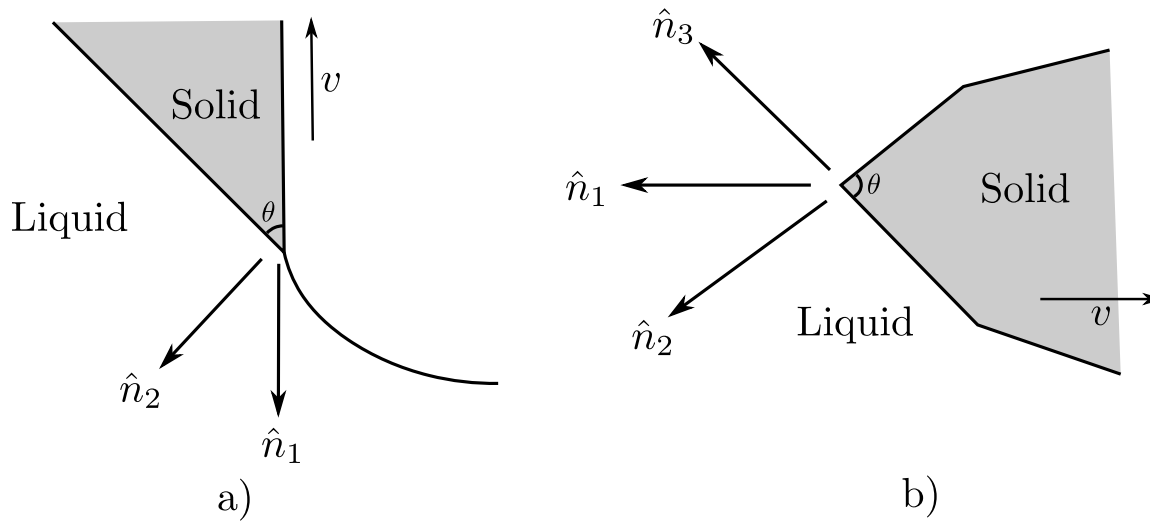


Figure 4.1: Examples of ill-defined interface velocity at non-smooth corners in bulk crystal growth

interface from solid to liquid. Equation (4.1) holds point-wise everywhere on the interface.

The assumption of smoothness (differentiability) of the interface puts a restriction on the applicability of the classical Stefan formulation. This is especially relevant for crystal growth systems since the non-smooth interfaces occur in many applications [95, 92, 96]. Figure 4.1 provides two examples of frequently encountered situations in crystal growth where the classical Stefan formulation is not applicable. Figure 4.1a is a close-up of a crystal growth configuration around a triple point. The solidification interface makes an angle θ with the free surface. In the case of a faceted growth, θ can be a fixed angle [97, 98, 99]. The unit normal is uniquely defined everywhere on the interface except at the triple point. At the triple point, the tip grows with a velocity of either v , if measured from the direction of \hat{n}_1 ; or $v \sin \theta$, if measured from \hat{n}_2 . This presents an ambiguity in the choice of the normal velocity in the Stefan condition (4.1). A similar problem exists in systems with facet growth [100, 101, 102], as shown in figure 4.1b, where the normal component of the interfacial velocity likewise cannot be uniquely defined and is characterized by a sub- rather than regular derivative. This gives an ambiguity in the strong formulation which

requires the imposition of additional conditions to determine physical properties of the system such as direction and speed of crystallization.

Using the classical Stefan formulation to model interfaces that are non-smooth can, therefore, lead to incorrect results [103, 104, 105]. This is because the limit of the energy balance equation on an arbitrarily small neighbourhood of a non-smooth interface does not exist. In the context of bulk crystal growth systems, the use of the classical formulation has created singularities around triple points and facet corners, which has made the analysis of heat transfer difficult.

In the Bridgman process, theoretical and numerical solutions have shown singularities in many applications at the intersection of crucible walls with the interface [106, 107]. This has led to the phenomenon of “Interface effect”, which makes it difficult to control the interface shape [108, 109]. Singularities have also been observed near the triple point in the Czochralski process [110, 111]. Asymptotic analysis shows that the order of these singularities depend on the angle prescribed by the triple point or the facet corners [112, 113]. As a result, the use of numerical techniques that rely on piecewise polynomials do not model heat transfer at such points accurately [114].

One particular crystal growth method where singularities have made it difficult to provide robust predictions is the horizontal ribbon growth (HRG) process [34, 115, 116]. Figure 4.2 provides a schematic of the growth zone in the horizontal ribbon growth furnace near the triple point. Cooling is applied at the top surface of a molten bath and a seed crystal is inserted horizontally to nucleate the growth process [117]. The thickness of the growing crystal is controlled by manipulating the cooling rate and the pull speed (v). A higher pull speed provides less exposure to cooling and thus produces thinner ribbons. However, experiments have shown that the HRG process exhibits a limitation on its pull speed, which also constraints the size of the ribbon’s thickness [118, 44]. Theoretical modeling and simulations have not provided any conclusive explanation for the pull speed limit [119, 120, 121, 122, 41, 123]. This has hindered the scale up of the process, since it has

not been possible to increase production speed to meet industrial standards [46].

The aim of this chapter is to develop a theoretical framework for simulating crystal growth based on the weak formulation of the Stefan problem. We apply this theory to the numerical simulation of the horizontal ribbon growth process. At the same time, we keep the formulation general enough to be applicable to other areas of crystal growth. Although fluid flow, meniscus stability and impurities play important roles in the stable operation of the horizontal ribbon growth process [124, 125, 126, 127], here we decouple these phenomena and focus only on the conductive heat transfer aspect of the process. In doing so, we provide quantitative estimates on the limitation on pull speed and ribbon sheet thickness as observed in experiments.

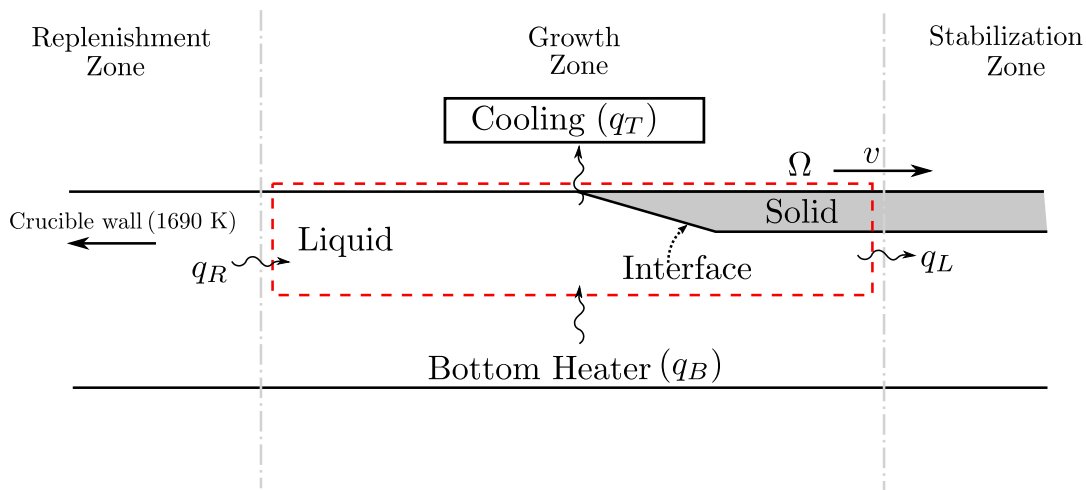


Figure 4.2: Schematic of the horizontal ribbon growth process around the growth zone

4.2 Mathematical Formulation

Consider a process of solidification taking place inside a closed domain Ω , belonging to a subset of the Euclidean space \mathbf{R}^n ($n = 2, 3$). We shall assume that the process occurs at constant volume, i.e., no volume change associated with phase change. In practise, the

volume change upon solidification for silicon is about 3.5%. The domain is occupied by a pure material capable of attaining two phases, liquid and solid, at a sharp melting point T_m . The analysis is carried out in a Lagrangian frame of reference, so that the solid material moving at a constant velocity v appears stationary.

The time interval for analysis is set to $]0, \tau[$, where τ is a constant. The domain of interest is therefore $Q := \Omega \times]0, \tau[$. An energy balance carried out over any volume V with surface area A gives

$$\int_{\Gamma} \left[\frac{\partial}{\partial t} \int_V U dV + \oint_A \vec{f} \cdot \hat{n} dA \right] dt = 0 \quad \forall V \times \Gamma \subseteq Q \quad (4.2)$$

where U is the density of internal energy within volume V and $\vec{f} \cdot \hat{n}$ is the flux of the energy transferred through the boundary A . The energy balance holds over any time interval $\Gamma \subseteq]0, \tau[$. The use of the integral form (4.2) is advantageous as it reduces the requirements on the regularity of the interface shape. Since we carry out our analysis in a Lagrangian reference frame, conduction is the only main source of energy transport within the material. Therefore, the energy flux at any point inside the domain is given by the Fourier law:

$$\vec{f} = -k \nabla T. \quad (4.3)$$

Additional information on the nature of U is needed for (4.2) to be suitable in practice. This will be given by an energy-phase rule that takes into account the possibility of metastable states. The phase rule we use for the weak formulation is a modification of the temperature-phase rule used for the strong formulation proposed in [84].

4.2.1 The Energy-Phase Rule

We define a solid fraction field, $\chi \in [0, 1]$, to denote the phase of the material at any point in Q . $\chi = 1$ corresponds to the material in the solid phase and $\chi = 0$ to the material in the liquid phase. An intermediate value of χ denotes a solid-liquid mixture at the macroscopic length scales. In the crystallization literature $\chi \in (0, 1)$ is referred to as a mushy zone. For our formulation, we require that the phase change only occurs at the melting point T_m ,

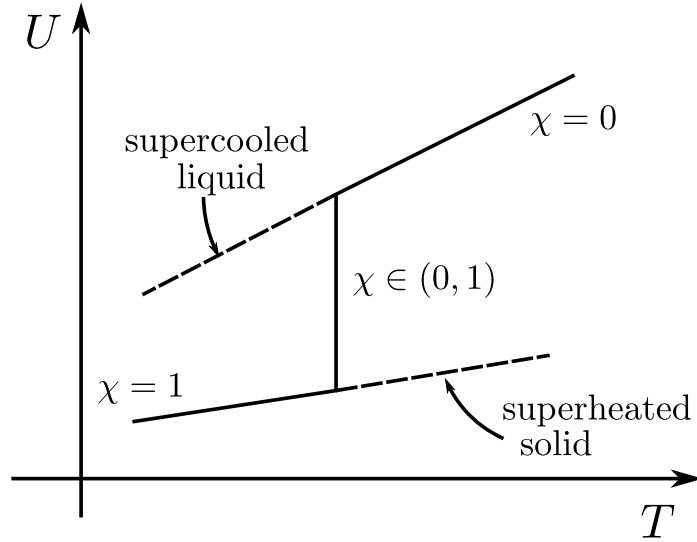


Figure 4.3: Energy-Phase rule

during which the temperature remains constant until χ changes phase to either 0 or 1. The formulation allows for the existence of supercooling in absence of nucleation during extreme cooling. These features are captured through the energy-phase rule of the form given below:

$$U = \begin{cases} \rho c_s(T - T_m) & \chi = 1 \\ \rho L \chi & \chi \in (0, 1), T = T_m \\ \rho L + \rho c_l(T - T_m) & \chi = 0. \end{cases} \quad (4.4)$$

Figure 4.3 illustrates the essential features of the energy-phase rule. The internal energy is considered to be a multi-valued function of the temperature that branches at two points. The choice of the branch depends on whether a phase change is initiated as the temperature approaches the melting point. The criteria for initiating a phase change is determined by a set of rules discussed in section 4.1. Metastable states, like a supercooled melt, are often observed in practise, this energy-phase rule (4.4) allows us to approximate the physics of crystal growth in a manner representative of experimental systems.

Substituting (4.4) in (4.2), the energy balance equation can be re-written as:

$$\int_{\Gamma} \left[\frac{\partial}{\partial t} \int_V (\rho c_{\chi}(T - T_m) + \rho L\chi) dV + \oint_A \vec{f} \cdot \hat{n} dA \right] dt = 0 \quad \forall V \times \Gamma \subseteq Q, \quad (4.5)$$

where c_{χ} is equal to c_s in the solid phase and equals to c_l in the liquid phase. V and A refer to the (Lebesgue) measure in 3 and 2D respectively.

4.3 Numerical Simulation Model

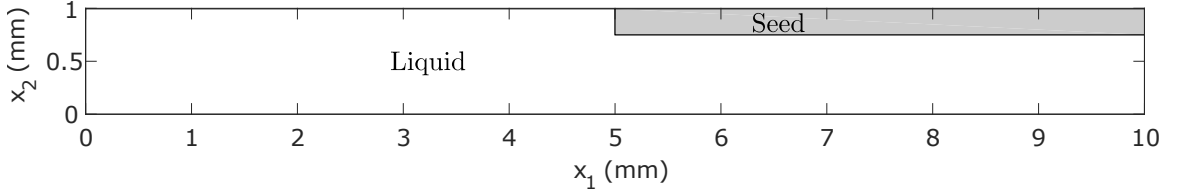


Figure 4.4: Simulation domain and initial seed configuration of the HRG process

To test the utility of the weak formulation, we carry out finite volume simulations to model the growth of a silicon ribbon in a horizontal ribbon growth process. The simulation is carried out in a rectangular domain of size $1\text{mm} \times 10\text{mm}$ around the growth tip of the ribbon. The shape and size of control volumes are chosen based on the geometry of the domain and the accuracy needed for the required engineering application. For our simulations, we divided the domain into rectangular control volumes (V_i) of size $\Delta x = 5\mu\text{m}$. The time interval for simulation will be divided into equal open intervals Γ_n of size Δt .

Each cell element $V_i \times \Gamma_n$ of Q is categorized to belong to one of the three domains: solid Q_s , liquid Q_l or interface Q_I . Phase change will be restricted to take place only in the interface domain Q_I . In the solid Q_s or liquid Q_l domain, no phase change occurs so the energy balance equation (4.5) reads

$$\int_{\Gamma_n} \left[\rho c_j \frac{\partial \bar{T}_i}{\partial t} \Delta x - D f_i \right] dt = 0 \quad \forall V_i \times \Gamma_n \subseteq Q_j, \quad j = \{s, l\}, \quad (4.6)$$

where \overline{T}_i is the temperature field averaged over the control volume V_i . D is the difference operator and $Df_i = f_R - f_L + f_T - f_B$ denotes the intensity of the heat flux removed from the control volume V_i . f_R, f_L, f_T and f_B represent the heat fluxes from the right, left, top and bottom walls of V_i respectively.

The interface is characterized as a region of phase change with constant melting point T_m . Therefore, the energy balance equation (4.5) in the interface domain (Q_I) is written as

$$\int_{\Gamma_n} \left[\rho L \frac{\partial \overline{\chi}_i}{\partial t} \Delta x - Df_i \right] dt = 0 \quad \forall \quad V_i \times \Gamma_n \subseteq Q_I \quad (4.7)$$

where $\overline{\chi}_i$ is the solid fraction averaged over the control volume V_i . Equation (4.7) equates the intensity of latent heat released due to phase change to the intensity of heat removed from a control volume of size Δx .

Equations (4.6) and (4.7) are conservative discretizations of the balance equation (4.5), in the sense that the flux on the boundary of one cell equals the flux on the boundary of the adjacent cell. Since conservation holds at the discrete level; if the numerical method converges, they can be proven to converge to a weak solution of the conservation law (4.5) using the Lax-Wendroff theorem [128].

In a Stefan problem, the solid-liquid interface behaves like a moving boundary that evolves continuously over time. Due to this, the proposed simulation scheme proposed relies on the categorization of each cell element at the beginning of every time step. Therefore, a capture rule is required to determine the propagation of the interface for numerical simulations.

4.3.1 Interface Propagation

In the classical Stefan formulation, phase transition occurs only at the interface, between the boundaries of the solid and liquid phases. This condition serves as a useful abstraction to model solidification processes involving metastable states, namely, supercooling and superheating. In contrast, the enthalpy based methods for solidification assume thermodynamic equilibrium at all points in the domain.

Keeping this in mind, we constrain local thermodynamic equilibrium to occur only along a small band of size Δx between the solid and the liquid phase. Physically, this would signify the proximity of the liquid to nucleation sites for phase transition. This region of size Δx is defined as the interface. Away from the interface, we allow for the possibility of metastable states. All of this is governed by the energy phase rule described in (4.4).

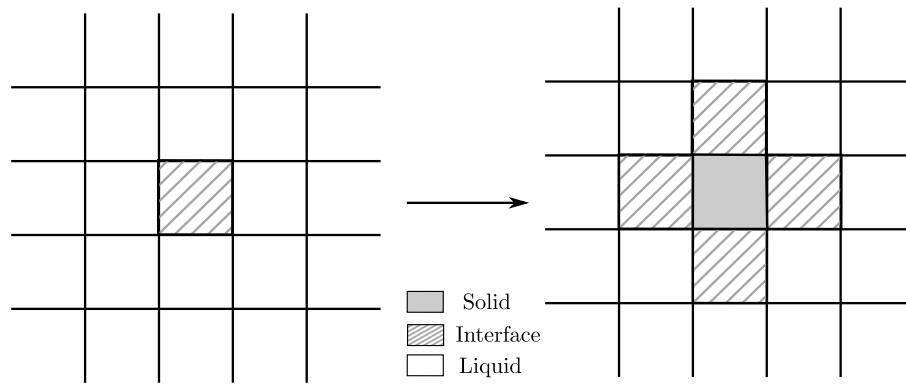


Figure 4.5: Interface propagation rule for solidification.

Initially, each cell in $\Omega \times \{0\}$ is categorized as either a solid, liquid or interface. At the end of each time interval, an interface propagation step is carried out. In this step, any cell belonging to the interface that exceeds its solid fraction beyond $[0, 1]$ changes its label to either liquid or solid appropriately. This transformed cell acts as a nucleation site for its nearby cells to become a part of the interface. Figure 4.5 shows an example of a Δx radial neighbourhood, also called the Von Neumann neighbourhood, used for interface propagation. In general, crystals have anisotropic surface energy, so the interface propagation may be preferred along certain directions. However, in the simulation we consider the case when the crystal growth is isotropic.

The interface propagation step is carried out at the end points of the discretization scheme. Due to this, additional steps need to be taken to ensure that energy is conserved

when the labels on the cells are changed. When a cell transforms from a solid or liquid phase to an interface, the temperature of the cell is updated to T_m and the residual thermal energy is transferred into the solid fraction using

$$L \Delta \bar{\chi}_i = c_\chi (T_m - \bar{T}_i), \quad (4.8)$$

where $\Delta \bar{\chi}_i$ is the change in the solid fraction of cell i . A similar strategy is applied when the solid fraction of an interface cell exceeds $[0, 1]$ and changes to either a solid or a liquid cell.

4.3.2 Numerical Method

Applying the equation for heat flux (4.3) to each wall in the control volume V_i , the flux can be discretized using the central difference scheme, which is substituted into equations (4.6) and (4.7). Combined with the boundary conditions, the system of equations describing the evolution of the temperature and phase fields is complete and can be solved using any standard method of numerical integration. For this paper, we found the Douglas-Gunn Alternating Direction Implicit (ADI) scheme to be stable and efficient in solving the integral equations. The implementation of the ADI scheme is standard and we refer the readers to McDonough [129] for more information.

Due to the Lagrangian nature of the simulation, the domain needs to be re-centered after a fixed number of iterations to prevent the domain from leaving the area of interest. To do this effectively, we re-center the simulation domain after every $\Delta x/v\Delta t$ iterations. This approach restricts the choice of v so that $\Delta x/v\Delta t$ is an integer. The simulation is said to reach steady-state when the solution becomes time independent within given tolerance.

At the initial stages of the simulation, the numerical integration starts with large step sizes, $\Delta t \approx 10\Delta x$. The step size is then gradually decreases to $\Delta t = \Delta x$, until steady state is reached. In some situations, it was observed that the interface would oscillate for a large number of iterations and would not reach steady state. This was attributed to the explicit nature of the interface propagation step. The conversion of residual solid fraction

into thermal energy based on (4.8) could sometimes cause the algorithm to not converge due to the large value of latent heat L . In this case, further decrease in the step size of the simulation or distribution of the excess solid fraction to the nearby transformed cells was found to be sufficient to stop the oscillations.

4.4 Application: Horizontal Ribbon Growth

To determine the boundary conditions required for our simulations, we refer to Figure 4.2 for a cross-sectional schematic of the horizontal ribbon growth furnace. A cooling mechanism at the top surface of the melt drives the solidification process which causes single crystal silicon to grow. Cooling takes place either through a passive mechanism, such as radiation or through an active cooling system, such as cold gas injection on the surface. [118, 130, 39, 115].

For the case of radiation, the top surface heat loss is given by the Stefan-Boltzmann law

$$q_t(x_1) = \epsilon\sigma(T^4 - T_c^4)F(x_1), \quad (4.9)$$

where σ is the Stefan-Boltzmann constant, $\epsilon = \chi\epsilon_s + (1 - \chi)\epsilon_l$ is the weighted emmissivity of solid (ϵ_s) and liquid (ϵ_l) emmissivities. $T_c = 300\text{K}$ is the temperature of the water cooled walls of the furnace surrounding the crucible. $F(x_1)$ is called the view-factor and takes into account the area exposed by an opening, like a slit, to the water cooled walls of the furnace from any point x_1 on the surface of the melt. We consider the slit width to be variable and placed above the top surface of the melt at a height h . The width of the slit is parameterized using the variable w . The view-factor at any point x_1 on the surface of the melt is given by the formula [131]:

$$F(x) = \frac{\sin \phi_2 - \sin \phi_1}{2}, \quad (4.10)$$

where $\sin \phi_1$ and $\sin \phi_2$ are

$$\sin \phi_1 = \frac{-(w+x)}{\sqrt{(w+x)^2 + h^2}} \quad \sin \phi_2 = \frac{(w-x)}{\sqrt{(w-x)^2 + h^2}}. \quad (4.11)$$

For the base case, a value of $w = 5\text{mm}$ is chosen. A small value of h , say $h = 0.1\text{mm}$, allows a smooth transition in the radiative heat flux near the slit edges. The variable w will be used as a parameter to study the effects of radiation length on pull speed.

To model the gas cooling jet, a scaled down version of the experimental conditions in Helenbrook et al. [123] will be used. For gas cooling (hereon referred as Gaussian cooling), the top surface heat removal rate is modeled using a Gaussian curve, parameterized by peak intensity q_{peak} and spread σ .

$$q_t(x) = q_{peak} \exp\left(\frac{-x^2}{2\sigma^2}\right). \quad (4.12)$$

An approximate fit to the experimental data in Helenbrook et al. [123] was found at $\sigma = 0.8$. q_{peak} was chosen to be 40 W/cm^2 , to ensure the heat removed using the Gaussian cooling profile was of the same order of magnitude as the heat removed using radiation. These values of σ and q_{peak} will serve as the base case for Gaussian cooling and provide us with a comparative study of the two cooling mechanisms.

A positive thermal gradient in the melt is found to provide a stable environment for crystal growth [100]. For this reason, a small heat flux is applied on the bottom boundary of the domain, supplied from the heaters on the underside of the crucible.

$$q_B = 2\text{ W/cm}^2 \quad (4.13)$$

In a reference frame moving at a constant velocity v , the top and bottom boundary conditions appear to drift in the opposite direction. To account for this, we introduce a time dependent drift on the top boundary condition.

$$q_T(x_1, t) = q_t(x_1 - vt).$$

Since the bottom flux is a constant, it remains unchanged.

Preceding the growth zone is a replenishment zone that provides a constant supply of melt. This is done by means of heaters inside the crucible walls that melt silicon feed chunks. Experimental conditions maintain the temperature of the silicon melt at 1690K [123].

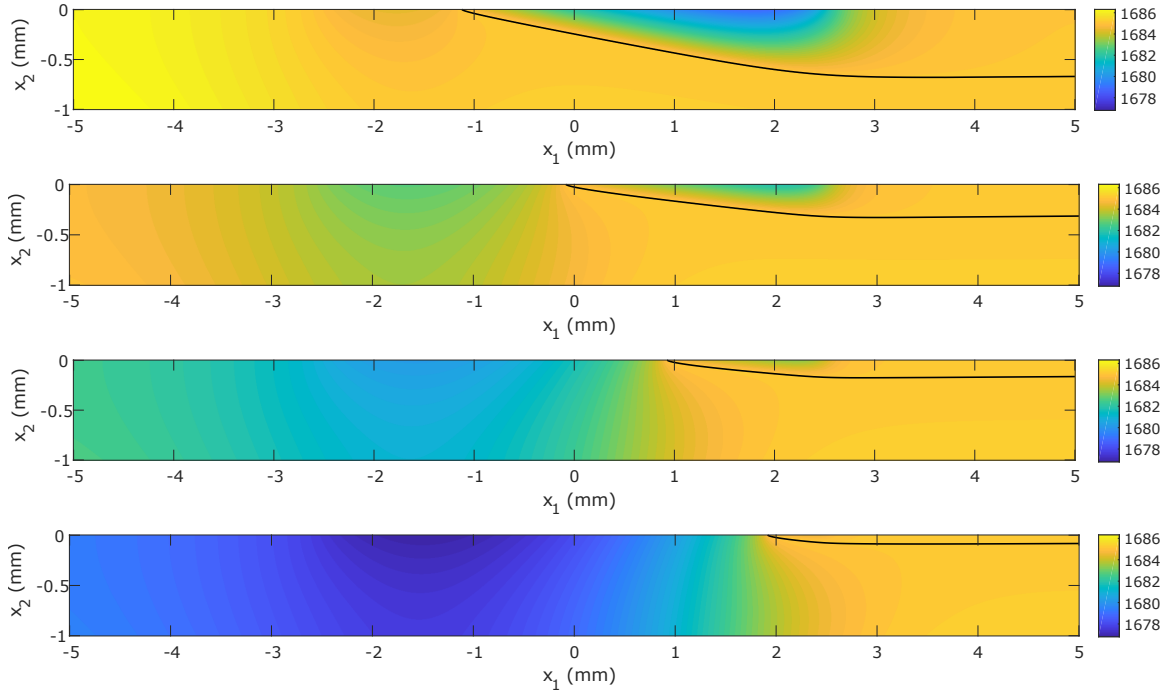


Figure 4.6: Temperature maps for radiation cooling at ribbon pull speeds of 0.3, 0.5, 0.7, 0.9 mm/sec from top to bottom, respectively. The solid black line describes the position of the solid-liquid interface.

This bulk melt at 1690K is assumed to be 5cm away from the simulation domain. We also assume a linear temperature profile inside the replenishment zone with respect to the moving reference frame. The left boundary condition is therefore calculated to be

$$q_L = -k_l \frac{\Delta T}{\Delta x} = \frac{67 \times 10^{-4}}{5 \times 10^{-2}} (1690 - T) = 0.134 \times (1690 - T) \text{ W/cm}^2 \quad (4.14)$$

As the ribbon is pulled out of the simulation domain, it exits into a stabilization zone. In this region, the temperature in the solid and liquid phases are maintained so that conduction only occurs in the vertical direction [123]. Although convective heat transport still exists in the horizontal direction, in a moving reference frame this effect is not realized and therefore the heat flux at the right boundary equals zero, i.e.

$$q_R = 0. \quad (4.15)$$

Parameter	Symbol	Value
Density of liquid silicon	ρ	2530 [kg/m ³]
Thermal conductivity of silicon melt	k_l	67 [W/mK]
Thermal conductivity of silicon solid	k_s	22 [W/mK]
Heat capacity of silicon melt	c_l	1000 [J/kgK]
Heat capacity of silicon solid	c_s	1060 [J/kgK]
Latent heat of fusion	L	1.8×10^6 [J/kg]
Emmisivity of silicon melt	ϵ_l	0.2
Emmisivity of silicon solid	ϵ_s	0.6

Table 4.1: Material properties of silicon used for simulation

The initial condition for simulations was found to be robust to any appropriate choice of seed crystal shape and temperature field. The first simulation was initialized using a rectangular seed crystal of width $250\mu\text{m}$ and length 5mm, covering the top half surface of the melt as shown in figure 4.4. The melt was initialized with a uniform temperature of 1690K and the solid was chosen to be at a 1680K . Subsequent simulation for different operating condition were initialized from the steady state solution of the previous simulation.

4.4.1 Results

We begin the simulation study by applying the finite volume discretization to the base cases of radiation and Gaussian cooling. The values of the physical constants required for simulation are summarized in Table 1.

We first consider the base case when the top surface of the melt is cooled by radiation. For this case, the slit only allows the center 5 mm of the melt to radiate heat, which acts as the sole mechanism of latent heat removal. We perform simulations at pull speed in-

crements of 0.05 mm/sec, starting from 0.3 mm/sec. Figure 4.6 illustrates the steady-state temperature fields at pull speeds of $v = 0.3, 0.5, 0.7$ and 0.9 mm/sec. The solid black line in the figures denotes the shape of the ribbon. For all pull speeds, the ribbon shape is found to approximate a wedge shape. This can be attributed to the near constant heat flux at the top surface of the solid [119]. Figure 4.7 illustrates the top surface heat flux for radiation and Gaussian cooling. The radiative heat flux was plotted at a steady-state pull speed of $v = 0.5$ mm/sec. The heat flux appears constant in solid and liquid phases and shows a jump in between due to their difference in emissivities.

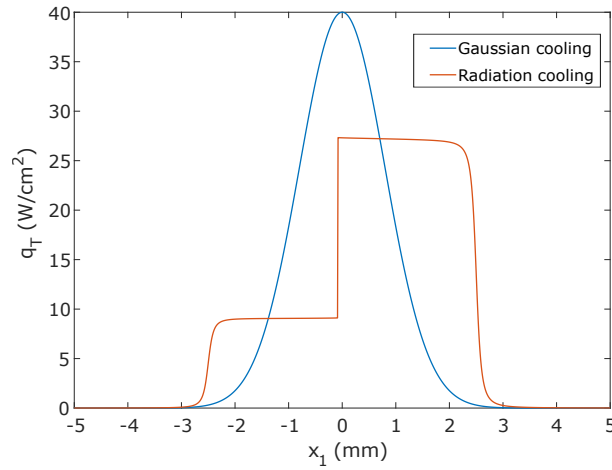


Figure 4.7: Comparison of top surface heat flux for radiation ($v = 0.5$ mm/sec) and Gaussian cooling

For the base case involving Gaussian cooling, simulations performed at 0.1 mm/sec increments, starting from a pull speed of 0.2 mm/sec. Unlike the radiation case, the heat removed by Gaussian cooling does not depend on the position of the ribbon tip. The temperature field and ribbon shape at pull speeds of $v = 0.2, 0.4, 0.8$ and 1.6 mm/sec are displayed in Figure 4.8. In this case, the ribbon shape is curved due to the non-linear shape of the Gaussian cooling profile.

Comparing figures 4.6 and 4.8, we observe certain similarities and differences between

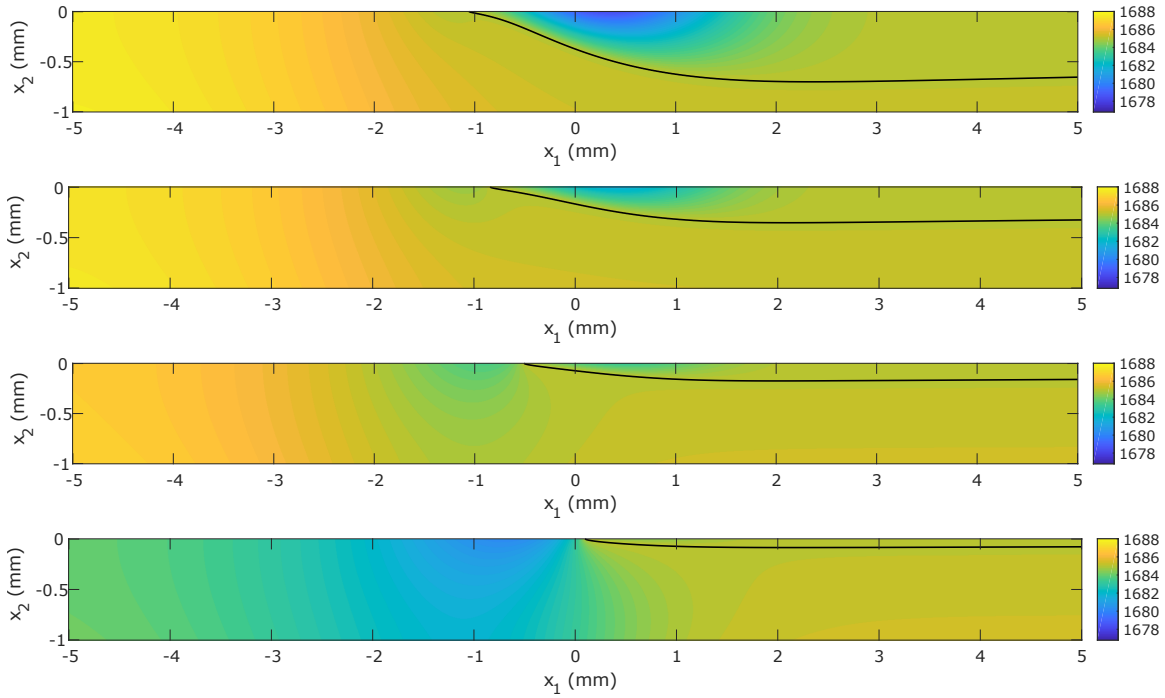


Figure 4.8: Temperature maps for gas cooling at ribbon pull speeds of 0.2, 0.4, 0.8, 1.6 mm/sec from top to bottom, respectively.

the two cooling mechanisms. In both cases, we observe the ribbon tip moving to the right as the pull speed increases. This creates a U-shaped pool of supercooled melt in front of the ribbon tip that grows larger in size. It is worthwhile to note the larger pool size in radiation compared to Gaussian cooling. Another important observation is the motion of the ribbon tip to the center in the Gaussian case, and to the edge of the slit in the radiation case.

The information on the pull speed and ribbon thickness for radiation and Gaussian cooling is summarized as a graph in figure 4.9. This relationship is governed by the total energy balance equation

$$L\rho vt_r = Q_{tot}, \quad (4.16)$$

where t_r is the thickness of the ribbon and Q_{tot} is the total heat removed from the domain.

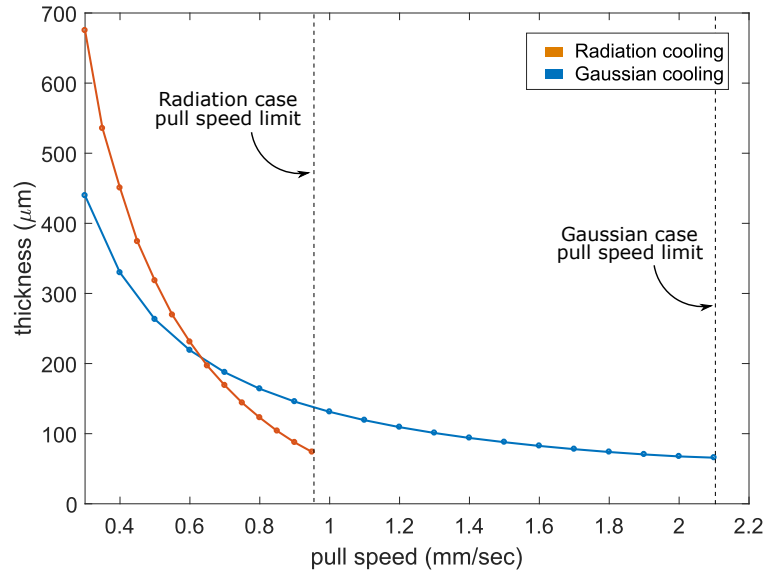


Figure 4.9: Thickness vs pull speed plot for radiation and Gaussian cooling. The dashed lines signify the pull speed limitation observed in simulations.

The two curves intersect at a pull speed of $v = 0.63$ mm/sec. Therefore, the point where the two curves intersect denotes equal heat removal Q_{tot} for the two cases. Below this pull speed the heat removed from the radiative case is higher and above this pull speed the heat removed is lower due to the difference in emissivities of the two phases. This causes radiation to produce thicker ribbons at lower pull speeds and thinner ribbons at higher pull speeds.

In Addition, we also observe a pull speed limitation for both mechanisms. For radiation, the limit occurs at 0.9 mm/sec as the ribbon tip reaches the end of the slit. On the other hand, the pull speed limit for Gaussian cooling occurs at 2mm/sec, as the ribbon tip reaches the center of the cooling jet.

4.4.2 Discussion

The previous section, showed limitations in ribbon's pull speed for radiation and Gaussian cooling. To study this further, we take a closer look at the temperature profile near the

ribbon tip. Figure 4.10 shows a close-up of the temperature contours near the ribbon tip for the two base cases at their respective pull speed limit. The isotherms are vertical as they approach the ribbon tip. This implies a predominantly horizontal mode of heat removal at the ribbon tip. This is in contrast to the conventional notion of heat removal in the horizontal ribbon growth process, which was considered to be in the vertical direction.

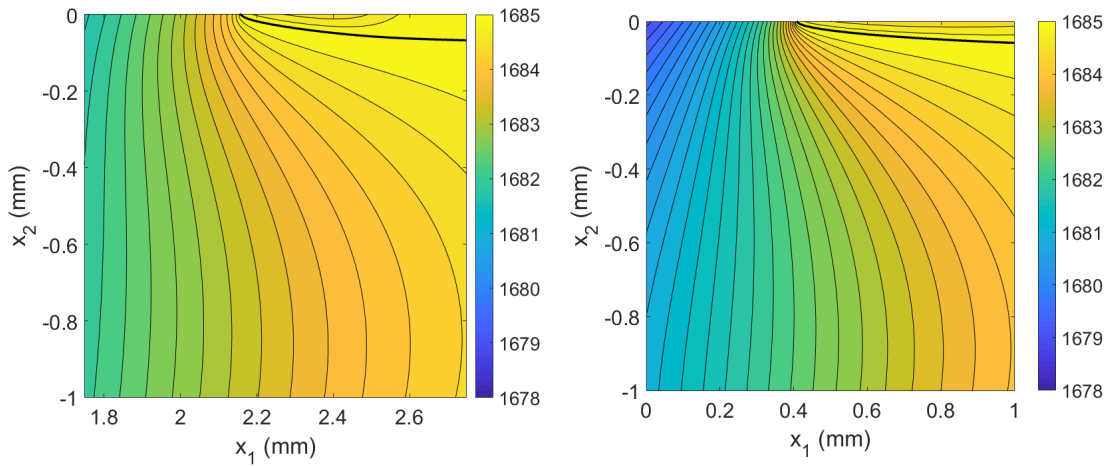


Figure 4.10: A close up of the temperature field around the ribbon tip for radiation (left) and Gaussian cooling at limiting pull speeds of 0.9 and 2 mm/sec respectively. The thick black line denotes the interface at $T_m = 1685\text{K}$. Thin black lines denote isotherms at 0.2K intervals.

To explain this hypothesis, we study the variations in the temperature gradient around the ribbon tip for increasing pull speeds. Figure 4.11 plots the temperature profile at the top surface of the domain, $T(x_1, 0)$ for the two base cases. The multiple curves in each plot, from left to right, denote the temperature profile for increasing pull speeds. The position of the ribbon tip in these curves can be identified by the peak at $T_m = 1685\text{K}$. At low pull speeds, almost all the heat removal required to maintain solidification at the ribbon tip is from the solid side. As the pull speed is increased, the ribbon tip shifts to

the right. This decreases the heat removed from the solid surface and increases the heat removed from the liquid surface. The increase in the heat removed from the liquid side creates a pool of super-cooled melt in front of the ribbon tip. The negative thermal gradient in the melt provides the necessary source of heat removal to maintain growth at the tip. Moreover, the decrease in the heat removed from the solid side causes the ribbon to get thinner. Therefore, from the perspective of heat transfer, it is more efficient to remove heat from the liquid side than the solid side because some portion of the heat removed from the solid side is used to maintain the ribbon's thickness.

Based on the above explanation we summarize the observation of pull speed limit as follows: increasing the pull speed of the ribbon requires an equal increase in the growth rate of solid at the ribbon tip. If sufficient latent heat is not removed to maintain this growth rate, the ribbon tip moves to the right. This increases the amount of heat removed from the tip—by increasing the heat removed from the liquid side—and establishes a new equilibrium position. As the pull speed is increased further, at some point the heat removed from tip is at its maximum and the growth rate reaches its limits. For the Gaussian case this limit occurs around the center of the cooling profile, while for the radiation case this limit occurs at the edge of the slit.

4.4.3 Comparison Between Radiation and Gas Cooling

Simulations from the previous section suggest the pull speed limit for Gaussian cooling to be higher than radiation. However, since the heat removed due to radiation varies with pull speed, it is unclear if the advantage lies in the mode of cooling or the quantity of heat removed. Figure 4.12 plots the total amount of heat removed Q_{tot} , which includes the sum of conductive and convective heat transport from all four boundaries, at different pull speeds for the two base cases. The heat removed for Gaussian cooling is nearly constant while the heat removed during radiation cooling decreases with increasing pull speed. At the limit point, the heat removed in the radiation case is significantly lower than the

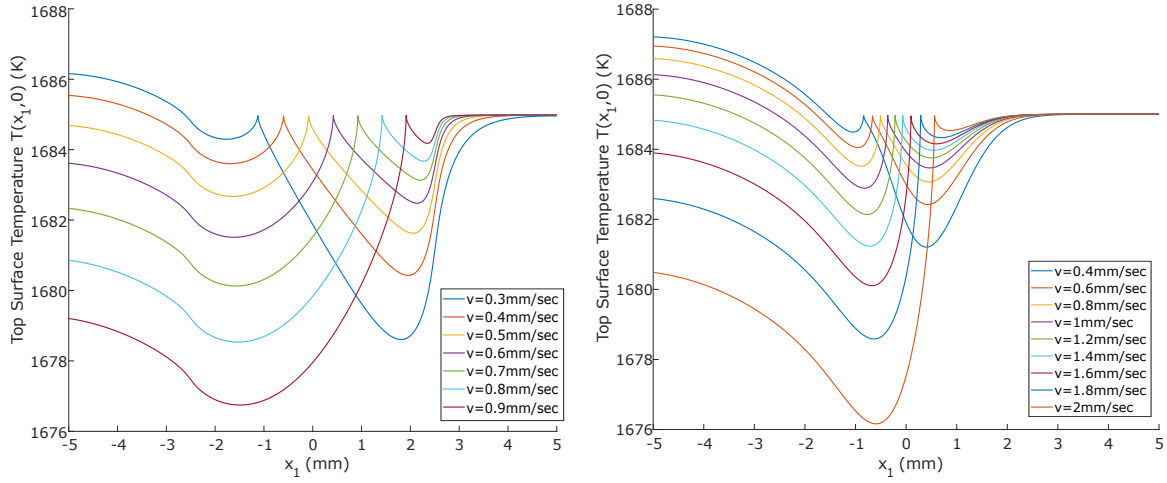


Figure 4.11: Top surface temperature profile for radiation (left) and Gaussian (right) cooling.

Gaussian case. Therefore, for a fair comparison it is reasonable to ask how radiation and Gaussian cooling compare for the same amount of heat removed.

To do this, a parametric study of the top surface cooling profiles is performed by varying the slit width w in radiation cooling and q_{peak} in Gaussian cooling. For the radiation case, 5 sets of simulations are performed with slit widths of $w = 2.5$ mm, 3.75 mm, 5 mm, 6.25 mm, and 7.5 mm. For Gaussian cooling, we choose $q_{peak} = 12.48$ W/cm², 18.19 W/cm², 23.96 W/cm², 28.94 W/cm², and 33.91 W/cm². These values of q_{peak} were chosen to match the total top surface heat removed from the radiation case.

Similar to the process of finding the limit points in figure 4.12, we find the pull speed limit v_{lim} in each case and mark them in figure 4.13. Interestingly, the points follow a straight line with R^2 value close to 1 upto 3 decimal places.

For both mechanisms, increasing the total heat removed from the system (Q_{tot}), leads to a proportional increase in the pull speed limit. For a given (Q_{tot}), Gaussian cooling achieved a higher maximum pull speed compared to radiation cooling. This can be attributed to the narrow heat removal profile in Gaussian cooling. Therefore, we find that

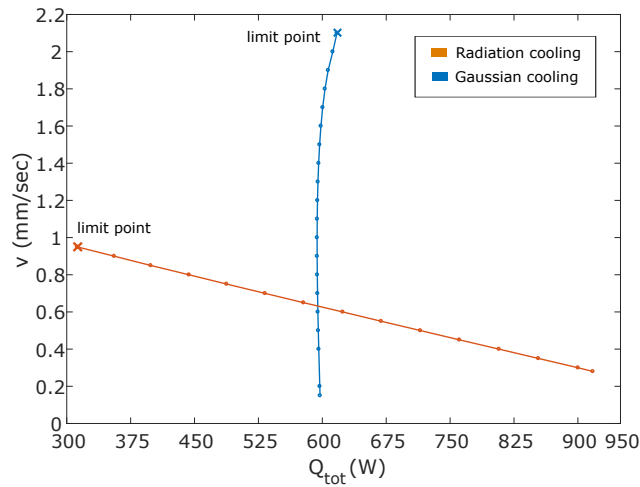


Figure 4.12: A graph highlighting the variability in total heat removed using radiation as a function of pull speed. In contrast, the heat removed using cooling jet is almost constant.

a cooling jet provides better performance in producing high speed ribbons than radiation. The improvement is larger at higher heat removal rates.

4.5 Active Cooling Design for Horizontal Ribbon Growth

Difficulty in producing thin ribbons at high production speeds has been a significant barrier in the adoption of the horizontal ribbon growth process for manufacturing low-cost silicon wafers. The use of active cooling devices, like helium jets, has allowed for intense heat removal from the ribbon tip leading to higher pull speeds. However, at the same time, this has also caused an increase in the thickness of the ribbon, making them unsuitable for commercial applications. We analyze the results from a series of simulation studies and outline a general process to the effects of active cooling on the ribbons' growth rate and thickness. A linear scaling relationship between the limiting pull speed and the total heat removed is derived empirically for a family of Gaussian cooling profiles. These scaling relationships show that the intensity and spread of a cooling profile are directly tied to the

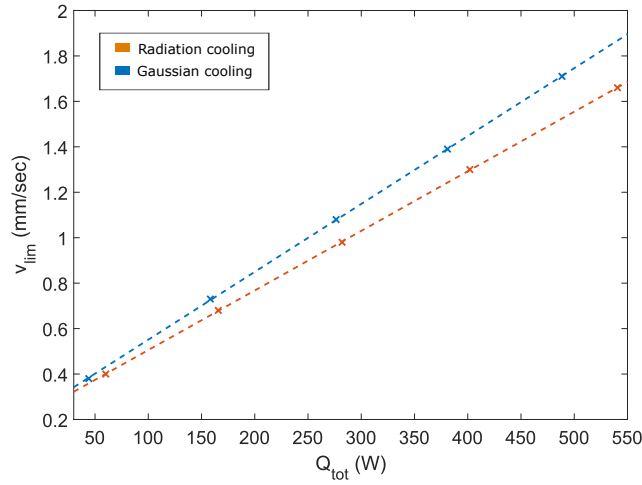


Figure 4.13: A graph of maximum pull speed as a function of heat removed. The dashed lines denotes the best fit lines.

growth rate limit and the ribbon's thickness, respectively.

We outline a general procedure to compare the performance of a cooling system design. We do this by solving the inverse problem of finding the limiting pull speed (v_{lim}) for a given cooling profile. For this, we begin with 3 scenarios for standard deviation, $\sigma = 0.8, 0.5$ and 0.2 . For each scenario, 5 instances of simulation are performed with different values of q_{peak} . Table 4.2 provides the numerical values for each instance. The values were chosen such that the total heat flux at the top surface in each column is the same.

The pull speed limit v_{lim} in each case was found and marked as a cross in figure 4.14. We observe that for each scenario, the points naturally classify themselves into straight lines. The best fit line for each case was determined using the form

$$v_{lim} = \alpha(Q_{tot} + Q_c), \quad (4.17)$$

where α and Q_c are the regression parameters of the best fit line. The numerical values of α and Q_c for each scenario of Gaussian cooling are summarized in table 4.3. The R^2 value for each scenario was equal to 1 within 3 decimal places.

Table 4.2: Numerical values for simulation instances

Spread, σ [mm]	Peak Intensity, q_{peak} [W/cm ²]				
	0.2	49.90	72.75	95.85	115.75
0.5	19.96	29.10	38.34	46.30	54.26
0.8	12.475	18.19	23.96	28.94	33.91

The scale factor α in (4.17) denotes the change in the pull speed limit due to a unit change in the amount of heat removed from the system. Q_c takes into account the non-linear behaviour of the process as Q_{tot} approaches to 0. The linearity of (4.17) was not found to be applicable for values Q_{tot} an order of magnitude lower than Q_c . Separate simulations were performed with larger values of heat supplied from the bottom heater, under the presumption that decreasing Q_{tot} would lead to thinner ribbons. However, increasing the heat supplied below the ribbon lead to insufficient heat removal at the growth tip. Additionally, the solution was found to be very sensitive to the initial position of the growth tip and the temperature field. Further analysis of this system was found to be difficult and therefore not reported here.

For each scenario in figure 4.14, we observe that increasing the total heat removed from the system (Q_{tot}), leads to an increase in the pull speed limit. For a given (Q_{tot}), the cooling mechanism with a narrower cooling profile yielded a higher pull speed limit. This is because a narrow cooling profile induces larger temperature gradients around the tip of the ribbon. This makes it possible to maintain a larger growth rate of the ribbon tip for the same amount of heat removed from the system.

The advantage of using a narrow cooling profile goes beyond increasing the pull speed limit of the ribbon. By substituting (4.17) into the overall energy balance, $L\rho vt = Q_{tot}$, we

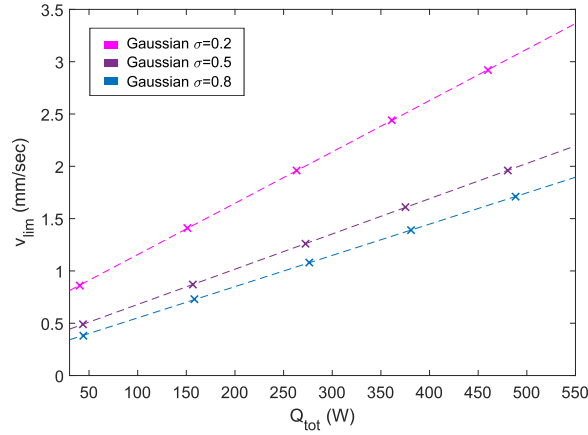


Figure 4.14: Scaling relationship between maximum pull speed limit and total heat removed for different Gaussian cooling profiles.

Table 4.3: Best fit parameters

σ [mm]	α [$\mu\text{m}/\text{J}$]	Q_c [W]
0.2	4.91	135.78
0.5	3.37	101.59
0.8	2.99	84.46

arrive at the equation

$$t_{lim} = \frac{Q_{tot}}{Q_{tot} + Q_c} \frac{1}{L\rho\alpha}, \quad (4.18)$$

where t_{lim} is the minimum thickness limit of the ribbon that can be produced for a given cooling scenario. L is the latent heat of fusion, ρ is the density of solid, t is thickness. Equation (4.18) shows that it is possible to produce thinner ribbons from the same amount heat removed Q_{tot} , if we choose a cooling system with a higher value of α . Figure 4.15 plots the limiting thickness of the ribbons produced for each scenario. Often, the ribbon interface would show dendritic behaviour near the limit point and so the thickness calculations had to be averaged.

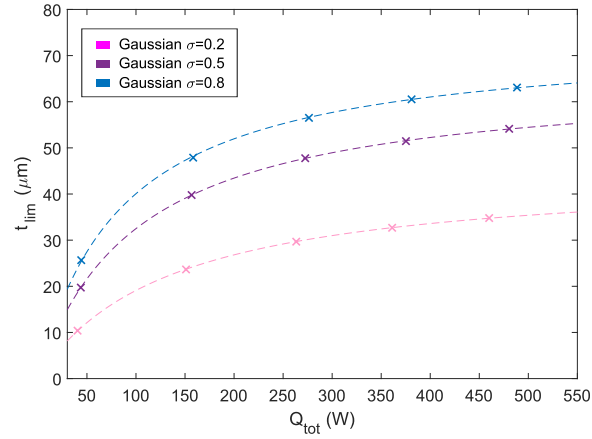


Figure 4.15: Minimum thickness as a function of total heat removed for different Gaussian cooling profiles

The dashed lines in figure 4.15 represent the curves generated from (4.18) for different modes of cooling. We observe that the curves flatten out at larger values of cooling provided to the system. This is apparent from (4.18), when $Q_{tot} \gg Q_c$

$$t_{lim} \sim \frac{1}{L\rho\alpha}. \quad (4.19)$$

Equation (4.19) explains why it has been difficult to reduce the thickness of ribbons in the presence of intense heat removal devices like cooling jets. In the high speed operation of the horizontal ribbon growth process, the minimum thickness limit of the ribbons produced is directly tied to spread of the cooling profile used to solidify the ribbon. Using a narrow cooling profile focuses the heat removal at the growth tip. This prevents any portion of the cooling jet from thickening the ribbon. Therefore a cooling jet with a higher value of α allows for the high speed production of thin ribbons.

4.6 Conclusions

The main goal of this paper is to provide an alternative theoretical framework for simulating crystal growth models involving non-smooth edges. We find that around non-smooth

interfaces, like the triple point in a horizontally grown ribbon, the classical models do not satisfy energy conservation. Therefore, a weak formulation of the Stefan problem is needed to relax the requirements on the regularity of the interface. A modified energy-phase rule is derived to account for the existence of metastable states. We choose a finite-volume discretization scheme to maintain the conservative form of the weak formulation. This allows us to come up with an easy to implement simulation scheme, which satisfies energy conservation and provides sufficient accuracy for engineering applications.

As an application, we perform a simulation study of the horizontal ribbon growth process. Unlike the classical Stefan formulations, the weak formulation demonstrates a pull speed limitation as observed in experiments. We explain the pull speed limit based on a local heat transfer arguments. During experiments, this limitation may be compounded by other physical constraints like the formation of a stable meniscus or solidification kinetics [122, 123]. However, from the perspective of heat transfer alone, insufficient heat removal from the growth tip is shown to be the fundamental reason for pull speed limitation.

Two different mechanisms of heat removal are analyzed. We find that a diffuse cooling profile, like radiation, is less effective than a narrow cooling profile, like a cooling jet, in producing thin ribbons at high speed. A linear relationship was discovered between the total heat removed from the furnace and the maximum pull speed in both cooling mechanisms. This relationship provides an interesting insight into the heat transfer occurring in the horizontal ribbon growth furnace and would require further analysis beyond the scope of this simulation. All of this aids in our understanding of the heat transfer conditions required for the high speed operation of the horizontal ribbon growth process.

We also discuss an approach in the design of active cooling system. Multiple simulations were carried out for varying peak intensities and spread of the Gaussian cooling profile. Through these simulations, a linear scaling relationship was discovered between the pull speed limit and the total heat removal rate. These scaling relationships serve as a lookup chart and may reduced the requirement to carry out expensive simulations. The spread

of the cooling profile was found to be directly related to the ribbons thickness. Therefore, we find in order to produce thin ribbons at high pull speeds, a narrow cooling profile with high intensity should be used.

Chapter 5

A theory on interface propagation at the solidification triple junction

In this chapter we are interested in identifying the physics of solidification at the solid-liquid-gas triple point. Importantly, we would like to know the limitations of using continuum models in describing the horizontal ribbon growth process. Since the problem is not limited to horizontal ribbon growth alone and may have a big overlap with other areas of multiphase physics, it will be of interest in knowing more about the generality of this problem and the mathematical tools used to solve them. An example of this is the paper by Amy Novick Cohen [132] where the triple junction motion of Allen-Cahn and Cahn-Hilliard type equations are studied using asymptotic analysis. The motion of the triple junction for solidification has also been studied experimentally by Surek and Chalmers [133] and using simulations by Virozub et. al [134]. However, there is no consensus between experimental, simulation, and theoretical values of the triple point angle, and existing works often contradict each other.

Our analysis shows that energy conservation at the triple point requires the solid angle to be 90° when the length scale is very small. At larger length scales, the result for the 90° solid angle still holds, but its effect decreases with increasing length scales as more physics may come into play. Experimental observations for horizontally grown silicon crystals show the solid angle to be 55° .

Combining the solid angle result with mass conservation adds another constraint of 90° for the liquid angle. However, these two results again do not satisfy the surface tension force balance at the triple point and are also not in line with experimental observations

for a liquid growth angle of 11° . We show that it is possible to accommodate all these experimental and theoretical observations using a multiple-scale model.

5.1 Introduction

The motion of the triple junction plays an important role in solidification processes. Examples of this include casting [135], sintering [136], welding [137], coating/painting [138], and crystal growth [112, 115]. A typical solidification process near the triple junction involves three phases. The interface separating the solid and the liquid phase interests the third phase, which could either be a free boundary formed by the gas phase or a fixed boundary supported by a solid. The configuration of the three phases, including the angle formed by each phase at the triple junctions as well as the heat and the mass transfer profile, are fundamental in understanding the motion of the triple junction. However, there is little consensus in the literature on the phase angles at the triple junction angles. The purpose of this chapter is to investigate this phenomena at a detailed level using energy and mass conservation.

From a theoretical and numerical point of view, phase angles at the triple junction provide the boundary conditions for the interface. To see this, we consider again the strong form of the Stefan condition on the interface,

$$\left[k_l \nabla T_l - k_s \nabla T_s \right] \cdot \hat{n} = -\rho L \vec{v} \cdot \hat{n}, \quad (5.1)$$

where \hat{n} is a unit vector normal to the interface; k_s, k_l are the thermal conductivities and $\nabla T_s, \nabla T_l$ are the temperature gradients for the solid and liquid phase. ρ denotes the density of the solid phase, L is the latent heat of fusion and $\vec{v} \cdot \hat{n}$ denotes the velocity of the interface from solid to liquid.

Consider a function $g \in \mathcal{C}^1$, such that $S = \{(x, t) : g(x, t) = 0\}$ denotes the interface. Then (5.1) can be equivalently written as,

$$\left[k_l \nabla T_l - k_s \nabla T_s \right] \cdot \nabla g = -\rho L \frac{\partial g}{\partial t} \quad \text{on } S. \quad (5.2)$$

Equation (5.2) is a partial differential equation determining the motion of the interface. Without additional information on the phase angles, it is not possible to theoretically or numerically solve the Stefan problem given by equation (5.2). The inclusion of phase angles as boundary condition for the interface is often ignored in numerical simulations of crystal growth systems [43, 123, 139, 140].

To this end researchers have attempted to theoretically and numerically calculate the shape of the solid-liquid interface near the triple junction. Kuiken [107] and Bolling and Tiller [141] analytically calculate the shape of the solid-liquid interface under static conditions. They conclude that the interface approaches the external boundary at an angle of 180° asymptotically, irrespective of material. Helenbrook [115] found that the solid angle at the triple junction is primarily a function of the jump in the radiation heat flux. Edge smoothing is also found to play a role in shaping the solid tip near the triple junction [142, 143]. Mazuruk et al. [144] explains the angles at the triple junction as a bulk phenomenon using bulk free energy potentials. Bardsley et al. [145] provides an explicit formula for the liquid angle and the solid angle using Herring's equilibrium conditions [146]. The formula calculates the liquid angle and the solid angle for silicon as 100° and 111° , respectively.

Tatarchenko [147] provides an extensive experimental literature on the liquid angle for silicon, with values ranging between $90^\circ - 110^\circ$. Cizek [45] photographed silicon sheet growth in the horizontal direction with different seed crystal geometries. He found the solid tip at the triple junction aligned along the lowest energy Wulff shape. Kellerman et al. [99] reported the formation of a dual facet near the triple junction in a horizontal growth configuration. Figure 5.1 shows a photograph of the dual facets observed in experiments by Kellerman et al. [99]. The origin of the dual facet formation at the triple junction is not yet understood [148].

Experimental results are much more consistent in water-ice systems due to the relative ease in performing experiments compared to silicon. Experiments of water droplet solidi-

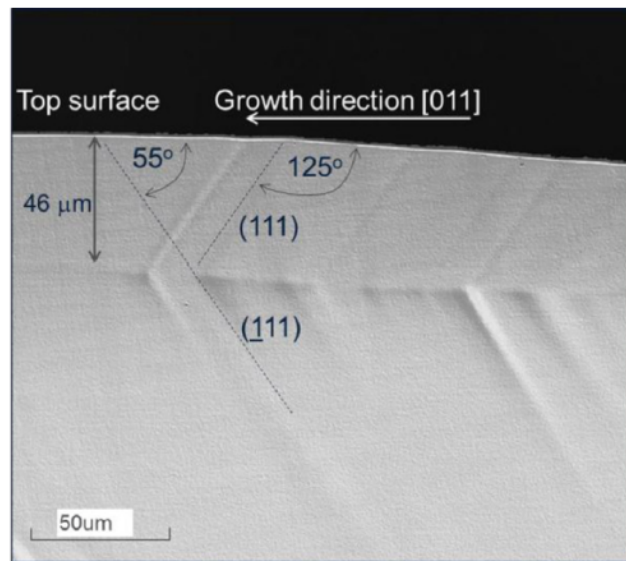


Figure 5.1: A photograph of dual facet formation using antimony demarcation.

fication show the solid and the liquid angles at 90° [149]. The 90° solid and liquid angles were also verified theoretically by Anderson and Davis [112] and Anderson et al. [150]. Schultz et al. [151] performed numerical simulations of a solidifying water droplet and came to the same conclusions.

In this chapter we take a closer look at the physics that drives the motion of the triple junction. The theory will be used to estimate the solid and the liquid angles at the triple point. We will also numerically simulate the horizontal ribbon growth process and verify results with experimental observations. Although the main application of this research is for the horizontal ribbon growth process, the analysis is quite general and can be applied to other areas of solidification, including ice. In fact we recover the same 90° angle reported in the experiments referenced above as the only possible solution under steady state operating conditions.

5.2 Constraints due to Mass and Energy Conservation

Energy Conservation: We begin our analysis by modeling the interface propagation of a solid growing in the horizontal direction near the triple point. A key physics that drives the solidification process is the transport of energy from the solid and liquid phases away from the interface. From the principle of energy conservation, the amount of latent heat released due to solidification is equal to the amount of energy that is transported away from the interface. This imposes a constraint on the dynamics of the interface at the triple point.

We assume the solid-liquid interface to be a continuous curve with zero width. We also assume the solid and liquid phase to behave as a continuum. These assumptions are not valid as we approach the atomic scale. Most bulk crystal growth models rely on these assumptions. Note that the analysis does not assume steady state, is independent of the crystallization kinetics, and does not make any assumption on the shape of the liquid interface. Under these assumptions, the goal is to find constraints that energy and mass conservation impose on interface propagation at the triple point.

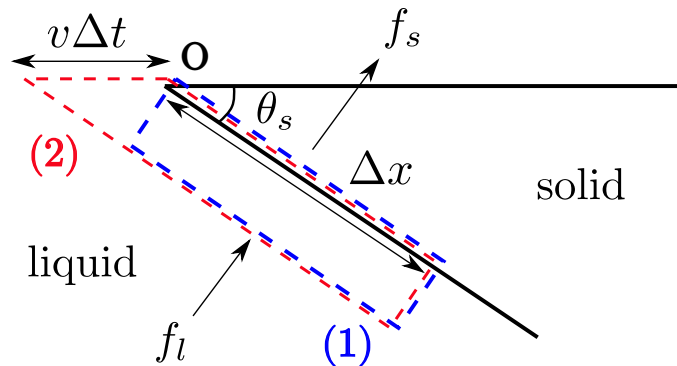


Figure 5.2: A schematic showing the energy flux across the solidification interface at the growth tip.

Figure 5.2 shows the energy transport at the interface near the triple point O at a time instant t . We assume the interface is differentiable near the triple point and makes an

angle θ_s with the horizontal. Let Δx be the length of an interval starting at the triple point \mathbf{O} and stretching along the interface. The average energy flux normal to the interface from the liquid phase and solid phase is denoted by f_l and f_s , respectively. v is the average speed of the interface at the triple point, moving in the horizontal direction. The average is calculated over the interval $[0, \Delta x]$ and $[t, t + \Delta t]$.

Consider two intervals along the interface given by $(0, \Delta x]$ and $[0, \Delta x]$. We term these intervals as region (1) and region (2), respectively. Energy balance for along region (1) over the time interval $(0, \Delta x]$ gives us,

$$(f_s - f_l) \Delta t \Delta x = L \rho_s v \sin \theta_s \Delta t \Delta x, \quad (5.3)$$

where L is the latent heat of fusion per unit mass and ρ_s is the solid phase density. The expression on the right hand side is the energy released due to the propagation of the interface and is represented by the blue box in fig. 5.2.

On the other hand, an energy balance carried over region (2) in the interval $[0, \Delta x]$ gives us,

$$(f_s - f_l) \Delta t \Delta x = L \rho_s v \sin \theta_s \Delta t \Delta x + L \rho_s v^2 \cos \theta_l (\Delta t)^2. \quad (5.4)$$

The expression on the right-hand side is latent heat released due to the growth of the solid phase shown by the red box in fig. 5.2. Subtracting (5.3) from (5.4) and dividing by $\Delta x \Delta t$ we get the identity,

$$L \rho_s v^2 \cos \theta_s \frac{\Delta t}{\Delta x} = 0. \quad (5.5)$$

The left-hand side denotes the additional energy flux per unit time that is liberated due to growth of excess solid at the triple point. Energy cannot be spontaneously created, so the expression on the left-hand side should be zero in the limit $\Delta t, \Delta x \rightarrow 0$. Since the limit does not exist, the identity can only be true if either $v = 0$ or $\theta_s = 90^\circ$. These complementarity constraints impose restrictions on the motion of the triple point and shape of the solid angle. When $\theta_s < 90^\circ$, there is not enough heat removal at the triple point. Therefore, the triple point does not move and waits till the solid angle becomes perpendicular from the

interface motion away from the triple point. When $\theta_s = 90^\circ$, the triple point is free to move and its motion depends on the energy transport in the horizontal direction given by

$$v = \frac{f_s - f_l}{L\rho_s}. \quad (5.6)$$

The difference in the energy balance equations (5.3) and (5.4) can also be resolved if $(f_s - f_l)$ and v are singular. The singularity occurs when $\theta_s > 90^\circ$. In this case, the heat removed from any finite interval of space and time around the triple junction is larger than the amount of latent heat liberated. This causes the triple point moves faster than the rest of the interface till $\theta_s = 90^\circ$. An analytic approach to calculate heat transfer and triple junction speed is carried out in section 5.3 and leads to the same conclusion. Thus we conclude that at the tip the angle θ_s equals 90° under steady state operating conditions.

Mass Conservation: The motion of the interface during the solidification process can be seen as the consumption of liquid material on one end of the interface and the generation of solid material on the other end. Following the mass conservation principle, the two quantities need to be equal over every choice of the interface region. This imposes a condition on the motion of the liquid material close to the interface and the liquid angle.

Similar to the energy conservation analysis, we consider the solid phase and liquid phase to behave like a continuum. The width of the interface will be assumed to be zero. We do not make any assumption on the crystallization kinetics, surface energy of liquid or steady state. In addition, based on the energy conservation analysis, we work with the case when the solid angle $\theta_s = 90^\circ$ and $v \neq 0$. The case with $v = 0$, leads to a static system at the triple point. In this case, the range of liquid angles may be calculated in a fashion similar to the Gibbs pinning condition in appendix A.

Under these assumptions, a schematic for the interphase boundaries at a time instant t near the triple point given in fig. 5.3. The location of the triple point is marked as **O** and is considered to be the origin. The analysis is carried out in a Lagrangian frame of reference, such that the interface appears fixed and the liquid phase moves in and the solid phase moves out of the interface. The average speed of the material near the triple point **O** in

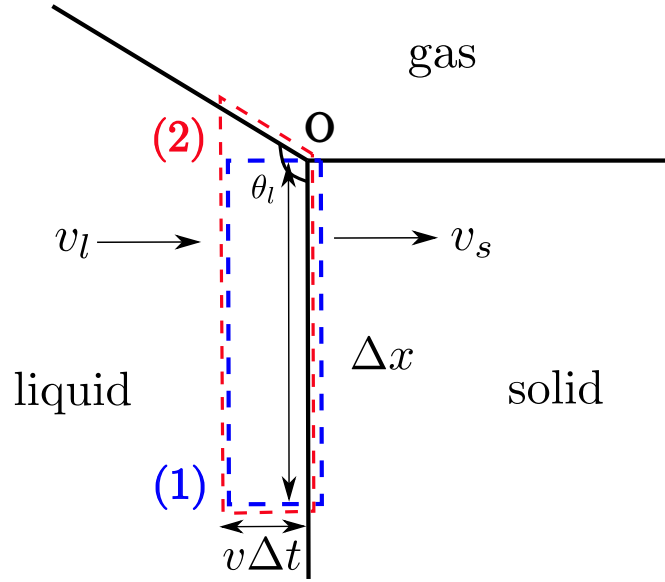


Figure 5.3: A schematic showing the mass flux at the interface from liquid to solid phase. The solid angle θ_s is considered to be 90° .

a direction perpendicular to the interface is given by v_s for the solid phase and v_l for the liquid phase. ρ_l is the average density of the liquid phase close to the triple point. Similar to the energy conservation case, we define region (1) as $(0, \Delta x]$ and region (2) as $[0, \Delta x]$.

A mass balance carried out over region (1) in the time interval $[t, t + \Delta t]$, gives us:

$$\rho_l v_l \Delta t \Delta x = \rho_s v_s \Delta t \Delta x. \quad (5.7)$$

The expression on the right-hand side is the amount of material that changes to solid phase due to the motion of the interface. The motion of the interface is governed by energy balance and determines v_s . The expression on the left-hand side is the amount of liquid consumed during phase change. This is illustrated by the blue box in fig. 5.3.

On the other hand, a mass balance carried over region (2) in the time interval $[t, t + \Delta t]$ gives us,

$$\rho_l v_l \Delta t \Delta x + \rho_l v_l^2 \cot \theta_l (\Delta t)^2 = \rho_s v_s \Delta t \Delta x. \quad (5.8)$$

The expression on the left-hand side is given by the red box shown in fig. 5.3. The second

term in this expression is the excess liquid mass consumed by the interface, which can be geometrically represented by the difference between the red and blue box. Subtracting (5.7) from (5.8) and dividing by $\Delta x \Delta t$ we get the identity,

$$\rho_l v_l^2 \cot \theta_l \frac{\Delta t}{\Delta x} = 0. \quad (5.9)$$

The expression on the left-hand side of (5.9) denotes the additional liquid mass flux per unit time that is consumed at the triple point **O**. Since matter cannot be destroyed this quantity needs to be equal to zero in the limit $\Delta t, \Delta x \rightarrow 0$. The limit for this expression is path dependent. Therefore, (5.5) is only true when $v_l = 0$ or $\theta_l = 90^\circ$. $v_l = 0$ leads to the case when the interface at the triple point is static and governed by Gibbs thermodynamics. When the interface is moving, we get $\theta_l = 90^\circ$ as the only possible solution to the steady state problem. The path dependence of (5.5) and (5.9) in the limit $\Delta t, \Delta x \rightarrow 0$ provides a clue to the multiple-scale nature of the triple point. It also indicates the possibility that growth may not be at steady state in the HRG process [99]. This will be explored further in section 5.3.

5.3 Heat Transfer and Fluid Flow near a Triple Junction

Another approach to understand the interface motion at the triple junction is to solve the steady-state heat equation and the Navier-Stokes equation near the triple point. Analytic methods to solve these equations are well known and can be used to characterize the local behaviour in the solid and liquid phase. The goal of this section is to determine the thermal and the flow field near the triple junction and compare the results to the observations made in the previous section.

We assume that the liquid and the solid phases can be treated as a continuum. The solid-liquid interface is assumed to be a continuous curve of zero width and differentiable at the triple point. In addition, we also assume the liquid-air free surface is differentiable at the triple point. We assume the temperature and the velocity field to be at a steady state.

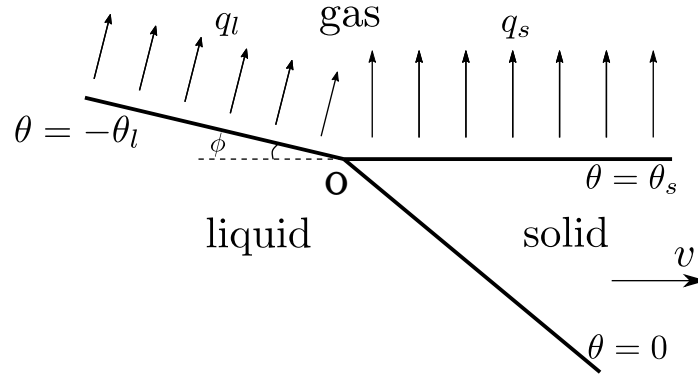


Figure 5.4: A schematic of the three inter-phase boundaries between solid, liquid and gas phases intersecting at the triple point \mathbf{O} .

Figure 5.4 provides a schematic of the inter-phase in a typical crystal growth system, which are approximated as straight lines close to the triple point. The origin is at the triple junction point and is denoted by \mathbf{O} . The co-ordinate axis is now chosen such that the solid-gas interface is in the horizontal direction and the solid-liquid interface is stationary. The solid is withdrawn to the right with velocity v . The heat removal at the solid-gas and liquid-gas interface can be approximated as a constant heat flux with magnitude q_s and q_l , respectively. The growth angle is denoted by ϕ as shown.

Within the solid and the liquid phase, we use the energy balance equation to describe the temperature field,

$$\vec{u}_i \cdot \nabla T_i - k_i \nabla^2 T_i = 0, \quad (5.10)$$

where $i = s, l$ represent the solid and the liquid phases respectively. \vec{u}_i is the velocity field, T_i is the temperature field, and k_i is the thermal conductivity. By choosing the length scales to be of $\mathcal{O}(\epsilon)$, we see that the diffusion term dominates at small length scales, so that we get a singularly perturbed system

$$\epsilon \vec{u}_i \cdot \nabla T_i - k_i \nabla^2 T_i = 0, \quad (5.11)$$

by taking $\epsilon \rightarrow 0$. The resultant equation that needs to be solved is the Laplacian:

$$\nabla^2 T_i = 0. \quad (5.12)$$

We assume local thermodynamic equilibrium at the solid-liquid interface. The boundary conditions close to the triple junction are given by

$$T = 0 \quad \text{on} \quad \theta = 0, \quad (5.13a)$$

$$-k_s \frac{\partial T}{r \partial \theta} + k_l \frac{\partial T}{r \partial \theta} = L \rho_s v \sin \theta_s \quad \text{on} \quad \theta = 0, \quad (5.13b)$$

$$-k_s \frac{\partial T}{r \partial \theta} = q_s \quad \text{on} \quad \theta = \theta_s, \quad (5.13c)$$

$$-k_l \frac{\partial T}{r \partial \theta} = q_l \quad \text{on} \quad \theta = -\theta_l. \quad (5.13d)$$

(5.13a) describes the equilibrium condition along the solid-liquid interface. (5.13b) equates the latent heat released due to solidification to the heat transported away. (5.13c) and (5.13d) represent the heat removal flux from the solid-gas and liquid-gas interface, respectively. To make (5.13c) and (5.13d) homogeneous, we choose a particular solution of the form

$$T_i^p = -\frac{q_i}{k_i \cos \theta_i} r \sin \theta. \quad (5.14)$$

The solution to the homogeneous temperature profile can be calculated using the Fourier basis functions [152]. Locally, the solutions behave as

$$T_s^h = A_s r^{\lambda_s} \sin(\lambda_s \theta) + \mathcal{O}(r^{\lambda_s+1}), \quad (5.15)$$

$$T_l^h = A_l r^{\lambda_l} \sin(\lambda_l \theta) + \mathcal{O}(r^{\lambda_l+1}). \quad (5.16)$$

where λ_s, λ_l are the dominant eigenvalues of the Laplacian (5.12) in solid and liquid phase, respectively. The eigenvalues and the wedge angles satisfy the relationship

$$\lambda_s \theta_s = \lambda_l \theta_l = \frac{\pi}{2}. \quad (5.17)$$

The coefficients $A_{s,l}$ depend on the external boundary conditions of the application domain. Finally, we superimpose the particular and the homogeneous solution to obtain the local temperature profile near the triple junction,

$$T_s = -\frac{q_s}{k_s \cos \theta_s} r \sin \theta + A_s r^{\lambda_s} \sin(\lambda_s \theta) + \mathcal{O}(r^{\lambda_s+1}), \quad (5.18)$$

$$T_l = -\frac{q_l}{k_l \cos \theta_l} r \sin \theta + A_l r^{\lambda_l} \sin(\lambda_l \theta) + \mathcal{O}(r^{\lambda_l+1}). \quad (5.19)$$

When $\theta_{s,l}$ is less than $\pi/2$, $\lambda_{s,l}$ must be greater than 1. In this case, the particular solution is dominant and the heat flux contribution from the homogeneous terms is zero at the triple point. When θ_s or θ_l is greater than $\pi/2$, either λ_s or λ_l is less than 1, respectively, and the homogeneous term dominates close to the origin. As $r \rightarrow 0$, the heat flux at the origin is singular and the interface velocity grows unbounded. These results match our conclusions from the energy conservation in section 5.2. A steady state solution to the growth speed at the triple point cannot be unbounded. Therefore, we restrict the values of θ_s and θ_l to be less than equal to $\pi/2$.

The equation of motion for fluid velocity provide further insights into the choice of solid and liquid wedge angles. To calculate the velocity field \vec{u} , we solve the steady-state Navier-Stokes equation for in-compressible fluids around the growth tip,

$$\vec{u} \cdot \nabla \omega - \mu \nabla^2 \omega = 0 \quad (5.20)$$

$$\omega = -\nabla^2 \psi.$$

The equations are written in terms of the vorticity ω , which is defined as $\omega = \nabla \times \vec{u}$ and the stream function ψ . For the 2D case, the velocity field $\vec{u} = (u_r, u_\theta)$ can be calculated from the stream function as,

$$u_r = \frac{1}{r} \frac{\partial \psi}{\partial \theta}, \quad u_\theta = -\frac{\partial \psi}{\partial r}. \quad (5.21)$$

Similar to the energy balance equation, we are interested in solving the velocity field in a small neighbourhood of the triple junction point. The effect of convection close to the

triple point is negligible at such small length scales. This is apparent when we choose the length scales as $x \rightarrow \frac{x}{\epsilon}$.

$$\epsilon \vec{u} \cdot \omega = \mu \nabla^2 \omega. \quad (5.22)$$

The resulting equation in terms of the stream function is given as:

$$\nabla^4 \psi = 0. \quad (5.23)$$

Equation (5.23) is also known as the Biharmonic equation. A general solution to the Biharmonic equation (5.23) in 2 dimensions is given by the Michell solution,

$$\begin{aligned} \psi(r, \theta) = & A_0 r^2 + B_0 r^2 \ln(r) + C_0 \ln(r) \\ & + (I_0 r^2 + I_1 r^2 \ln(r) + I_2 \ln(r) + I_3) \theta \\ & + (A_1 r + B_1 r^{-1} + B'_1 r \theta + C_1 r^3 + D_1 r \ln(r)) \cos \theta \\ & + (E_1 r + F_1 r^{-1} + F'_1 r \theta + G_1 r^3 + H_1 r \ln(r)) \sin \theta \\ & + \sum_{n=2}^{\infty} (A_n r^n + B_n r^{-n} + C_n r^{n+2} + D_n r^{-n+2}) \cos n\theta \\ & + \sum_{n=2}^{\infty} (E_n r^n + F_n r^{-n} + G_n r^{n+2} + H_n r^{-n+2}) \sin n\theta. \end{aligned} \quad (5.24)$$

We choose three basic boundary conditions for the liquid near the triple point,

$$u_\theta = -\frac{\partial \psi}{\partial r} = \frac{\rho_s}{\rho_l} v \sin \theta_s \quad \text{on} \quad \theta = 0 \quad (5.25a)$$

$$u_r = \frac{1}{r} \frac{\partial \psi}{\partial \theta} = v \cos \theta_s \quad \text{on} \quad \theta = 0 \quad (5.25b)$$

$$u_\theta = -\frac{\partial \psi}{\partial r} = 0 \quad \text{on} \quad \theta = -\theta_l \quad (5.25c)$$

Equation (5.25a) is a mass balance condition in the normal direction to the interface. Equation (5.25b) is a no-slip condition. Equation (5.25c) imposes that there is no liquid flux across the gas-liquid interface. In addition to these boundary conditions, we require that the fluid velocity is not singular and independent of θ at the triple point \mathbf{O} . Therefore, the contributions from terms involving $\ln(r)$ and θ are not considered.

Using (5.25a) and (5.25b) a local solution to the stream function is obtained as,

$$\psi = r \left(-\frac{\rho_s}{\rho_l} v \sin \alpha_1 \cos \theta + v \cos \alpha_1 \sin \theta \right) + \mathcal{O}(r^2). \quad (5.26)$$

This is a simple uniform flow feeding into the solid-liquid interface. The no flux condition at the free surface leads to the condition,

$$\frac{\rho_s}{\rho_l} \sin \theta_s \cos \theta_l + \cos \theta_s \sin \theta_l = 0. \quad (5.27)$$

When the solid and liquid densities are the same, i.e., $\rho_s = \rho_l$, the wedge angles satisfy $\theta_s + \theta_l = \pi$. So the free surface is horizontal and the growth angle $\phi = 0^\circ$. When $\rho_s \neq \rho_l$, (5.27) is true only if at least one wedge angle is greater than $\pi/2$. The heat transfer conditions require that $\theta_s, \theta_l \leq \pi/2$. Therefore, $\theta_s = \theta_l = \pi/2$ is the only configuration where (5.27) is satisfied close to the triple point under steady state conditions.

5.4 Interpretation: Multiple Length Scales Point of View

In section 5.2, we concluded that energy and mass conservation impose a 90° constraint on the solid and liquid angles. However, experimentally the angles do not appear perpendicular and depend on the physical properties of the material under consideration. Crystal growth process have also shown a wide variety of solid angles depending on the orientation of the seed crystal [97, 45]. In the case of silicon and germanium, the observed liquid angles are 101° and 98° , respectively [133].

Theoretical justifications for the observed growth angle and solid angle are based on the principle of free energy minimization. Herring's growth angle formula, used in simulation models of crystal growth, uses a balance of surface tension and torque at the triple junction point [145]. The solid angle is determined by the shape of the minimum energy facet at the solid-liquid interface. The shape of the facet is determined geometrically using the Wulff construction [153]. In both cases, the free energy \mathcal{F} on the solid and the liquid surfaces can

be written as,

$$\mathcal{F} = \int \gamma dS, \quad (5.28)$$

where dS is an element on the interface. For the liquid-gas surface the integrand γ is determined by hydrostatics and is given by equation (3.3) in chapter 3. For a solid surface, the integrand is given by $\gamma(\hat{\theta})$, where γ is the gamma function and $\hat{\theta}$ is the angle made by the normal vector to the solid surface. Figure 5.5 shows an example of a polar gamma plot as a function of θ and also the corresponding Wulff construction of the low energy crystal.

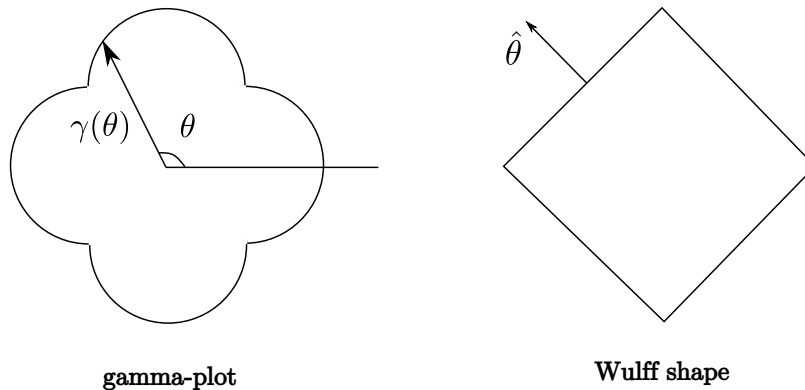


Figure 5.5: Typical polar gamma plot of surface energy of a crystal and the corresponding Wulff shape.

A major assumption in the methods discussed above is the condition of static and thermodynamic equilibrium at the liquid-gas and solid-liquid interface, respectively. Near the triple junction, the interface is continuously evolving, with liquid flowing and large thermal gradients. Clearly, close to the triple junction the assumption of equilibrium does not hold true. However, away from the triple junction the effect of liquid motion and large thermal gradients diminishes with distance and one may find conditions satisfying the assumption of equilibrium. Therefore, a multiple-scale point of view of the triple junction would reconcile the experimental and theoretical observations, while at the same time

satisfying the 90° constraint due to energy and mass balance.

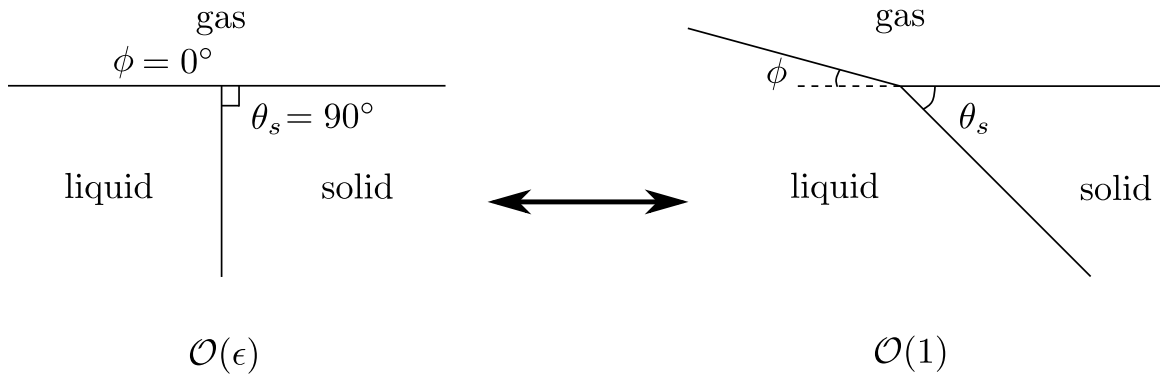


Figure 5.6: A multiple scales point of view of the angles at the triple point.

Figure 5.6 illustrates how the interface would look like near the triple junction at two different length scales. At a length scale of $\mathcal{O}(\epsilon)$, the angles of the gas-liquid-solid interfaces near the triple junction are determined by energy and mass conservation. The solid and the liquid angles are constrained at 90° , because any deviation from this shape leads to a violation of conservation laws. At a more macroscopic length scale, the effect of triple junction motion becomes negligible and physical/material properties are needed to determine the angles. The liquid-gas interface is in a state of static equilibrium, which lead to a non-zero growth angle to minimize surface energy. A condition of thermodynamic equilibrium is also achieved and the solid-liquid interface orients itself in the direction of a low energy facet. This leads to the formation of facet angles typically observed in experiments [97, 45]. The deviation from the minimum energy solution based on (5.28) is only $\mathcal{O}(\epsilon)$.

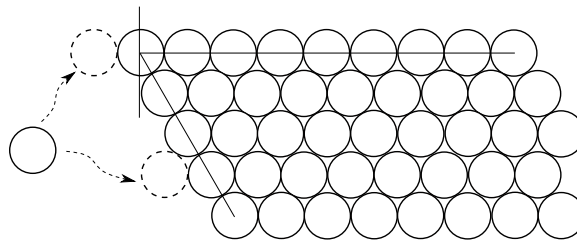


Figure 5.7: An atomic scale interpretation of the 90° solid angle.

How small is the length scale ϵ ? From an energy minimization point of view, ϵ should be as small as possible. As ϵ approaches the atomic scale, an interesting intuition can be developed on the nature of interface motion at the triple junction. Figure 5.7 provides a 2D schematic of atomic lattice in the solid phase near the triple junction. During growth, the atoms attach themselves along the low energy surface. Therefore, motion of the atomic interface takes places in the direction perpendicular to the horizontal at the solid tip or in the direction normal to the low energy facet. Such discrete level dynamics illustrates the origin of the multiple length scale at the triple junction. Continuum scale models are not directly capable of capturing these discrete dynamics. However, they are important when the aim is to build a mono-crystalline sheet. In the next section, we show how a cellular approach can naturally resolve the problem of multiple-length scales in numerical models for crystal growth.

In reality the picture is more complex with curvature and nucleation effects involved. An accurate estimation of the length scale ϵ requires knowledge of solute and temperature distributions; energies of liquid-gas, solid-gas, and solid-liquid surfaces; and the proximity to thermodynamic equilibrium at various regions of the interface. As a first step, the results presented here takes energy and mass balance as the primary basis. Therefore, the 90° condition on the solid and liquid angles should be taken into consideration in any crystal growth model for accurate predictions.

5.5 Cellular Automata Simulations for Facet Growth

A cellular model for simulating the facet formation provides a simple approach to resolve the multiple length scale problem at the triple junction. The proposed approach extends the weak Stefan formulation described in chapter 4. The domain will be discretized into square grids of size Δx . Each grid is categorized as a solid, liquid or interface. The width of the interface is limited to one grid size Δx and corresponds to the mushy phase introduced in Chapter 4. Therefore, at the triple junction, the solid and the liquid angle always appear

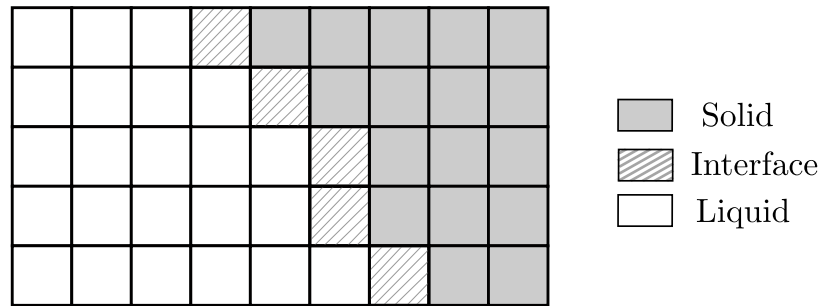


Figure 5.8: Mushy zone ($0 < \chi < 1$) representing the interface.

to be 90° . This is illustrated in fig. 5.8.

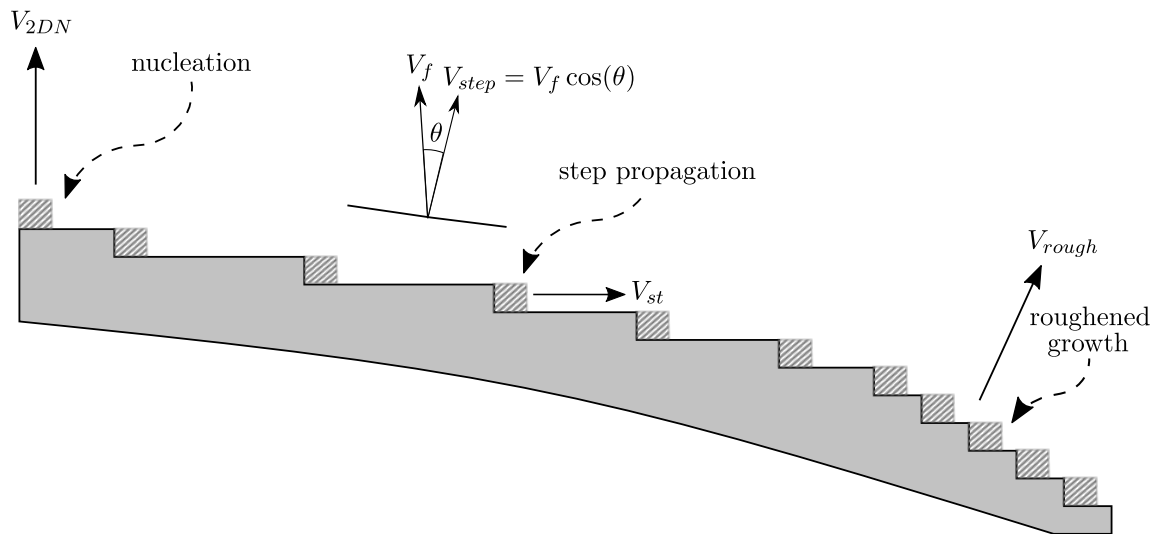


Figure 5.9: Three main mechanisms of crystal growth at the interface

To simulate the formation of flat facets at the solidification interface as observed in experiments, crystallization kinetics need to be included in the simulation model. Flat facets occur due to the inhomogeneity of growth rates on different crystal surfaces. The facet planes tend to be smoother on a molecular scale, with fewer dangling bonds. During solidification, molecules attach more easily to the rough surfaces that have more chemical bonds compared to flat surfaces, hence the facet surfaces advance more slowly.

We use a global assembling procedure as described by Weinstein and Brandon [154] for interface motion and adapt it for our cellular automaton model. The finite growth kinetics can be written down as,

$$\Delta x \frac{\partial \chi}{\partial t} = V, \quad (5.29)$$

$$V = \beta(\theta, \Delta T) \Delta T, \quad (5.30)$$

$$\beta(\theta, \Delta T) = \min(\beta_{rough}, \max(\beta_{2DN}, \beta_{step})). \quad (5.31)$$

$\chi \in [0, 1]$ is the solid fraction field. Equation (5.30) relates the growth rate V to the kinetic coefficient β and the amount to undercooling $\Delta T = T - T_m$. T_m is the melting point, which for silicon is 1685 K.

As illustrated in 5.9, the kinetic coefficient (β) depends on three different mechanisms of solidification: roughened growth, 2D nucleation and step growth. The roughened growth is modeled as $V = \beta_{rough} \Delta T$ where, β_{rough} has a constant value of 0.0126 m/sK. β_{2DN} models the nucleation of atoms on a low index surface. The driving force for 2D nucleation is the degree of supercooling (ΔT) as can be seen from the expression:

$$V = \beta_{2DN} \Delta T = B \exp\left(\frac{-A}{\Delta T}\right) \Delta T \quad (5.32)$$

where A and B are constants with value 140 K and 1.5×10^{10} m/sK respectively. Directional growth of steps across a low index surface is modeled using

$$V = \beta_{step} \Delta T = \beta_{st} |\sin(\theta - \theta_0)| \Delta T,$$

where $\theta_0 = 54^\circ$, is the angle made by the low energy facet to the horizontal and $\beta_{st} = 0.63$ is the step growth parameter. The angle θ made by the interface with the horizontal is calculated using a forward difference method illustrated in fig. 5.10. These equations are combined in (5.31) to give a composite kinetic rate law.

The simulation domain is chosen as a 1×10 mm rectangular box around the triple junction. Heat is removed from the top surface using a Gaussian cooling profile given by,

$$q_t(x) = q_{peak} \exp\left(\frac{-x^2}{2\sigma^2}\right). \quad (5.33)$$

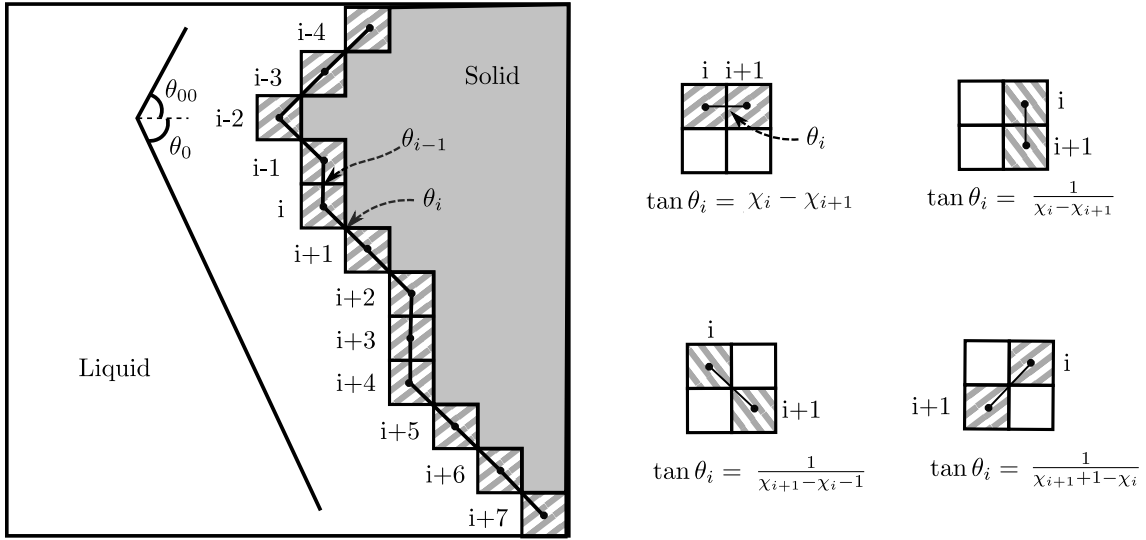


Figure 5.10: Procedure to calculate the facet angle θ along the interface.

σ and q_{peak} values are based on experimental conditions described in Helenbrook et al. [123] and taken as 0.8 and 400 W/cm², respectively. The heat flux at the bottom surface is,

$$q_B = 20 \text{ W/cm}^2. \quad (5.34)$$

The right boundary is considered to be adiabatic and the left boundary heat flux is given by,

$$q_L = 0.134 \times (1690 - T) \text{ W/cm}^2. \quad (5.35)$$

We refer the readers to chapter 4 for more information on the boundary conditions.

We solve the energy balance equation (4.5) inside every grid cell using an Alternating Direction Implicit (ADI) scheme. After every energy balance iteration, the phase field is updated explicitly using the kinetic law (5.29). The interface propagation proceeds anisotropically depending on the interface angle θ . An extensive description of the simulation procedure can be found in chapter 4.

5.5.1 Simulation results

Two sets of simulations are performed with different phase update rules. One simulation includes facet growth dynamics described using (5.29). The other simulation does not include facet growth dynamics and uses (4.4) for updating the phase field. The latter will serve as a base case for comparing the effect of facet formation at the triple junction.

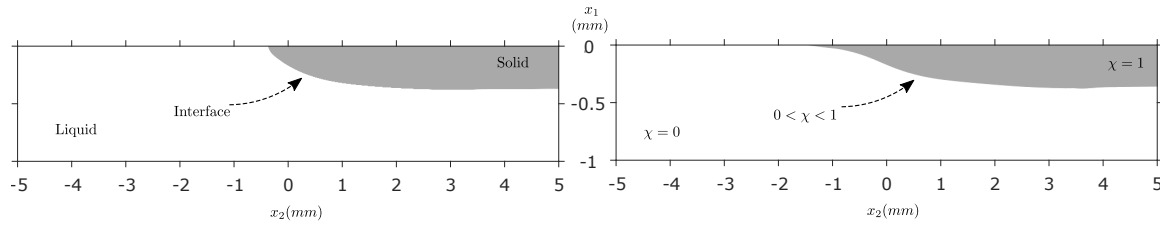


Figure 5.11: Steady state phase field at $v = 4$ mm/sec. The figure on the left includes crystal growth dynamics and the figure on the right does not.

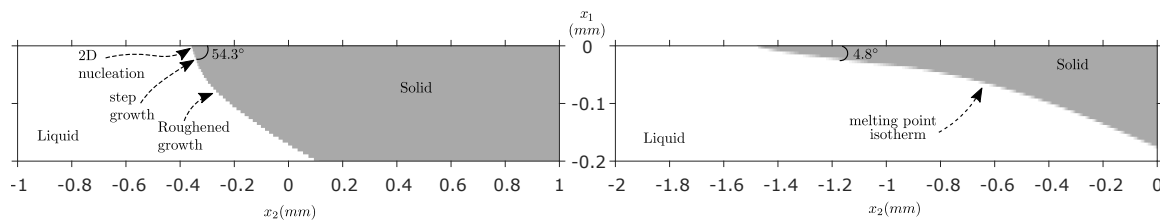


Figure 5.12: A close-up of the solid angle at $v = 4$ mm/sec. The figure on the left shows different stages of crystal growth dynamics at the interface. The figure on the right shows the triangular wedge shape predicted by Zoutendyk's theory.

Figure 5.11 shows the phase field solution obtained from simulations at a pull speed of $v = 4$ mm/sec. The figure on the left includes crystal growth kinetics and has a much larger solid angle compared to the figure on the right which does not include the kinetics. A close-up of the solid as shown in fig. 5.12 demonstrates the different mechanisms of crystal growth near the triple point. When the solid angle approaches close to a nearby facet orientation, the dominant mechanism of crystal growth is 2D nucleation. As we

move away from the triple point, the misalignment angle ($\theta - \theta_0$) increases and the growth mechanism switches to step growth. Further away from the triple point, the misalignment angle becomes so large that the roughened growth dominates. The transition from facet to roughened growth along the interface happens in the interval of $100\mu\text{m}$.

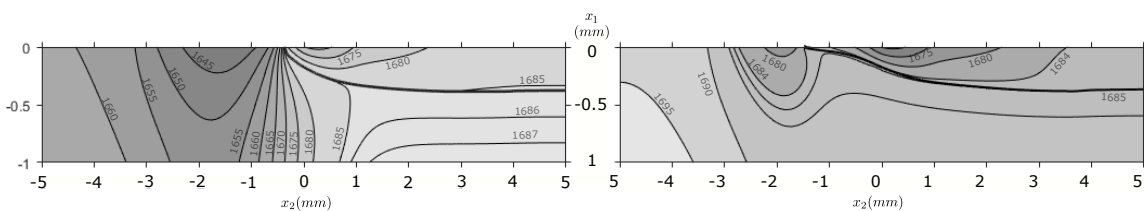


Figure 5.13: Simulation results for the temperature field with crystal growth dynamics (left) and isotropic growth dynamics (right).

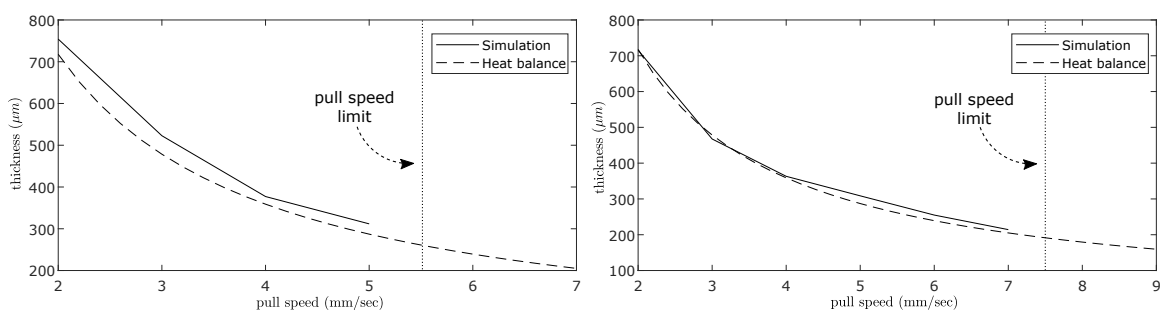


Figure 5.14: Thickness vs. pull speed charts for simulations carried out with (left) and without (right) crystal growth dynamics. The pull speed limitation is more severe when crystal growth is included.

The crystal growth kinetics also have a significant effect on the temperature field near the triple junction. At the triple junction point, the mechanism for growth is 2D nucleation. The kinetic parameter β for 2D nucleation is an increasing function of the undercooling ΔT . Therefore, a large amount of undercooling is needed to maintain the same growth rate as compared to the base case with the isothermal interface condition. This is visible in fig. 5.13, where the undercooling is much larger in the kinetic case. The region of under-

cooling for the base case is much smaller. Also, the solid tip extends deeper into the liquid and make a solid angle of 4.8° . The base case is more closely related to Zoutendyk [119], which predicts the formation of a sharp triangular wedge at the triple point.

One consequence of undercooling is that it is difficult to remove heat from an undercooled solid tip compared to the tip maintained at melting point, since the rate of solidification at the tip determines the limitations on the pull speed of the entire process. Figure 5.14 shows the thickness vs pull speed chart for the two simulation cases. The solid black line denotes the results obtained from simulation. The simulations are carried out at intervals of 1 mm/sec starting from 2 mm/sec. The dashed black line is calculated by equating the total amount of heat removed from the boundaries to the amount of solid removed. We observe that the pull speed limit in the presence of facet growth is severe compared to the base case.

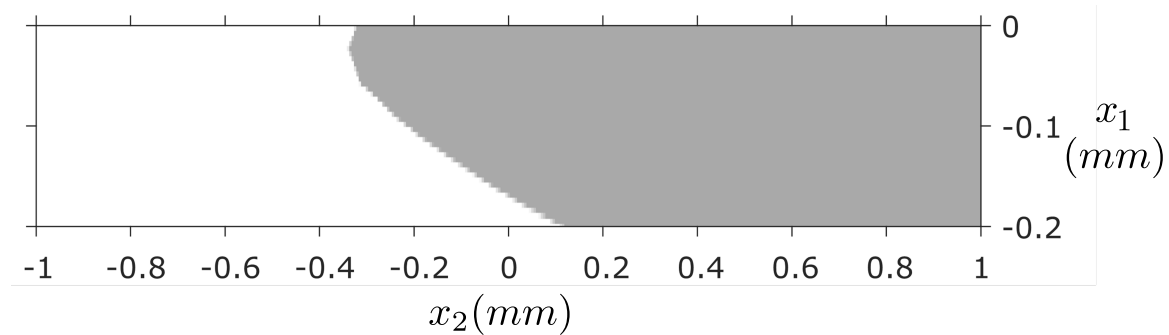


Figure 5.15: Formation of dual facets near the triple point in presence of impurities. A close-up of the simulation result.

The cellular automata algorithm can also simulate the formation of a dual facet at the triple point. Dual facets were found in crystal grown using the horizontal ribbon growth apparatus [99]. Figure 5.15 is the first successful attempt at simulating the formation of a dual facet using first principles. To simulate the dual facet, we manually depresses the melting point of the top $20\mu\text{m}$ by 7°C . The manual decrease in the melting temperature was done to simulate the effect of constitutional undercooling that happens due to impurity

segregation at the interface. This is not too far from experimental conditions which use antimony demarcation to study the facet formation in crystal growth. Kellerman et al. [99] uses an antimony concentration of 6.9×10^{-5} mole fractions which is equivalent to a melting point depression of 7°C .

5.6 Conclusions

The main goal of this chapter is to get a deeper understanding of the physics that drive the motion of the solidification interface near the triple junction. We use the principle of energy and mass conservation as our starting point and obtain constraints on the motion of the interface. We observe that for energy and mass conservation to be satisfied the solid angle and the liquid angle at the interface should be 90° at a small length scale.

From a numerical simulation perspective, we calculate the error in energy and mass balance at the triple point in (5.5) and (5.9). From this we conclude, if the time step Δt is much larger than the grid length Δx , then the error from a non 90° angle at the triple point can be kept bounded.

We found analytic solutions to the heat transfer and fluid flow close to the triple junction. At small length scales and steady state conditions, the temperature and the stream function are shown to satisfy the Laplace equation and the Biharmonic equation, respectively. Simplified boundary conditions are used to obtain explicit solutions for the temperature and velocity field. The solutions indicate that for the heat flux and the viscous stresses are finite only when the solid and the liquid angle at the triple junction are 90° as found from the mass and energy balances.

A multiple scale point of view puts together the 90° constraint found at the triple point with the non 90° facet angles that are observed in experiments. The multiple scale point of view breaks down the important physics and assumption that are valid at different length scales. At small length scales, the motion of the interface is dominant and the assumption of static and thermodynamic equilibrium is not valid. At this length scale, the solid and the

liquid angle are 90° to satisfy energy and mass conservation. At larger length scales, the effect of interface motion decreases and so the assumption of static and thermodynamic equilibrium may become valid. At this length scale, the liquid-gas and solid-liquid interface shapes are determined using the principles of free energy minimization. This leads to the observations of growth angles and facet edges found in experiments.

The multiple scale point of view explains the limitation in solid pull speeds observed in certain crystal growth processes [123, 139]. The heat transfer at the triple junction is fundamentally in the direction of the crystal pull. This is also observed in numerical simulations from chapter 4. In the context of the horizontal ribbon growth process, we see that the advantages in vertical heat transfer perceived with the horizontal mode of pulling is mathematically not true. The multiple scale point of view also explains why current some numerical solvers cannot predict a pull-speed limitation [121, 122, 41, 115].

Finally, we motivate a cellular automata algorithm to resolve the multiple scale problem. The algorithm incorporates crystal growth kinetics to simulate the formation of a low energy facet. Simulations are carried out for the horizontal ribbon growth process. Results show that the formation of a low energy facet decreases the melting point at the triple junction. This causes less heat to be removed from the triple junction compared to the case without any crystal growth dynamics. Therefore, facet formation further lowers the pull speed limit of the horizontal ribbon growth process. The cellular automata algorithm also found the first numerical evidence for the formation of a dual facet at the triple junction (experimentally observed in Kellerman et al. [99]).

Chapter 6

Conclusions and Future Work

6.1 Summary and Contributions

Silicon wafer production is expensive and account for 48% of the total solar cell production cost. In addition, the current technology used to manufacture silicon wafers is a batch process, which is not scalable wastes more than 50% of the end product. As the demand for solar energy increases in the future, a more scalable and efficient solution will reduce the costs of manufacturing solar cells. This will make solar energy more affordable for everyone.

The Horizontal Ribbon Growth (HRG) process provides a potential solution to manufacturing low cost silicon wafer. The advantages of this process are less material waste, increased production speed, and better crystal quality. The main challenge with this process is that the process cannot be operated at the desired operating conditions, which makes the process economically infeasible. Theoretical explanations are given in this thesis for the pull speed limitations observed in HRG process. This has remained an unsolved problem in the crystal growth field for more than 16 years. The results show, using simple tools, that steady state operation of the process as described in current literature is not technologically and economically feasible.

In chapter 3, we provide a parametric formulation and a solution to the generalized static stability problem for the meniscus in a ribbon growth process. Using Weierstrass' variational theory, we found analytic expressions describing the shape of the meniscus and compared it with the family of Euler's elastic curves. The stability of the meniscus is evaluated using Legendre and Jacobi test conditions. A range of stable operating condi-

tions are provided over the parameter space of melt height and pull angle. Interestingly, the horizontal position of the ribbon growth configuration was found to have no solution. This meant that the horizontal position is inherently unstable. The same observation was made in a small scale “kitchen” experiment. We conclude that the ribbon should be pulled above a certain threshold angle to ensure stability.

In chapter 4, we provide a weak Stefan formulation to simulate crystal growth models involving non-smooth edges. Non-smooth edges do not have a unique normal direction. Therefore the strong form of the Stefan formulation used in current computer simulations cannot be directly used for numerical simulations unless extra conditions are imposed. We choose a finite-volume discretization scheme to maintain the conservative form of the weak formulation. This allows us to come up with an easy to implement simulation scheme, which satisfies energy conservation and provides sufficient accuracy for engineering applications. We perform a simulation study of the horizontal ribbon growth process and demonstrate pull speed limitations as observed in experiments. We find that insufficient heat removal from the growth tip is the fundamental reason for pull speed limitation. This insight is used to design an active cooling system using inverse modeling. A linear relationship is discovered between the total heat removed from the furnace and the maximum pull speed. The thickness of the solid was found to be proportional to the spread of the cooling profile.

In Chapter 5, we use the principle of energy and mass conservation as our starting point and obtain constraints on the motion of the interface. We observed that for energy and mass conservation to be satisfied the solid and the liquid interface angles at the interface should be 90° at a small length scale. A multiple scale point of view puts together the 90° constraint found at the triple point with the non 90° facet angles that are observed in experiments. We find that the heat transfer at the triple junction is fundamentally in the direction of the crystal pull and the advantages in vertical heat transfer perceived with the horizontal mode of pulling is mathematically not true. A cellular automata algorithm is

developed to simulate the formation of a low energy facet. The algorithm could also find the first numerical evidence for the formation of a dual facet at the triple junction. The theory was found to correspond closely to published experiments.

6.2 Future Work

The original concept of the Horizontal Ribbon Growth process is found to be infeasible at the rates needed to produce low cost silicon wafer. The next step to increase the production yield using unsteady state periodic control is proposed in Ydstie and Noronha [155]. The main idea is to use oscillation for improving the heat transfer around the triple point to increase the growth speed of the solid. In addition, the oscillation homogenizes the melt, which may help to reduce the effects of impurity segregation close to the solid-liquid interface.

From a computational standpoint, GPU acceleration can be used to carry out high-fidelity simulations in the unsteady state. This can be especially important with cellular automata algorithms, which are computationally irreducible. Advancements in GPU simulations and control of cellular automata process can also contribute to related areas of crystal growth.

Active and concentrated cooling has the potential to improve production speed of all crystal growth processes. Future directions of work should focus on developing active cooling as an independent technology for high speed crystal growth applications.

Bibliography

- [1] R. E. P. N. for the 21st Century, *Renewables 2021 Global Status Report*, 2021.
- [2] J. Goldemberg, "The promise of clean energy," *Energy policy*, vol. 34, no. 15, pp. 2185–2190, 2006.
- [3] A. G. Goncharuk, K. Hromovenko, A. Pahlevanzade, and Y. Hrinchenko, "Energy poverty leap during the pandemic: the case of ukraine," *Polityka Energetyczna-Energy Policy Journal*, pp. 5–18, 2021.
- [4] M. Hasan, M. Mahi, T. Sarker, M. Amin *et al.*, "Spillovers of the covid-19 pandemic: Impact on global economic activity, the stock market, and the energy sector," *Journal of Risk and Financial Management*, vol. 14, no. 5, p. 200, 2021.
- [5] S. Manabe and R. T. Wetherald, "Thermal equilibrium of the atmosphere with a given distribution of relative humidity," 1967.
- [6] S. V. Valentine, "Emerging symbiosis: Renewable energy and energy security," *Renewable and Sustainable Energy Reviews*, vol. 15, no. 9, pp. 4572–4578, 2011.
- [7] E. Fasching and S. Ray, "Solar power will account for nearly half of new u.s. electric generating capacity in 2022," *Today in energy, EIA*, 2022.
- [8] W. J. Cole and J. V. Carag, "2021 standard scenarios report: A us electricity sector outlook," National Renewable Energy Lab.(NREL), Golden, CO (United States), Tech. Rep., 2021.
- [9] S. Maldonado, "The importance of new "sand-to-silicon" processes for the rapid future increase of photovoltaics," *ACS Energy Letters*, vol. 5, no. 11, pp. 3628–3632, 2020.
- [10] S. Ranjan, S. Balaji, R. A. Panella, and B. E. Ydstie, "Silicon solar cell production," *Computers & Chemical Engineering*, vol. 35, no. 8, pp. 1439–1453, 2011.

- [11] M. A. Woodhouse, B. Smith, A. Ramdas, and R. M. Margolis, "Crystalline silicon photovoltaic module manufacturing costs and sustainable pricing: 1h 2018 benchmark and cost reduction road map," National Renewable Energy Lab.(NREL), Golden, CO (United States), Tech. Rep., 2019.
- [12] D. M. Powell, M. T. Winkler, H. Choi, C. B. Simmons, D. B. Needleman, and T. Buonassisi, "Crystalline silicon photovoltaics: a cost analysis framework for determining technology pathways to reach baseload electricity costs," *Energy & Environmental Science*, vol. 5, no. 3, pp. 5874–5883, 2012.
- [13] H. E. Labelle Jr and A. I. Mlavsky, "Method and apparatus for growing inorganic filaments, ribbon from the melt," 1972, uS Patent 3,650,703.
- [14] S. William, "Process for growing single crystals," 1962, uS Patent 3,031,275.
- [15] J. I. Hanoka, "An overview of silicon ribbon growth technology," *Solar energy materials and solar cells*, vol. 65, no. 1-4, pp. 231–237, 2001.
- [16] E. Sachs, D. Harvey, R. Janoch, A. Anselmo, D. Miller, and J. Hanoka, "String ribbon growth via the mesa crucible; multiple ribbons, inherent flatness stability and low materials and power consumption," in *14th Workshop on Crystalline Silicon Solar Cells & Modules: Materials and Processes*, 2004, p. 2.
- [17] R. Wallace, E. Sachs, and J. Hanoka, "Multiple ribbon growth using the string ribbon method," in *3rd World Conference on Photovoltaic Energy Conversion, 2003. Proceedings of*, vol. 2. IEEE, 2003, pp. 1297–1299.
- [18] D. Garcia, M. Ouellette, B. Mackintosh, and J. Kalejs, "Shaped crystal growth of 50 cm diameter silicon thin-walled cylinders by edge-defined film-fed growth (efg)," *Journal of crystal growth*, vol. 225, no. 2-4, pp. 566–571, 2001.
- [19] G. A. Oliveros, R. Liu, S. Sridhar, and B. E. Ydstie, "Silicon wafers for solar cells by horizontal ribbon growth," *Industrial & Engineering Chemistry Research*, vol. 52, no. 9, pp. 3239–3246, 2013.

BIBLIOGRAPHY

- [20] T. Duffar, *Crystal growth processes based on capillarity: Czochralski, floating zone, shaping and crucible techniques*. John Wiley & Sons, 2010.
- [21] T. Surek, *The growth of silicon sheets for photovoltaic applications*. Solar Energy Research Institute, 1980, vol. 614.
- [22] B. Chalmers, "High speed growth of sheet crystals," *Journal of Crystal Growth*, vol. 70, no. 1-2, pp. 3–10, 1984.
- [23] T. Kieliba, "Zone-melting recrystallization for crystalline silicon thin-film solar cells," Ph.D. dissertation, Universität Konstanz, Konstanz, 2006, als Ms. gedr. Berlin : dissertation.de Verlag im Internet GmbH, 2006.
- [24] T. Ciszek, "Techniques for the crystal growth of silicon ingots and ribbons," *Journal of Crystal Growth*, vol. 66, no. 3, pp. 655–672, 1984.
- [25] P. L. Kellerman and F. Sinclair, "Floating sheet production apparatus and method," 2010, uS Patent 7,855,087.
- [26] C. Bleil, "A new method for growing crystal ribbons," *Journal of Crystal Growth*, vol. 5, no. 2, pp. 99–104, 1969.
- [27] C. E. Bleil, "A new approach to continuous crystal sheet growth," *Journal of Crystal Growth*, vol. 104, no. 1, pp. 29–33, 1990.
- [28] B. Kudo, "Improvements in the Horizontal Ribbon Growth technique for single crystal silicon," *Journal of Crystal Growth*, vol. 50, no. 1, pp. 247–259, 1980.
- [29] T. Shudo, B. Kudo, and Y. Tamai, "Lateral pulling growth of crystal ribbons and apparatus therefor," 1981, uS Patent 4,264,407.
- [30] J. A. Zoutendyk, "Analysis of forced convection heat flow effects in horizontal ribbon growth from the melt," *Journal of Crystal Growth*, vol. 50, no. 1, pp. 83–93, 1980.
- [31] ———, "Theoretical analysis of heat flow in horizontal ribbon growth from a melt," *Journal of Applied Physics*, vol. 49, no. 7, pp. 3927–3932, 1978.
- [32] D. Jewett, H. Bates, and J. Locher, "Progress in growth of silicon ribbon by a low angle, high rate process," in *16th Photovoltaic Specialists Conference*, 1982, pp. 86–89.

BIBLIOGRAPHY

- [33] B. T. Helenbrook, P. Kellerman, F. Carlson, N. Desai, and D. Sun, "Experimental and numerical investigation of the horizontal ribbon growth process," *Journal of Crystal Growth*, vol. 453, pp. 163–172, 2016.
- [34] M. Glicksman and P. Voorhees, "Analysis of morphologically stable horizontal ribbon crystal growth," *Journal of Electronic Materials*, vol. 12, no. 1, pp. 161–179, 1983.
- [35] B. T. Helenbrook, "Solidification along a wall or free surface with heat removal," *Journal of Crystal Growth*, vol. 418, pp. 79–85, 2015.
- [36] C. Rhodes, M. Sarraf, and C. Liu, "Investigation of the meniscus stability in horizontal crystal ribbon growth," *Journal of Crystal Growth*, vol. 50, no. 1, pp. 94–101, 1980.
- [37] G. A. Oliveros, S. Sridhar, and B. E. Ydstie, "Existence and static stability of the meniscus in horizontal ribbon growth," *Journal of Crystal Growth*, vol. 411, pp. 96–105, 2015.
- [38] E. P. Noronha, G. A. Oliveros, and B. E. Ydstie, "Weierstrass' variational theory for analysing meniscus stability in ribbon growth processes," *Journal of Crystal Growth*, vol. 553, p. 125945, 2021.
- [39] D. N. Jewett, "Method and apparatus for producing crystalline ribbons," 1981, uS Patent 4,289,571.
- [40] —, "Controlled heat sink for crystal ribbon growth," 1983, uS Patent 4,417,944.
- [41] P. Daggolu, A. Yeckel, and J. J. Derby, "An analysis of segregation during horizontal ribbon growth of silicon," *Journal of Crystal Growth*, vol. 390, pp. 80–87, 2014.
- [42] P. Daggolu, A. Yeckel, C. E. Bleil, and J. J. Derby, "Stability limits for the horizontal ribbon growth of silicon crystals," *Journal of Crystal Growth*, vol. 363, pp. 132–140, 2013.
- [43] —, "Thermal-capillary analysis of the horizontal ribbon growth of silicon crystals," *Journal of Crystal Growth*, vol. 355, no. 1, pp. 129–139, 2012.

BIBLIOGRAPHY

- [44] P. Kellerman, "Floating Silicon Method," Applied Materials-Varian Semiconductor Equipment, Tech. Rep., 2013.
- [45] T. Ciszek, "Orientation and morphology effects in rapid silicon sheet solidification," in *Flat-Plate Solar Array Proj. Res. Forum on the High-Speed Growth and Characterization of Crystals for Solar Cells*, 1984, pp. 223–246.
- [46] A. S. Greenlee, "Towards the development of a horizontal ribbon growth process to produce thin, monocrystalline silicon sheets via the stabilization of the (111) plane in undercooled melts," Ph.D. dissertation, Massachusetts Institute of Technology, 2015.
- [47] P. L. Kellerman, F. M. Carlson, D. Morrell, B. MacKintosh, and N. Desai, "Apparatus and method for controlling thickness of a crystalline sheet grown on a melt," 2018, uS Patent 10,030,317.
- [48] Thomas Young, "An essay on the cohesion of fluids," *Philosophical transactions of the royal society of London*, vol. 3, no. 95, pp. 65–87, 1805.
- [49] Pierre-Simon Laplace, *Traité de mécanique céleste*. de l'Imprimerie de Crapelet, 1799, vol. 1.
- [50] Carl Fredrich Gauss, "Principia generalia theoriae figurae fluidorum in statu aequilibrii," in *Werke*. Springer, 1877, pp. 29–77.
- [51] R. Seidensticker and R. Hopkins, "Silicon ribbon growth by the dendritic web process," *Journal of Crystal Growth*, vol. 50, no. 1, pp. 221–235, 1980.
- [52] S. N. Rossolenko, G. M. Katyba, I. N. Dolganova, I. A. Shikunova, D. O. Stryukov, K. I. Zaitsev, and V. N. Kurlov, "Numerical analysis of liquid menisci in the efg technique," in *Crystal Growth*. IntechOpen, 2019.
- [53] D. Jewett, H. Bates, and J. Locher, "Low angle high rate crystal growth of silicon ribbon," in *Proceedings of the Third Symposium on Materials and New Processing Technologies for Photovoltaics*, vol. 82. Pennington, NJ: Electrochemical Society, 1982, p. 320.

- [54] P. D. Thomas and R. A. Brown, "Rate limits in silicon sheet growth: The connections between vertical and horizontal methods," *Journal of Crystal Growth*, vol. 82, no. 1-2, pp. 1–9, 1987.
- [55] B. Yang, L. Zheng, B. Mackintosh, D. Yates, and J. Kalejs, "Meniscus dynamics and melt solidification in the efg silicon tube growth process," *Journal of Crystal Growth*, vol. 293, no. 2, pp. 509–516, 2006.
- [56] H. Bates and D. Jewett, "Low angle silicon sheet growth: A review of progress, problems and promise," in *Proceedings of the Flat-plate Solar Array Project Research Forum on the High-speed Growth and Characterization of Crystals for Solar Cells*, 1984, pp. 297–307.
- [57] A. Yeckel, R. S. Feigelson, and J. J. Derby, "Analysis of scintillator crystal production via the edge-defined film-fed growth method," in *Hard X-Ray, Gamma-Ray, and Neutron Detector Physics XV*, vol. 8852. International Society for Optics and Photonics, 2013, p. 88520V.
- [58] G. Samanta, A. Yeckel, P. Daggolu, H. Fang, E. D. Bourret-Courchesne, and J. J. Derby, "Analysis of limits for sapphire growth in a micro-pulling-down system," *Journal of Crystal Growth*, vol. 335, no. 1, pp. 148–159, 2011.
- [59] A. Yeckel, "Modeling high speed growth of large rods of cesium iodide crystals by edge-defined film-fed growth (efg)," *Journal of Crystal Growth*, vol. 449, pp. 75–85, 2016.
- [60] K. Mika and W. Uelhoff, "Shape and stability of menisci in czochralski growth and comparison with analytical approximations," *Journal of crystal growth*, vol. 30, no. 1, pp. 9–20, 1975.
- [61] K. Mazuruk and M. Volz, "Static stability of menisci in detached bridgman growth," *Physics of Fluids*, vol. 25, no. 9, p. 094106, 2013.
- [62] —, "Dynamic stability of detached solidification," *Journal of Crystal Growth*, vol. 444, pp. 1–8, 2016.

- [63] T. Surek, "Theory of shape stability in crystal growth from the melt," *Journal of Applied Physics*, vol. 47, no. 10, pp. 4384–4393, 1976.
- [64] V. A. Tatartchenko, "The possibility of shape stability in capillary crystal growth and practical realization of shaped crystals," *Crystal Growth Processes Based on Capillarity: Czochralski, Floating Zone, Shaping and Crucible Techniques*, pp. 51–114, 2010.
- [65] Z. Wang, C.-C. Chang, S.-J. Hong, Y.-J. Sheng, and H.-K. Tsao, "Capillary rise in a microchannel of arbitrary shape and wettability: Hysteresis loop," *Langmuir*, vol. 28, no. 49, pp. 16 917–16 926, 2012.
- [66] E. Pitts, "The stability of pendent liquid drops. part 1. drops formed in a narrow gap," *Journal of Fluid Mechanics*, vol. 59, no. 4, pp. 753–767, 1973.
- [67] T. I. Vogel, "Stability of a liquid drop trapped between two parallel planes," *SIAM Journal on Applied Mathematics*, vol. 47, no. 3, pp. 516–525, 1987.
- [68] G. Soligno, M. Dijkstra, and R. van Roij, "The equilibrium shape of fluid-fluid interfaces: Derivation and a new numerical method for young's and young-laplace equations," *The Journal of chemical physics*, vol. 141, no. 24, p. 244702, 2014.
- [69] A. Lawal and R. A. Brown, "The stability of an inclined pendent drop," *Journal of Colloid and Interface Science*, vol. 89, no. 2, pp. 332–345, 1982.
- [70] —, "The stability of inclined sessile drops," *Journal of Colloid and Interface Science*, vol. 89, no. 2, pp. 346–352, 1982.
- [71] Oskar Bolza, *Lectures on the Calculus of Variations*. Courier Dover Publications, 2018.
- [72] G. A. Oliveros, "Modeling and stability of the horizontal ribbon growth process," Ph.D. dissertation, Carnegie Mellon University, 2014.
- [73] C. Stelian, N. Barthalay, and T. Duffar, "Numerical investigation of factors affecting the shape of the crystal-melt interface in edge-defined film-fed growth of sapphire crystals," *Journal of Crystal Growth*, vol. 470, pp. 159–167, 2017.

- [74] C. Le, Z. Li, W. Mu, Z. Jia, and L. Liu, "3d numerical design of the thermal field before seeding in an edge-defined film-fed growth system for β -ga₂o₃ ribbon crystals," *Journal of Crystal Growth*, vol. 506, pp. 83–90, 2019.
- [75] E. Miroshnichenko, E. Kit, and A. Y. Gelfgat, "Effect of the capillary meniscus height on the instability of large prandtl number czochralski melt flow," *Journal of Crystal Growth*, vol. 453, pp. 20–26, 2016.
- [76] D. Schwabe, R. Uecker, M. Bernhagen, and Z. Galazka, "An analysis of and a model for spiral growth of czochralski-grown oxide crystals with high melting point," *Journal of Crystal Growth*, vol. 335, no. 1, pp. 138–147, 2011.
- [77] M. M. Alimov and K. G. Kornev, "Piercing the water surface with a blade: Singularities of the contact line," *Physics of Fluids*, vol. 28, no. 1, p. 012102, 2016.
- [78] H. Bonart, J. Jung, C. Kahle, and J.-U. Repke, "Influence of liquid density and surface tension on the pinning of sliding droplets on a triangular microstructure," *Chemical Engineering & Technology*, 2019.
- [79] R. L. Levien, "From spiral to spline: Optimal techniques in interactive curve design," Ph.D. dissertation, UC Berkeley, 2009.
- [80] M. Abramowitz and I. A. Stegun, *Handbook of mathematical functions with formulas, graphs, and mathematical tables*. US Government printing office, 1948, vol. 55.
- [81] J. C. Maxwell, "Capillary action," *Encyclopaedia Britannica*, vol. 5, pp. 256–275, 1876.
- [82] J. E. Marsden and T. J. Hughes, *Mathematical foundations of elasticity*. Courier Corporation, 1994.
- [83] J. J. Derby, "The synergy of modeling and novel experiments for melt crystal growth research," in *IOP Conference Series: Materials Science and Engineering*, vol. 355. IOP Publishing, 2018, p. 012001.
- [84] A. Visintin, "Introduction to stefan-type problems," *Handbook of differential equations: evolutionary equations*, vol. 4, pp. 377–484, 2008.

- [85] C. Lan, "Recent progress of crystal growth modeling and growth control," *Chemical engineering science*, vol. 59, no. 7, pp. 1437–1457, 2004.
- [86] S. Ghosh and S. Moorthy, "An arbitrary lagrangian-eulerian finite element model for heat transfer analysis of solidification processes," *Numerical Heat Transfer*, vol. 23, no. 3, pp. 327–350, 1993.
- [87] C. Zhang, B. Gao, A. S. Tremsin, D. Perrodin, T. Shalapska, E. D. Bourret, D. R. Onken, S. C. Vogel, and J. J. Derby, "Analysis of chemical stress and the propensity for cracking during the vertical bridgman growth of babrcl: Eu," *Journal of Crystal Growth*, vol. 546, p. 125794, 2020.
- [88] B. Helenbrook and J. Hrdina, "High-order adaptive arbitrary-lagrangian–eulerian (ale) simulations of solidification," *Computers & Fluids*, vol. 167, pp. 40–50, 2018.
- [89] J. Fainberg, D. Vizman, J. Friedrich, and G. Mueller, "A new hybrid method for the global modeling of convection in cz crystal growth configurations," *Journal of crystal growth*, vol. 303, no. 1, pp. 124–134, 2007.
- [90] T. Jung, J. Seebeck, and J. Friedrich, "Combined global 2d–local 3d modeling of the industrial czochralski silicon crystal growth process," *Journal of crystal growth*, vol. 368, pp. 72–80, 2013.
- [91] O. Weinstein, A. Virozub, W. Miller, and S. Brandon, "Modeling anisotropic shape evolution during czochralski growth of oxide single crystals," *Journal of Crystal Growth*, vol. 509, pp. 71–86, 2019.
- [92] J.-Y. Yan, Y.-W. Wang, Y.-M. Guo, W. Zhang, C. Wang, B.-L. An, and D.-F. Liu, "Formation and preferred growth behavior of grooved seed silicon substrate for kerfless technology," *Chinese Physics B*, vol. 28, no. 6, p. 066802, 2019.
- [93] J. Jhang and C. Lan, "Three-dimensional phase field modelling of twin nucleation during directional solidification of multi-crystalline silicon," *Journal of Crystal Growth*, vol. 520, pp. 33–41, 2019.

- [94] A. M. Jokisaari, P. W. Voorhees, J. E. Guyer, J. A. Warren, and O. G. Heinonen, "Phase field benchmark problems for dendritic growth and linear elasticity," *Computational Materials Science*, vol. 149, pp. 336–347, 2018.
- [95] A. Krauze, J. Virbulis, S. Zitzelsberger, and G. Ratnieks, "3d modeling of growth ridge and edge facet formation in; 100; floating zone silicon crystal growth process," *Journal of Crystal Growth*, vol. 520, pp. 68–71, 2019.
- [96] D. G. Schwabe, "Spiral crystal growth in the czochralski process—revisited, with new interpretations," *Crystal Research and Technology*, vol. 55, no. 2, p. 1900073, 2020.
- [97] L. Stockmeier, C. Kranert, G. Raming, A. Miller, C. Reimann, P. Rudolph, and J. Friedrich, "Edge facet dynamics during the growth of heavily doped n-type silicon by the czochralski-method," *Journal of Crystal Growth*, vol. 491, pp. 57–65, 2018.
- [98] L. Stockmeier, C. Kranert, P. Fischer, B. Epelbaum, C. Reimann, J. Friedrich, G. Raming, and A. Miller, "Analysis of the geometry of the growth ridges and correlation to the thermal gradient during growth of silicon crystals by the czochralski-method," *Journal of Crystal Growth*, vol. 515, pp. 26–31, 2019.
- [99] P. Kellerman, B. Kernan, B. T. Helenbrook, D. Sun, F. Sinclair, and F. Carlson, "Floating silicon method single crystal ribbon—observations and proposed limit cycle theory," *Journal of Crystal Growth*, vol. 451, pp. 174–180, 2016.
- [100] K. Fujiwara, "Crystal growth behaviors of silicon during melt growth processes," *International Journal of Photoenergy*, vol. 2012, 2012.
- [101] V. Lau Jr, K. Maeda, K. Fujiwara, and C.-w. Lan, "In situ observation of the solidification interface and grain boundary development of two silicon seeds with simultaneous measurement of temperature profile and undercooling," *Journal of Crystal Growth*, vol. 532, p. 125428, 2020.
- [102] K.-K. Hu, K. Maeda, K. Shiga, H. Morito, and K. Fujiwara, "In situ observation of multiple parallel (1 1 1) twin boundary formation from step-like grain boundary during si solidification," *Applied Physics Express*, vol. 13, no. 10, p. 105501, 2020.

- [103] G. Segal, K. Vuik, and F. Vermolen, "A conserving discretization for the free boundary in a two-dimensional stefan problem," *Journal of Computational Physics*, vol. 141, no. 1, pp. 1–21, 1998.
- [104] C. Vuik, A. Segal, and F. J. Vermolen, "A conserving discretization for a stefan problem with an interface reaction at the free boundary," *Computing and visualization in science*, vol. 3, no. 1-2, pp. 109–114, 2000.
- [105] J. King, D. Riley, and A. Wallman, "Two-dimensional solidification in a corner," *Proceedings of the Royal Society of London. Series A: Mathematical, Physical and Engineering Sciences*, vol. 455, no. 1989, pp. 3449–3470, 1999.
- [106] A. Yeckel, "Novel means to modify growth interface shape in vertical bridgman crystal growth," <http://www.cats2d.com/SIVB/insulatedVB.html>, 2017, accessed: 2021-01-31.
- [107] H. Kuiken, "A note on the wall singularity of a solid–liquid interface caused by a difference between the thermal conductivities of the solid and the liquid phases," *SIAM Journal on Applied Mathematics*, vol. 48, no. 4, pp. 921–924, 1988.
- [108] A. Ostrogorsky, V. Riabov, and N. Dropka, "Interface control by rotating submerged heater/baffle in vertical bridgman configuration," *Journal of Crystal Growth*, vol. 498, pp. 269–276, 2018.
- [109] M. Volz, K. Mazuruk, M. Aggarwal, and A. Cröll, "Interface shape control using localized heating during bridgman growth," *Journal of crystal growth*, vol. 311, no. 8, pp. 2321–2326, 2009.
- [110] P. Sackinger, R. Brown, and J. Derby, "A finite element method for analysis of fluid flow, heat transfer and free interfaces in czochralski crystal growth," *International journal for numerical methods in fluids*, vol. 9, no. 4, pp. 453–492, 1989.
- [111] P. Ramachandran and P. Gunjal, "Comparison of boundary collocation methods for singular and non-singular axisymmetric heat transfer problems," *Engineering analysis with boundary elements*, vol. 33, no. 5, pp. 704–716, 2009.

- [112] D. Anderson and S. Davis, "Fluid flow, heat transfer, and solidification near tri-junctions," *Journal of crystal growth*, vol. 142, no. 1-2, pp. 245–252, 1994.
- [113] N. M. Wigley, "On a method to subtract off a singularity at a corner for the dirichlet or neumann problem," *Mathematics of Computation*, vol. 23, no. 106, pp. 395–401, 1969.
- [114] C. Cheng, Z. Han, S. Yao, Z. Niu, and N. Recho, "Analysis of heat flux singularity at 2d notch tip by singularity analysis method combined with boundary element technique," *Engineering Analysis with Boundary Elements*, vol. 46, pp. 1–9, 2014.
- [115] B. T. Helenbrook, "Solidification along a wall or free surface with heat removal," *Journal of Crystal Growth*, vol. 418, pp. 79–85, 2015.
- [116] A. Pirnia and B. T. Helenbrook, "Analysis of faceted solidification in the horizontal ribbon growth crystallization process," *Journal of Crystal Growth*, p. 125958, 2020.
- [117] G. A. Oliveros, S. Sridhar, and B. E. Ydstie, "Existence and static stability of the meniscus in horizontal ribbon growth," *Journal of Crystal Growth*, vol. 411, pp. 96–105, 2015.
- [118] B. Kudo, "Improvements in the horizontal ribbon growth technique for single crystal silicon," *Journal of Crystal Growth*, vol. 50, no. 1, pp. 247–259, 1980.
- [119] J. A. Zoutendyk, "Theoretical analysis of heat flow in horizontal ribbon growth from a melt," *Journal of Applied Physics*, vol. 49, no. 7, pp. 3927–3932, 1978.
- [120] —, "Analysis of forced convection heat flow effects in horizontal ribbon growth from the melt," *Journal of Crystal Growth*, vol. 50, no. 1, pp. 83–93, 1980.
- [121] P. Daggolu, A. Yeckel, C. E. Bleil, and J. J. Derby, "Thermal-capillary analysis of the horizontal ribbon growth of silicon crystals," *Journal of crystal growth*, vol. 355, no. 1, pp. 129–139, 2012.
- [122] —, "Stability limits for the horizontal ribbon growth of silicon crystals," *Journal of crystal growth*, vol. 363, pp. 132–140, 2013.

BIBLIOGRAPHY

- [123] B. T. Helenbrook, P. Kellerman, F. Carlson, N. Desai, and D. Sun, "Experimental and numerical investigation of the horizontal ribbon growth process," *Journal of Crystal Growth*, vol. 453, pp. 163–172, 2016.
- [124] T. Sun, J. Ding, C. Jiang, J. Xu, and N. Yuan, "Simulating the horizontal growth process of silicon ribbon," *AIP Advances*, vol. 8, no. 8, p. 085307, 2018.
- [125] T. Sun, Z. Zhang, G. Cheng, K. Zhu, J. Xu, N. Yuan, and J. Ding, "Numerical investigation of thermocapillary and buoyancy convection in horizontal ribbon growth with lid-driven boundary," *AIP Advances*, vol. 10, no. 11, p. 115310, 2020.
- [126] J. Ke, A. S. Khair, and B. E. Ydstie, "The effects of impurity on the stability of horizontal ribbon growth," *Journal of Crystal Growth*, vol. 480, pp. 34–42, 2017.
- [127] E. P. Noronha, G. A. Oliveros, and B. E. Ydstie, "Weierstrass' variational theory for analysing meniscus stability in ribbon growth processes," *Journal of Crystal Growth*, vol. 553, p. 125945, 2020.
- [128] P. Lax and B. Wendroff, "Systems of conservation laws," *Communications on Pure and Applied Mathematics*, vol. 13, no. 2, pp. 217–237, 1960.
- [129] J. M. McDonough, "Lectures on computational numerical analysis of partial differential equations," 2008.
- [130] Y. Cheng, "The growth of dislocation-free bicrystal silicon ribbon," *Journal of Physics D: Applied Physics*, vol. 26, no. 7, p. 1109, 1993.
- [131] J. R. Howel, R. Siegel, and M. Mengu, "Thermal radiation heat transfer 5th edition, 460-466," 2011.
- [132] A. Novick-Cohen, "Triple-junction motion for an allen–cahn/cahn–hilliard system," *Physica D: Nonlinear Phenomena*, vol. 137, no. 1-2, pp. 1–24, 2000.
- [133] T. Surek and B. Chalmers, "The direction of growth of the surface of a crystal in contact with its melt," *Journal of Crystal Growth*, vol. 29, no. 1, pp. 1–11, 1975.

- [134] A. Virozub, I. G. Rasin, and S. Brandon, "Revisiting the constant growth angle: Estimation and verification via rigorous thermal modeling," *Journal of Crystal Growth*, vol. 310, no. 24, pp. 5416–5422, 2008.
- [135] P. H. Steen and C. Karcher, "Fluid mechanics of spin casting of metals," *Annual review of fluid mechanics*, vol. 29, no. 1, pp. 373–397, 1997.
- [136] C. Herring, "Surface tension as a motivation for sintering," in *Fundamental Contributions to the Continuum Theory of Evolving Phase Interfaces in Solids*. Springer, 1999, pp. 33–69.
- [137] R. Ge, P. Clapp, and J. Rifkin, "Molecular dynamics of a molten cu droplet spreading on a cold cu substrate," *Surface science*, vol. 426, no. 1, pp. L413–L419, 1999.
- [138] S. Tarafdar, Y. Y. Tarasevich, M. Dutta Choudhury, T. Dutta, and D. Zang, "Droplet drying patterns on solid substrates: From hydrophilic to superhydrophobic contact to levitating drops," *Advances in Condensed Matter Physics*, vol. 2018, 2018.
- [139] J. Friedrich, T. Jung, M. Trempa, C. Reimann, A. Denisov, and A. Muehe, "Considerations on the limitations of the growth rate during pulling of silicon crystals by the czochralski technique for pv applications," *Journal of Crystal Growth*, vol. 524, p. 125168, 2019.
- [140] J. Cunhua, S. Tao, Y. Ningyi, and D. Jianning, "Dynamic stability and failure mechanism of meniscus during horizontal ribbon growth of silicon wafer," *ACTA ENERGIAE SOLARIS SINICA*, vol. 40, no. 7, pp. 1944–1949, 2019.
- [141] G. Bolling and W. Tiller, "Growth from the melt. i. influence of surface intersections in pure metals," *Journal of Applied Physics*, vol. 31, no. 8, pp. 1345–1350, 1960.
- [142] C. Herring, "Some theorems on the free energies of crystal surfaces," *Physical review*, vol. 82, no. 1, p. 87, 1951.
- [143] T. L. Einstein, "Equilibrium shape of crystals," in *Handbook of Crystal Growth*. Elsevier, 2015, pp. 215–264.
- [144] K. Mazuruk, A. Croll, and M. P. Volz, "Growth angle: A microscopic view," 2017.

BIBLIOGRAPHY

- [145] W. Bardsley, F. Frank, G. Green, and D. Hurle, "The meniscus in czochralski growth," *Journal of Crystal Growth*, vol. 23, no. 4, pp. 341–344, 1974.
- [146] C. Herring, "The physics of powder metallurgy, chapter 8," 1951.
- [147] V. A. Tatarchenko, *Shaped crystal growth*. Springer Science & Business Media, 1993, vol. 20.
- [148] A. Pirnia and B. T. Helenbrook, "Physics of double faceted crystal growth in solidification processes," *Journal of Crystal Growth*, p. 126517, 2022.
- [149] A. G. Marin, O. R. Enriquez, P. Brunet, P. Colinet, and J. H. Snoeijer, "Universality of tip singularity formation in freezing water drops," *Physical review letters*, vol. 113, no. 5, p. 054301, 2014.
- [150] D. Anderson, M. G. Worster, and S. Davis, "The case for a dynamic contact angle in containerless solidification," *Journal of crystal growth*, vol. 163, no. 3, pp. 329–338, 1996.
- [151] W. Schultz, M. Worster, and D. Anderson, "Solidifying sessile water droplets," in *Interactive dynamics of convection and solidification*. Springer, 2001, pp. 209–226.
- [152] J. Fourier *et al.*, *The analytical theory of heat*. The University Press, 1878.
- [153] G. Wulff, "Xv. zur frage der geschwindigkeit des wachstums und der auflösung der krystallflächen," *Zeitschrift für Kristallographie-Crystalline Materials*, vol. 34, no. 1-6, pp. 449–530, 1901.
- [154] O. Weinstein and S. Brandon, "Dynamics of partially faceted melt/crystal interfaces I: Computational approach and single step-source calculations," *Journal of Crystal Growth*, vol. 268, no. 1-2, pp. 299–319, 2004.
- [155] B. E. Ydstie and E. P. Noronha, "Method for producing a sheet from a melt by imposing a periodic change in the rate of pull," 2021, uS Patent App. 17/266,417.

Appendix A

Young's contact angle and Gibbs pinning condition

The parametric Young-Laplace equation (3.13) derived in section 3.4 relies on contact angle conditions at the boundary in order to find stationary curves that describe the meniscus shape. By perturbing the end points of the meniscus, we show that the contact angle and the Gibbs pinning conditions follow as a consequence of the free energy minimization of the system.

Consider the free energy formulation for the meniscus $x(s)$, $y(s)$ as defined in section 3.3 and add the surface energy of the solid boundaries in contact with the air and the liquid. For simplicity, we briefly consider the case where only the end point at the origin is varied while the end point at s_t is considered fixed. In this case,

$$\Delta U = \int_0^{s_t} -\Delta P xy' ds + \gamma \sqrt{x'^2 + y'^2} ds + A_1 \gamma_1 + A_2 \gamma_2,$$

where A_1 and A_2 are the areas of the solid crucible in contact with the melt and the air respectively. γ_1 , γ_2 are the interfacial energies of the melt and the air boundaries with the crucible (see figure A.1).

As before, we introduce small perturbations of $\epsilon \xi(s)$ and $\epsilon \eta(s)$ into $x(s)$ and $y(s)$. These perturbations are fixed at s_t such that $\xi(s_t) = \eta(s_t) = 0$. Using the definition (3.3), the first variation in energy is given by

$$\delta U = \int_0^{s_t} (\xi g_x + \xi' g_{x'} + \eta g_y + \eta' g_{y'}) ds + \delta r (\gamma_2 - \gamma_1),$$

where $|\delta r| = \sqrt{\xi(0)^2 + \eta(0)^2}$. Integrating by parts, we arrive at the following form of the

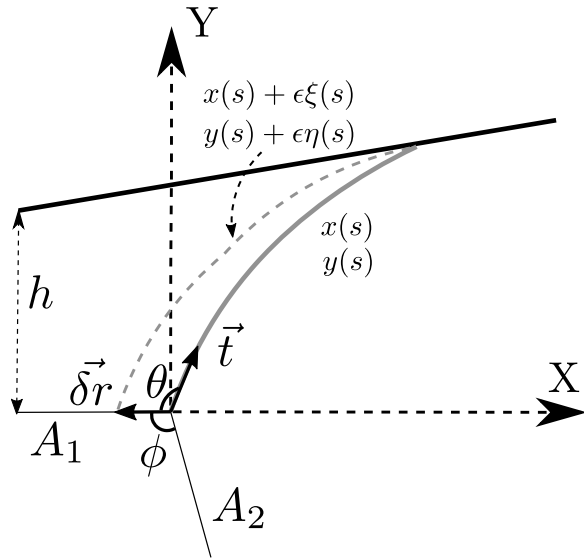


Figure A.1: For the case of variable endpoints, the perturbation at the origin is considered to be $\vec{\delta r}$. The aim is to find conditions on the meniscus shape such that $\vec{\delta r} = 0$ is a minimum.

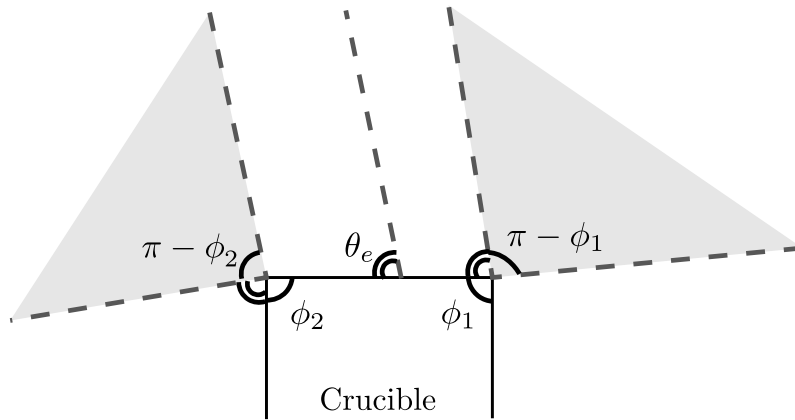


Figure A.2: The shaded region displays the range of pinning angles for the inner and the outer edges. The figure shows how the starting position of the meniscus would change as the pinning angle is varied.

first variation,

$$\delta U = \int_0^{st} \left[\xi \left(g_x - \frac{d}{ds} g_{x'} \right) + \eta \left(g_y - \frac{d}{ds} g_{y'} \right) \right] ds - \xi g_{x'} \Big|_0 - \eta g_{y'} \Big|_0 + \delta r (\gamma_2 - \gamma_1).$$

Setting the integrand to zero gives us the Euler-Lagrange equation for optimality. Substituting the expressions for $g_{x'}$ and $g_{y'}$ give us

$$\delta U = -\gamma \frac{\xi x' + \eta y'}{\sqrt{x'^2 + y'^2}} \Big|_0 + \delta r (\gamma_2 - \gamma_1).$$

The first term can be interpreted as a dot product between $\vec{\delta r} = [\xi(0), \eta(0)]$ and $\vec{t} = [x'(0), y'(0)]$, which can be written in terms of the cosine of the angle between them.

$$\delta U = \begin{cases} \gamma \delta r \left(-\cos(\theta) + \frac{\gamma_2 - \gamma_1}{\gamma} \right) & \delta r > 0 \\ \gamma \delta r \left(\cos(2\pi - \phi - \theta) + \frac{\gamma_2 - \gamma_1}{\gamma} \right) & \delta r < 0 \end{cases}$$

We see that the first variation is minimized and becomes zero at $\delta r = 0$ when

$$\begin{aligned} \theta_e &\leq \theta \leq \pi - \phi + \theta_e, \\ \theta_e &= \arccos \left(\frac{\gamma_2 - \gamma_1}{\gamma} \right). \end{aligned}$$

This range of θ values is known as the Gibbs pinning condition and is illustrated by the shaded region in figure A.2. The Young-Dupre contact angle condition follows as a corollary by setting $\phi = \pi$.

When $\theta \leq \theta_e$ the meniscus recedes horizontally along the crucible boundary until it gets pinned to the inner corner of the crucible. An extended range of pinning angles, as illustrated by the shaded region in figure A.2 follows. The overall range for the pinning conditions can be derived using a similar analysis.